Evaluation of Characterization Methods for Cu-Sn Micro-Connects

Nikolai Mäntyoja

School of Electrical Engineering

Thesis submitted for examination for the degree of Master of Science in Technology.

Espoo 25.01.2016

Thesis supervisor:

Prof. Mervi Paulasto-Kröckel

Thesis advisor:

M.Sc. Mikael Broas

Aalto University
School of Electrical
Engineering

AALTO UNIVERSITY
SCHOOL OF ELECTRICAL ENGINEERING

ABSTRACT OF THE
MASTER'S THESIS

Author: Nikolai Mäntyoja

Title: Evaluation of Characterization Methods for Cu-Sn Micro-Connects

Date: 25.01.2016 Language: English Number of pages: 9+105

Department of Electrical Engineering and Automation

Professorship: Electronics Integration and Reliability

Supervisor: Prof. Mervi Paulasto-Kröckel

Advisor: M.Sc. Mikael Broas

The microelectronics industry constantly aspires to shrink the device features. At the package level, this implies a decrease in the interconnect size leading to small volume interconnections that are commonly called micro-connects. Smaller material volumes may give rise to new reliability challenges, such as open circuits, due to Kirkendall voiding. The root cause(s) for Kirkendall voiding is not yet clear and the methods for characterization are still varied.

This thesis reviews techniques to characterize the microstructure and impurities in Cu-Sn micro-connects. The evaluated techniques are Auger Electron Spectroscopy (AES), Electron Energy Loss Spectroscopy (EELS), Energy-Dispersive X-Ray Spectroscopy (EDX), X-Ray Spectroscopy (XPS), Secondary Ion Mass Spectrometry (SIMS), Rutherford Backscattering Spectrometry (RBS), Elastic Recoil Detection Analysis (EELS), Transmission Electron Microscopy (TEM), Focused Ion Beam (FIB), and Scanning Acoustic Microscopy (SAM). From the reviewed techniques, EDX, FIB, SAM, and TEM are used in the experimental section. For the first time, impurities are measured directly inside Kirkendall voids. It was discovered that the Kirkendall voids in annealed Cu-Sn samples contained a significant amount of chlorine and oxygen.

The ASTM grain size counting method was applied to FIB-polished samples. It was observed that the grain size did not increase by annealing at 150 °C. Furthermore, for the first time, GHz-SAM was used to characterize Kirkendall voids. The technique is promising but it is still affected by the low lateral resolution.

Keywords: Micro-Connect, Voiding, Impurities, Kirkendall Voids, TEM, FIB

AALTO-YLIOPISTO
SÄHKÖTEKNIIKAN KORKEAKOULU

DIPLOMITYÖN
TIIVISTELMÄ

Tekijä: Nikolai Mäntyoja

Työn nimi: Kupari-tina mikroliitosten karakterisointimenetelmät

Päivämäärä: 25.01.2016 Kieli: Englanti Sivumäärä: 9+105

Sähkötekniikan ja automaation laitos

Professuuri: Elektroniikan integrointi ja luotettavuus

Työn valvoja: Prof. Mervi Paulasto-Kröckel

Työn ohjaaja: DI Mikael Broas

Mikroelektroniikkateollisuus pyrkii jatkuvasti pienentämään laitekokoa. Paketointitasolla tämä tarkoittaa sitä, että sirujen välisten liitosten kokoluokka on siirtymässä kohti mikroliitoksia, jotka saattavat aiheuttaa uusia luotettavuusongelmia. Kirkendall-aukot ovat yksi syy kyseisiin luotettavuusongelmiin ja aukkojen alkuperä on vielä tuntematon. Sen lisäksi, mikroliitosten ja Kirkendall-aukkojen karakterisointiin käytetään toisistaan poikkeavia menetelmiä eikä sopivista metodeista ole vielä yhteisymmärrystä.
Tämä diplomityö tarkastelee kupari-tina mikroliitoksien mikrorakenteen ja epäpuhtauksien analysointiin käytettyjä menetelmiä. Tarkasteltavat menetelmät ovat Auger-elektronispektroskopia (AES), epäelastinen elektronisironta (EELS), energiadispersiivinen röntgenspektroskopia (EDX), röntgenfotoelektronispektroskopia (XPS), sekundääri-ionimassaspektroskopia (SIMS), Rutherford-takaisinsirontaspektroskopia (RBS), rekyylispektrometria (ERDA), läpäisyelektronimikroskopia (TEM), keskitetty ionisuihku (FIB) ja akustinen mikroskopia (SAM). Esitellyistä menetelmistä kokeellisessa osiossa käytettiin EDX:ää, FIB:ä, SAM:a ja (S)TEM:ä. Tässä diplomityössä on mitattu ensimmäistä kertaa epäpuhtauksia Kirkendall-aukkojen sisältä. Mittauksista saatiin selville, että hehkutettujen kupari-tina -näytteiden Kirkendall-aukot sisälsivät huomattavan määrän happea ja klooria.
Raekokoa tarkasteltiin kiillottamalla näytteet FIB:llä ja soveltamalla ASTM:n raekoko -standardia. Työssä huomattiin, että raekoko ei kasvanut, jos näytteitä hehkutettiin 150 °C lämpötilassa. Tämä on myös ensimmäinen kerta, kun GHz-SAM:a on käytetty Kirkendall-aukkojen tutkimiseen. Tulokset olivat lupaavia, mutta menetelmän alhainen sivuttaissuuntainen resoluutio on vielä rajoittava tekijä.

Avainsanat: Mikroliitokset, Huokoisuus, Epäpuhtaudet, Kirkendall-aukot, TEM, FIB

Preface

This thesis is related to research by my colleague Glenn Ross, whom I would like to thank for the idea of this thesis. I also want to thank the other members of our research group for teaching me during the two and a half years that I was able to participate in fascinating research in the field of electronics reliability and integration.

I particularly would like to thank my supervisor Professor Mervi-Paulasto Kröckel as well as my advisor M.Sc. Mikael Broas. My supervisor has provided me excellent guidance and possibility for flexible working conditions. My advisor provided me help by scheduling, giving excellent commentary, and assisting in grammar. I also want to thank my family and Emma for understanding the stress during the demanding task that I was occupied with. Furthermore, I would like to thank Fraunhofer IMWS for providing the (S)TEM, STEM-EDX, and GHz-SAM results for this thesis.

Otaniemi, 25.01.2016

Nikolai Mäntyoja

Contents

Abstract ii

Abstract (in Finnish) iii

Preface iv

Contents v

Symbols and abbreviations vii

1 Introduction 1

2 3D Integration 2

3 Research Question 7

4 Impurity Analysis 8
4.1 Auger Electron Spectroscopy . . . 9
4.2 Electron Energy Loss Spectroscopy . . . 13
4.3 Energy-Dispersive X-Ray Spectroscopy . . . 15
4.4 X-Ray Photoelectron Spectroscopy . . . 17
4.5 Secondary Ion Mass Spectrometry . . . 19
4.6 Rutherford Backscattering Spectrometry . . . 23
4.7 Elastic Recoil Detection Analysis . . . 27
4.8 Comparison . . . 30

5 Structural Characterization 32
5.1 Grain Size Calculations . . . 32
5.2 Transmission Electron Microscopy . . . 36
5.3 Focused Ion Beam . . . 42
5.4 Scanning Acoustic Microscopy . . . 49
5.5 Comparison . . . 52

6 State of the Art in Micro-Connect Characterization 53

7 Materials and Methods 57
7.1 Sample Preparation . . . 57
7.2 Grain Revelation by FIB . . . 60
7.3 TEM Lamella Preparation . . . 61
7.4 Practical Advice for FIB Helios 600 . . . 63

8 Results and Discussion 64
8.1 Structural Analysis . . . 64
8.1.1 FIB . . . 64
8.1.2 SEM and TEM . . . 72

8.1.3 GHz-SAM 77
8.2 Impurity Analysis 80
8.2.1 STEM-EDX 81

9 Conclusions 86

References 88

A Appendix 102

B Appendix 103

C Appendix 105

Symbols and abbreviations

Symbols

E_K	Initial binding energy
E_{L1}	First outer shell energy
$E_{L2,3}$	Second outer shell energy
ϕ	Work function of the instrument
hv	Energy of an X-ray
E_B	Binding energy
E_K	Kinetic energy
I_M	Total ion count of the matrix
I_D	Total ion count of the element
N	Number of grains per square inch when the magnification is 100x
n	Grain size number (ASTM)
N_A	Number of grain sections per unit test area
$\overline{A}$	Mean area of the grain section
$\bar{d}$	Mean grain diameter
$\bar{l}$	Mean liner intercept
$\overline{D}$	Spatial diameter of sphere
D_0	Initial grain size
D	Grain size at time t
n	Grain growth exponent
k_0	Grain growth constant
E_a	Activation energy
R	Gas constant
N_T	Atomic density
q	Electron charge
$Y_S(\theta)$	Sputtering yield
θ	Incident angle

Abbreviations

3D	Three dimensional
ADF	Annular dark field
AES	Auger electron spectroscopy
ALD	Atomic layer deposition
ASTM	American society for testing and materials
BE	Binding energy
BF	Bright field
BGA	Ball grid array
BSE	Back-scattered electron
CERD	Coincident elastic recoil detection
CMA	Cylindrical mirror analyser
CMP	Chemical-mechanical planarization
CTE	Coefficient of thermal expansion
D2D	Die-to-die
DOF	Depth of focus
EBSD	Electron backscatter diffraction
EDX	Energy-dispersirve X-ray spectrometry
EELS	Electron energy loss spectroscopy
ERDA	Elastic recoild detection analysis
F2B	Face-to-back
F2F	Face-to-face
FEG	Field emission gun
FESEM	Field emission scanning electron microscope
FIB	Focused ion beam
FWHM	Full width at half maximum
GIS	Gas-injection system
HAADF	High-angle annular dark field
HRTEM	High-resolution transmission electron microscope
HSA	Hemispherical sector analyser
IBL	Ion beam lithography
IC	Integrated circuit
ICP-AES	Inductively coupled plasma atomic emission spectroscopy
IMC	Intermetallic compound
IMPF	Inelastic mean free path
IoT	Internet of things
KE	Kinetic energy
KGD	Known good dies
LIM	Linear intercept method
LMIS	Liquid-metal ion source
MEMS	Micro-electromechanical system
NEMS	Nano-electromechanical system
PCB	Printed circuit board
PEG	Polyethylene glycol

PIXE	Particle-induced X-ray emission
RBS	Rutherford backscattering spectrometry
RSF	Relative senstivity factor
RT	Room temperature
SAED	Selected area diffraction
SAEM	Scanning auger electron microscopy
SAM	Scanning acoustic microscope
SDD	Silicon drift detector
SEM	Scanning electron microscope
SIMS	Secondary ion mass spectrometry
SiP	System-in-package
SLID	Solid-liquid interdiffusion
SoC	System-on-chip
SPS	Bis-(3-sulfopropyl)-disulphide
STEM	Scanning transmission electron microscopy
TEM	Transmission electron microscopy
ToF	Time-of-Flight
TRIM	Transport of ions in matter
TSV	Through-silicon via
UBM	Underbump metallization
W2W	Wafer-to-wafer
WLP	Wafer-level packaging
XPS	X-ray photoelectron spectroscopy

1 Introduction

The demand for reduced power consumption, higher bandwidth, and greater interconnection density has gradually migrated the microelectronics industry towards three dimensional (3D) integrated circuits (3D ICs). Through-silicon via (TSV) has been attracting much attention as a novel technology for 3D ICs as TSV technology can reduce interconnection lengths by employing vertical electrical routing that passes through dies. [1] As it happens, 3D packaging is much more than TSVs since the interconnections between stacked wafers or dies have a crucial role as stacking multiple dies is not possible without interconnections.

In face-to-back (F2B) stacking, the interconnection pitch is limited by TSVs as the device layers are not facing each other. In the face-to-face (F2F) stacking, the bandwidth is limited by the interconnection density since the bottom device layer is facing up. Therefore, reduced pitch is one of the top requirements for 3D interconnects. [2] Alternative novel technologies have been suggested to reduce the interconnection pitch from 40 μm to sub-20 μm. Some examples of these technologies are μ-inserts, μ-tubes, and Solid-Liquid Interdiffusion (SLID) bonding. [3] These new technologies have similar reliability issues as older technologies such as microbumps. For example, it is known that Cu-Sn SLID bonds are susceptible to failures under thermal cycling (TC). The reliability issues can be assumed to be, at least partially, due to fractures initiated by Kirkendall voids [3]. However, the reliability of SLID bonds depend on the material choices since Ni-Au-Sn based SLID bonds may withstand even 3000 cycles of thermal shocking [4].

Kirkendall voids are not unique defects for only SLID bonds but a universal problem with the joining of metals with different diffusion rates. Kirkendall voids weaken the thermal, electrical, and mechanical properties of a solder joint [5]. However, due to the large volume of BGA solder joints, Kirkendall voids have not had a significant impact on reliability. The trend towards micro-connects below 10 μm has given rise to new reliability problems, for instance, in automotive applications that have to withstand varying temperatures. The general consensus regarding the root cause for Kirkendall voids is the difference of interdiffusion rates between the solder and underbump metallization (UBM). Any factors changing the rate of interdiffusion could promote Kirkendall void formation, such as electromigration and thermomigration. [5] A small fraction of researchers suggest that in the case of the Cu-Sn system, Kirkendall voiding should be renamed since it is not caused by the Kirkendall effect, but by the impurities embedded in copper from electroplating. [5–7]

As the root cause for Kirkendall voiding is not yet clear, the aim of this thesis is to compare the characterization methods for micro-connects, especially from the perspective of Kirkendall voiding. The thesis introduces and compares techniques for impurity analysis and microstructural evaluation. Some of the introduced tools are used, and the results will be presented at the end of the thesis. Based on the analyzed results, there will be a discussion about which theory regarding Kirkendall voids seems strongest. The conclusion summarizes the main results of the work.

2 3D Integration

The micro- and nano-electromechanical system (MEMS/NEMS) industry benefit from advanced 3D ICs and wafer-level packaging (WLP) since the functionality of single component can be increased. Functional diversification is called "More than Moore" while conventional Moore's law is about downscaling dimensions of ICs and memory chips. Internet of things (IoT) is one of the major driving forces for the development of 3D ICs as consumers demand more functionality packed on a smaller space.

There exist various technologies which can be used to integrate diverse electronic functions into subsystems. Currently, the most used are System-on-chip (SoC) and System-in-package (SiP). SoC combines all the divergent functions into a single chip, whereas SiP combines multiple chips into a single package. The difference of SoC and SiP is shown in Figure 1. However, SiP and SoC are not mutually exclusive, but they can co-exist in the same system. Nevertheless, the functionality and performance of SoC or traditional SiP might not be enough for future applications. Since novel applications require more integration in smaller space, the electronics industry is migrating towards 3D integration with the SiP approach. The reason is that SoC causes chips to grow very large decreasing the yield. Secondly, using a single chip forces same scaling for all the function blocks even though not all have to be scaled. In contrast, each block can be scaled at a different rate with the SiP approach. The modern SiP approach for 3D ICs relies on TSVs, interposers, micro-connects, and different die stacking schemes. Ultimately, the final objective is to integrate and miniaturize all components under one system, called System-on-package (SoP) which is shown in Figure 2. [8]

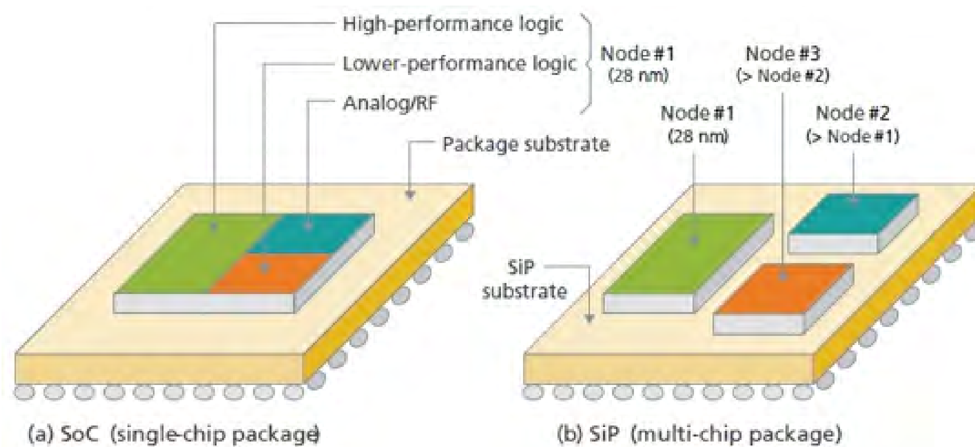

Figure 1: The fundamental difference between SiP and SoC is the amout of dies. The SoC approach includes only one chip that has multiple functions and the SiP approach includes multiple dies stacked or side by side. [9]

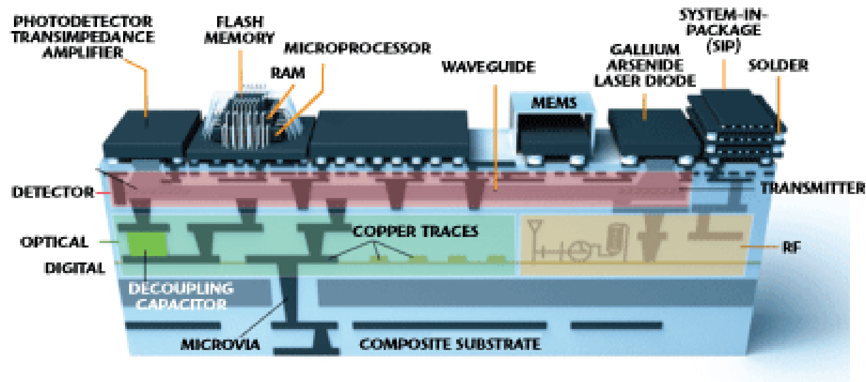

Figure 2: The ultimate objective is to blur the limits between dies, package and the substrate. [10]

The two approaches for 3D stacking are bonding at the wafer level or at the die level. The die level bonding includes die-to-die (D2D) and die-to-wafer (D2W) bonding. Typical wafer-to-wafer (W2W) bonding uses either a oxide or metallic bond, such as direct oxide bond or SLID bond. Variations may involve the use of a polymer or adhesive to improve bond characteristics. [11]

The W2W approach requires same die sizes on both wafers and a relatively high wafer yield since the yields are multiplied when stacking multiple wafers (e.g. $0.99 * 0.99 * ...$). Furthermore, the bonding process is sensitive to topographical variations since the bonding area is considerably large. The final thickness of the top wafer can be in the range of 10 μm since wafers are usually thinned and the TSVs formed after bonding. Therefore, the TSV length can be minimized to 10 μm and the W2W bonding is well suited for fine pitch applications since the aspect ratio limitation of TSVs is not a concern and alignment for wafers is more accurate than with other methods. [11]

D2D bonding has lower throughput than W2W bonding but D2D is not limited by the dimensions of the die and the wafer. Furthermore, the yield is not a concern for multiple stacks since only known good dies (KGD) can be used. Also, D2D resembles a more standard chip assembly than a microfabrication technique. The TSVs are usually manufactured after bonding and due to the handling issues, the thickness of a single die is typically 50-100 μm. The TSV depth is on the same range increasing the interconnection pitch since the TSVs can be narrow. Consequently, the increased pitch limits the usage of D2D bonding for applications requiring fine pitch. An example of D2D bonded structure is shown in Figure 3. [11]

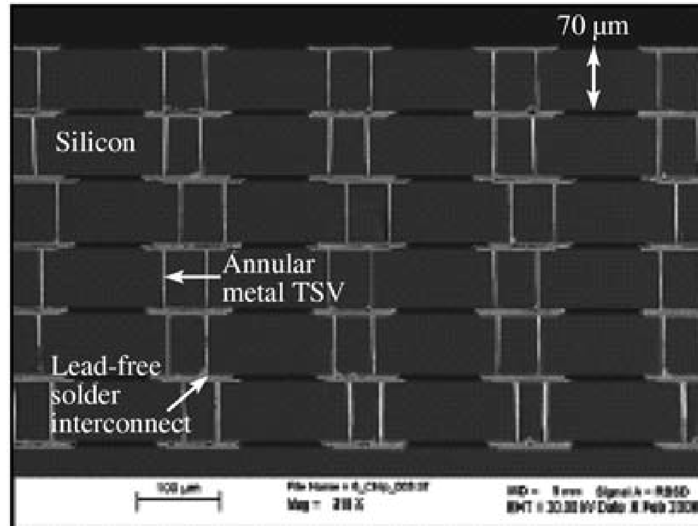

Figure 3: D2D bonding can be used to form a stack of dies connected with micro-connects. The dies are relatively thick and the pitch is limited. [11]

D2W bonding is a combination of D2D and W2W bonding. In the D2W approach, multiple dies are placed on the wafer and joined simultaneously. The throughput is high and the yield is not an issue. D2W stacking is actually more cost effective than W2W stacking and the alignment accuracy is relatively good. [8, 11]

No matter what stacking scheme is used, interconnections are required between the chips. Although there exists a broad range of various platforms for 3D interconnections, they are all limited by the same dimension constraints, cost, and reliability requirements. Bonding interfaces are susceptible to failures as intermetallic compounds (IMCs), which may be brittle, are a large fraction of the volume, a combination of different materials cause thermal issues related to the Coefficient of Thermal Expansion (CTE) mismatch and electromigration causes new issues in the small volume interconnections [12]

The primary bonding methods are direct copper-copper bonding, eutectic bonding and soldering. One popular approach in 3D IC interconnection manufacturing is bonding by lead-free solder bumps or copper pillars that can be manufactured by conventional mass-reflow or thermocompression. The diameter of those microbumps is one order of magnitude smaller and the volume can be 1000 times smaller than that of the flip-chip solder joints. The number of grains in a single solder joint becomes small and the microstructure of the solder joint can be considered to be anisotropic. That means that properties of each microbump can be different causing a large spread in lifetime distributions. Therefore, it is desirable to have a similar microstructure in each microbump. Furthermore, the relative amount of IMC is greatly increased if parameters used in the traditional flip-chip reflow process are adopted for the microbumps. On top of that, the solder thickness has been reduced more than the thickness of the UBM. In some scenarios, the entire microbump is completely transformed into intermetallics causing new reliability problems or unexpected behaviour. [8, 13]

Metal alloys that are based on Cu,Ni,Sn or Ag are probably the most used

materials for the micro-connects in 3D IC applications. The Ni diffusion layer between Cu and Sn reduces interdiffusion and formation of Sn whiskers, but it makes the micro-connect more brittle due to formed $(Cu, Ni)_6Sn_5$. In addition to the thermocompression and the reflow process, SLID bonding is emerging as a very reliable future technology for micro-connects. SLID bonding is based on the fact that the melting point of the IMC is higher than that of the solder itself. The IMC growth is carefully controlled during the bonding process to increase the joint reliability. SLID bonding is a thermocompression type bonding process that can be done at relatively low temperatures. Therefore, the process can be repeated to stack multiple layers without remelting the lower level bonds. For these reasons SLID bonding has drawn much attention. [8, 13]

Pb-free solders in combination to a copper UBM are not without problems. Pb-free solder is usually harder than eutectic Sn-Pb solder reducing the stress absorption of the solder joint. [13] Furthermore, electroplated copper contains impurities that might participate in void formation on the interface of Cu_3Sn and electroplated Cu. That is a real concern since one of the most important property of a solder joint is the strength. An example of a non-reliable micro-connection bonded by SLID is shown in Figure 4.

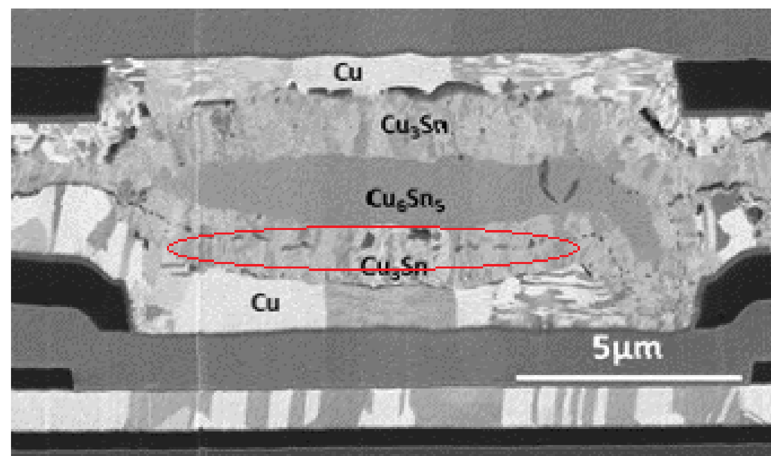

Figure 4: A micrograph of a Cu-Sn SLID bond. Kirkendall voids are visible inside Cu_3Sn and between the Cu_3Sn and Cu. The voids decrease the strength of the joint and might cause electrical failures. [3]

Ball Grid Array (BGA) solder joints and flip-chip technologies are not yet obsolete. BGA is used for connections between the package substrate and printed circuit board (PCB), and the flip-chip is used between the interposer and the substrate. However, the size of the solderbumps between the interposer and the substrate is decreasing towards the size of the micro-connects. The different interconnection levels are shown in Figure 5.

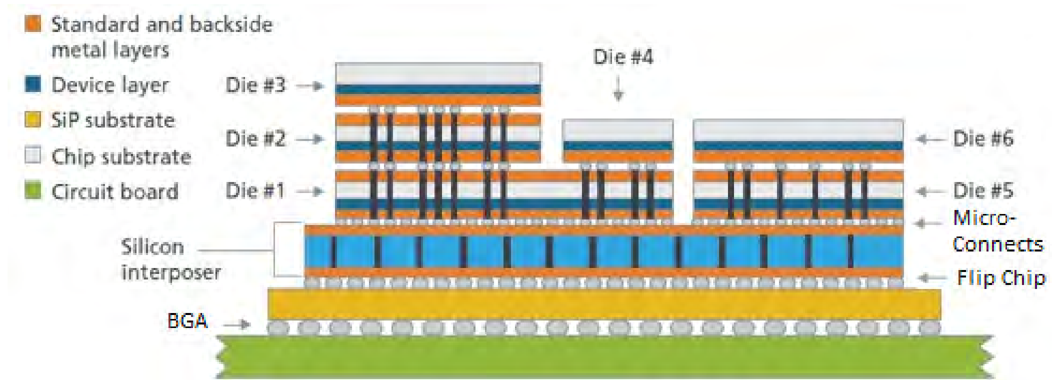

Figure 5: The package contains different level interconnections. BGA solder joints are used between the PCB and substrate, flip-chip between the substrate and interposer and micro-connects between the dies. [14]

3 Research Question

The impact of Kirkendall voids on the reliability and mechanical properties will become even more critical in the micro-connects. The reason is that the size of Kirkendall voids can be a large fraction of the volume of a micro-connect itself. The focus of this thesis is in the micro-connects, especially in characterization methods related to Kirkendall void research. It is known that several factors influence Kirkendall voiding such as impurities, grain size, film thickness, additional layers, and electroplating parameters. [3, 5, 7]

Furthermore, it has been shown that post-deposition annealing suppresses Kirkendall voiding formation due to outgassing of organic impurities [15, 16]. That gives even more proof that the voiding effect is not due to the Kirkendall effect but due to organic impurities. However, the main culprit has been usually claimed to be sulphur content [15, 17–20], but there is not yet strong evidence to support this conclusion. The relation between electroplating bath chemistry and Kirkendall voiding is complicated. The known fact is that the organic additive molecules and their derivatives can be incorporated into the metal film during the electroplating. Furthermore, it has been shown that different additives, current density, and age of the plating bath can directly affect the voiding propensity individually. [20]

Sulfide-forming elements such as Zn, Mn and Cr are shown to suppress Kirkendall voiding due to suppression of S adsorption on the void surface [19]. However, that claim might be questionable due to insufficient chemical analysis and lack of consideration of other impurities that may participate, such as O, C, and Cl. Similar to the S, the Cl may form chlorides with those sulfide-forming elements.

Since it is not clear which factors are dominant, several characterization methods are required to study Kirkendall voids and the root cause(s) for their growth. It is not enough to understand just the characterization methods, but to study the micro-connects and their manufacturing methods as a whole. The main question is that why Kirkendall voids form? Research is required to obtain the answer and for that different characterization techniques are required. Testing and a comparison of different techniques is time-consuming; thus there is a need for comparison of characterization methods. This thesis compares different characterization methods related to micro-connects and Kirkendall voids from the standpoint of limitations, ease of use, quality of data and time efficiency. Since there should be a link between impurities and Kirkendall voids, the most important techniques are related to impurity analysis and structural analysis.

4 Impurity Analysis

Currently used electroplating methods do not produce pure copper, as seen in Table 1. The table shows impurity measurements in at.% for electroplated copper from various references. However, Table 1 is not precise as some of the results had to be interpreted from graphs or the total copper amount was calculated based on the total amount of impurities. Secondly, some of the results were not used for calculation of the average since they seemed not to be reliable. Additionally, results that contained an excess amount of carbon and oxygen were discarded since the measurement or deposition is not probably successful. The depositions with a high level of Zn should also be discarded since the copper electrolytes do not contain Zn. Table 1 suggests that electroplating incorporates at least carbon, oxygen and nitrogen in the films. Additionally, for the electroplated copper, most of the concerns rise from the Cl and S concentration. If more additives are used in the bath chemistry, there are more different contaminants in the copper film. However, that does not necessarily mean that the total amount of impurities is higher.

Table 1: Tabulated impurity measurements in at.% for electroplated copper from various references. Concentration data showing less than 85 at.% Cu were omitted in the literature review.

Tool	Cu(%)	O(%)	C(%)	Cl(%)	Zn(%)	S(%)	Ref.
EDX	85.00	1.00	7.00	–	7.00	–	[21]
EDX	89.00	2.00	5.00	–	4.00	–	[21]
SIMS	87.10	7.30	5.60	–	–	–	[22]
SIMS	99.90	0.01	0.02	0.05	–	0.005	[23]
SIMS	94.60	2.20	1.80	1.30	–	0.10	[24]
SIMS	97.40	1.00	1.00	0.50	–	0.10	[25]
Average	92.20	2.20	3.40	0.60		0.10	

As seen in Table 1, the impurities in electroplated copper are usually measured by secondary ion mass spectrometry (SIMS) or energy-dispersive X-ray spectrometry (EDX). Unfortunately, EDX is not a reliable technique for lighter elements which is discussed in Section 4.3. The unreliability of EDX for impurity analysis is confirmed by C-H. Liao [21] by X-ray photoelectron spectroscopy (XPS) measurements that showed copper purities over 90 at.%, whereas EDX measurements for the same samples showed copper purities of 85-89 at.%. The SIMS analysis by D.L. Malm and M.J. Vasile [22] were done for surface-etched samples. The etching removed contaminants, such as Cl and S. Without etching, the copper surface contained $\sim$3 at.% Cl and S. Additionally, the surface etching did not decrease the amount of O, but the amount of C was drastically decreased. The measurements by K. Denn et al. [26] confirm that the impurities such as Cl and S are mostly located on the surface of the copper and not in the bulk. However, the initial location of the impurities is not yet clear since impurities could diffuse to the surface during even a short storing time at the room temperature. The measurements by Q. Huang et al. [23] differ greatly from the other results since all their measured impurities are in a ppm range.

Therefore, the results should be treated with caution. In conclusion, purity of 90 at.% could be considered a good standard for quality electroplated copper. Additionally, depending on the measurement and bath chemistry, the electroplated copper will probably contain ∼2 at.% C, ∼3 at.% O, and less than 1 at.% Cl and S. This section reviews popular and less known tools for impurity analysis. The reviewed tools were chosen by the ability to locate the impurities in a specimen and by the ability to analyse solid samples. The section is finalized by a comparison that attempts to evaluate the best choice among the reviewed tools.

4.1 Auger Electron Spectroscopy

The Auger effect was discovered by Pierre Auger in 1923, but the first commercial Auger electron spectroscopy (AES) instruments were introduced in the late 1960s. [27] AES analyses the kinematic energy of Auger electrons which are ejected when a system with an electron vacancy relaxes. The vacancies are usually produced by 5-25 keV electron beam by ejecting an electron from an inner K-shell. [27, 28] The process can be written as a simplified equation:

$$E = E_K - E_{L1} - E_{L2,3} - \phi, \quad (1)$$

,where E_K is the initial binding energy, E_{L1} first outer shell energy, $E_{L2,3}$ second outer shell energy, and ϕ the work function of the instrument. The equation resembles that of XPS. However, the equation is a simplified expression due to transition probabilities between double ionized states, multiple excitations and Coster-Kronig transitions. The measured kinetic energy is usually in the range of 50-2500 eV. [27] An example of the transition is shown in Figure 6 [29].

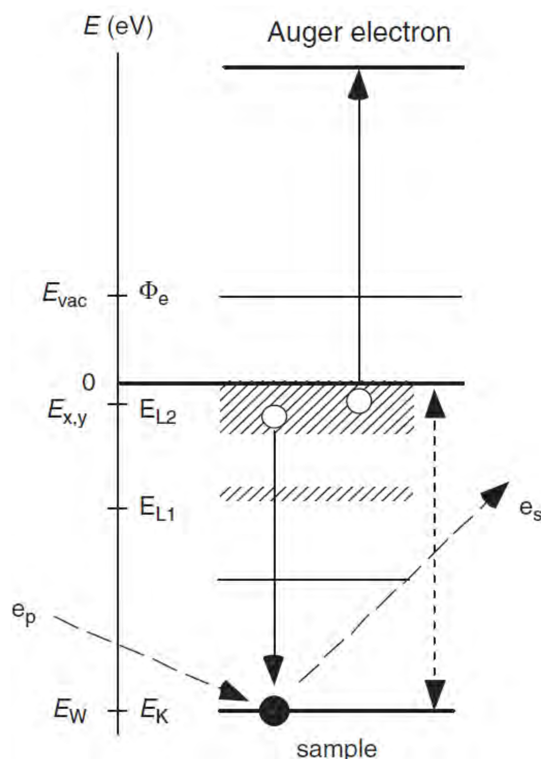

Figure 6: An electron is removed from the K-shell by the electron beam and the vacancy is filled by an electron from an upper shell. To balance the upper shell, an Auger electron is emitted from the same shell from where the electron was relaxed. [29]

The Auger transition is characterized by the presence of the core hole and location of the two final states. [29] AES instrument consists of an electron gun, an ultra high vacuum chamber and an electron detector. [27] The electron source is similar type than in scanning electron microscope (SEM) such as field emission gun or thermionic tungsten source. The detector is usually either cylindrical mirror analyser (CMA) or hemispherical sector analyser (HSA).

AES can refer to a conventional point analysis technique, or a scanning technique called scanning auger microscopy (SAEM) that is analogous to SEM. Furthermore, SEM-EDX and SAEM has similar scanning speeds to acquire elemental maps. Similar to SEM-EDX, SAEM can be used to scan line and mapping profiles. The major difference between SEM-EDX and AES is the interaction volume since the Auger electrons are emitted from the surface. Generally, SAEM uses a smaller beam diameter than the point analysis AES. However, the scanning mode is not acquired without disadvantages. The change of slope during the scanning changes the detected intensities and the background intensity, especially if the incident beam size is small. However, the most drastic intensity changes can be corrected using BSE detectors. Secondly, it is challenging to use scanning mode for structures that have sharp edges or wells that will cause shadowing and trapping of Auger electrons. Moreover, typical SAEM instrument has a beam size of 10-20 nm that can detect a few hundred atoms simultaneously. The spatial resolution limitations are mainly caused by radiation

damage and topographical effects. [27]

The major advantage of AES is the extreme surface sensitivity that is similar to XPS. The surface sensitivity emerges from the 0.3-3 nm inelastic mean free path (IMPF) of electrons. The IMPF depends on the electron kinetic energy (composition) and incident electron energy. [27] AES is a three electron process, whereas XPS is one electron process. In that sense, XPS peaks are easier to fit. Furthermore, since at least three electrons are required for the Auger process, AES is not compatible with elements $Z < 3$. In addition, unwanted inelastic collisions produce low energy backscattered electrons that contribute to the AES spectrum and they are regarded as background intensity or noise. Therefore, the Auger spectrum contains a high amount of unwanted noise that should be eliminated by the peak fitting. An example of AES spectrum is shown in Figure 7. [29]

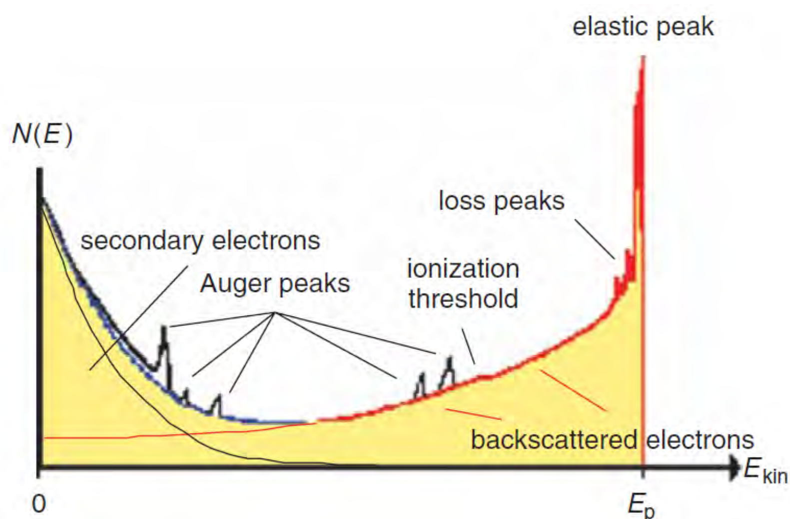

Figure 7: The Auger electron peaks are only a small part of the spectrum. The spectrum is dominated by noise from the backscattered electrons. The elastic peak is caused by the electron beam and it is used for calibration. The loss peaks near the elastic peak are related to ionization levels. However, the spectra do not contain photoemission peaks. [29]

The probability of creating core-hole electron depends on the e-beam energy and core hole binding energy. The rule of thumb is that the maximum probability is reached when the incident beam energy is three times higher than the core hole binding energy. However, the probability is different for different elements. For example, Auger process in light elements is very probable in contrast to X-ray emission as seen in Figure 8. [29]

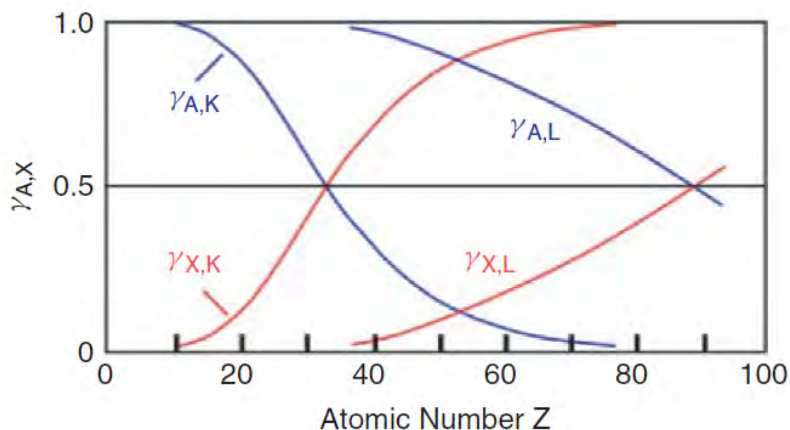

Figure 8: The yield per shell vacancy of X-rays (X) and Auger electrons (A) in relation to atomic mass number. The probability for Auger electron emission is relatively good for a whole range of elements. As can be seen, the probability for X-ray emission in light elements is low and that causes problems when EDX is used. [29]

AES can be used to acquire different types of spectra. The most popular ones are the first derivatives of the electron energy distribution since the chemical shifts and spectral quantification are simple to analyse in the derivative mode. Although, the derivatives are restricted to samples that do not cause a change in the peak shape. However, the derivative spectra are not necessarily comparable to spectra acquired by other AES tools. These disadvantages can be minimized if a direct spectral mode is used. The direct spectral mode acquires spectra using an incident beam in a nanoamp range and the Auger peak intensity is directly related to the chemical composition when the background noise is removed. [27]

Similar to XPS, AES can be used for probing the electronic structure. The transitions are mainly ionization of a core level followed by decay from the valence band. These shifts can be used to identify different chemical states of an atom, but they might introduce a systematic error in the results if the derivative mode is used. Nevertheless, due to the three electron process, the data is more difficult to handle and fit than with XPS and the results are not directly comparable. [27] Therefore, AES is usually used for purely atomic identification since the chemical shifts are complex.

Doing depth profiling by AES is possible. The maximum depth for electron transmission is three times the wavelength. For example, if the incident electron energy is 500 eV, the maximum depth is ∼7.5 nm. This approach requires tilting the specimen in various angles and it is widely used with XPS, but that will not give reliable results with AES since the backscattering factor will change. To increase the analyzed depth, there is need to use a destructive method, such as sputtering by Ar^+ ions. The most important parameters that influence the depth resolution during the sputtering are atomic mixing, surface roughness, and sputtering depth. [30, 31]

The major disadvantage of AES is the surface charging in insulating materials.

The charging shifts and distorts the acquired spectrum. However, thin dielectric layers can be investigated if the substrate is conductive due to the low voltage drop between the vacuum/dielectric and dielectric/substrate interfaces. Furthermore, electron beam might damage sensitive samples similar to SEM. [27]

Auger peaks are generally broader than XPS peaks. Therefore, the analyzer can be lower resolution and angular collection efficiency is not a problem. In addition, AES is faster than XPS, but misuse of relativity sensitivity factors might produce a big error in the results. The lateral resolution of AES is 10-100 nm and detection limit is 0.1 at.% [30] However, there is a trade-off between lateral resolution and capability for quantification. Improved lateral resolution requires a smaller incident beam that is consequently weaker decreasing the signal-to-noise ratio. Since the beam diameter is smaller, the acquisition speed has to be increased to keep the measurement time reasonable. These properties hinder the capability for accurate quantification if the tool is set to improved lateral resolution. [27] The quantification should be improved further by using a reference library of intensities corresponding to elemental concentrations at the surface. [27] Furthermore, AES requires a smooth surface and in the best-case scenario, the sample would be amorphous since quantitative analysis suffer from the channelling effect in the crystalline samples. [27]

4.2 Electron Energy Loss Spectroscopy

Electron energy loss spectroscopy is used to study chemical, physical, and optical properties of the materials and it is usually integrated with (scanning) transmission electron microscope ((S)TEM). In contrast to (S)TEM imaging, EELS is based on detecting inelastically scattered electrons. The energy loss due to the inelastic scattering is specific to each bonding state of each element. The method is suitable to extract information about composition and bonding. The acquired spectrum consists of zero-loss, low-loss, and core-loss regions as shown in Figure 9.

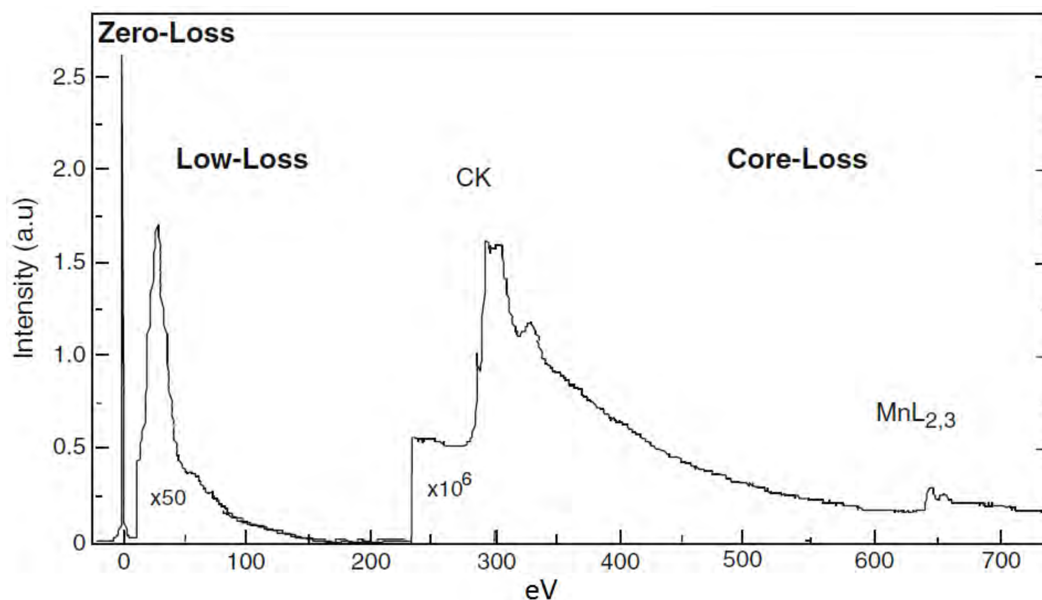

Figure 9: The spectrum is divided into three parts. The zero-loss peak is the reference energy, the low-loss peak is characteristic to the optical properties, and the core-loss region is used for elemental analysis. [32]

The zero-loss peak is used as a zero reference energy since it is the signature peak for all the electrons that have elastically passed through the sample. The low-loss region is characteristic to the optical properties of the sample and it can be separated into bulk and boundary groups. The bulk group consists of optical gap transitions, such as bulk plasmons and semi-core losses. The boundary group consists off the surface (plasmon) and Begrenzung effects. Altogether, the low-loss region can be used to evaluate the optical properties of the sample. [32]

The core-loss region typically exists beyond 100 eV and it is usually independent on the boundary effects. The core-loss signal can be used to interpret electronic transitions. The transition energy is close to the ionization energy with an accuracy of a few electron volts. The area under the edge corresponds to the amount of detected atoms if the geometrical conditions are known. The electronic structure is derived from the region near the edges since it contains information about the electronic structure, bonding, and valence. Furthermore, the spectrum can be used to calibrate energy filters for energy filtered (S)TEM imaging. [32]

EELS spectrometer is usually a magnetic prism that disperses the inelastically scattered electrons as a function of energy, but it does not change the electron trajectory. In addition to a spectrometer, EELS uses a lens system to align and focus the spectrum in the detector plane causing some energy loss. However, EELS requires a high brightness electron source such as cold FEG and the required sample thickness (usually ~50 nm) depends on the analyzed materials. [32]

4.3 Energy-Dispersive X-Ray Spectroscopy

EDX is a technique for chemical characterization of a sample. Commonly, EDX is integrated with SEM and it is used as a chemical analysis technique while SEM is used for structural characterization. EDX relies on the interactions between the electron beam and the specimen which emits characteristic X-rays in response to the electron beam. An electron from an inner shell is excited by an electron beam producing a vacancy and the vacancy is subsequently filled by an electron from the outer shell and an X-ray is emitted. The characteristic transitions are named according to the shell in which the electron is ejected and the shell from which electron is relaxed. For example, if electron drops from L-shell to K-shell, a Kα X-ray is emitted. [33] The number and energy of the X-rays are measured by an energy dispersive spectrometer. However, to accurately measure the material, all detectable transitions should be present in the spectrum.

Continuum (Bremsstrahlung) background noise is generated by the interaction between the e-beam and atom nucleus in addition to the characteristic X-rays. The distribution of continuum X-rays is not characteristic to the material and it is considered as a nuisance. Since the probability of electron beam reaching the nuclei of lighter atoms is high, more background noise is generated by lighter elements than by heavy elements. The electron beam energy should be over critical excitation energy to ionize an atom. Besides, inner shells have lower binding energy than the outer shell and each shell has its own binding energy that has to be exceeded. However, the difference in the energy is higher in transitions between inner shells than transitions between inner and outer shells. [33]

Usually, EDX uses Si(Li) detectors that convert the energy of each X-ray to a voltage by ionizing atoms in the silicon. To increase the signal-to-noise ratio, the detector is usually cooled by liquid nitrogen and the accumulated charge is periodically restored to prevent saturation. However, the detector causes peak broadening due to its response function, peak distortion due to trapping, escape X-rays, and sum peaks due to pulse pileup. However, new silicon drift detectors (SDD) have emerged which do not require cooling while offering superior performance. [34]

The detector itself is not the main reason for inaccuracy or inability to detect light elements. The inherent problems are related to the generation of X-rays and high interaction volume. EDX is not a surface characterization technique, but it gives an average composition based on the volume of the penetrated electrons that is approximately 1 μm deep and wide as seen in Figure 10. In addition to the high interaction volume, the X-ray emission in light elements is dominated by Auger emission that is used by AES. Furthermore, X-rays generated in lighter elements are easily absorbed since they are weak. Due to the absorption, the information is mostly acquired from the surface which is especially problematic if the surface is contaminated. Moreover, reliable analysis requires acquiring all possible transitions that might overlap in the spectrum reducing the possibilities for quantification. [33]

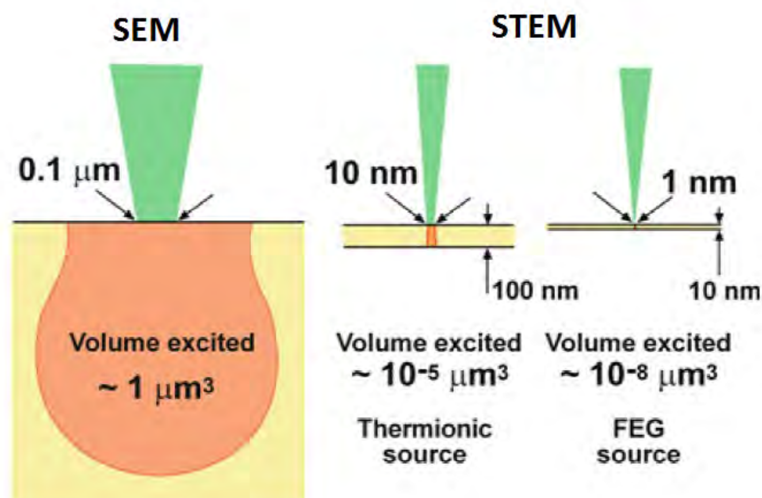

Figure 10: The accuracy of SEM-EDX is low since the interaction volume is high. If (S)TEM-EDX is used, the interaction volume is determined by the sample thickness and electron beam size. [32]

To provide best conditions for the EDX analysis, the sample should have flat surface, the acceleration voltage should be high enough, there should be no surface contaminations, and the material should be homogeneous. Although, even the best conditions do not provide real quantitative analysis since the data should be handled by a correction matrix that takes into account lost energy due to penetration, absorption of the X-rays, and secondary fluorescence. If the correction parameters cannot be used, at least the prefabricated profiles in the measurement software should be tested. [35]

EDX offers a possibility to carry out spot analysis, line analysis, and chemical mapping. However, the detection limit is approximately 0.1-1 at.% depending on the sample type. The spatial resolution is $\sim$1 μm for heavy elements and $\sim$5 μm for light elements. The inaccuracy between repeated measurements is less than 5 %. Reliable information of the chemical composition can be acquired if the elements are heavier than Z $>$ 3-11 depending on the used tool. [33]

EDX is quick, versatile, and widely available. For these reasons, it is especially suitable for qualitative analysis. However, due to the reviewed limitations, the tool cannot be used for depth profiling or trace element analysis and the accuracy is reasonably low for lighter elements. If the analysed area is small and there is a possibility for lamella preparation, (S)TEM-EDX should be used instead.

EDX analysis in (S)TEM is a reliable approach to characterize materials, especially for heavier elements (Z $>$ 30). The spatial resolution in (S)TEM-EDX is determined by incident probe size since the interaction volume is directly proportional to the probe size as shown in Figure 10. However, detection of the generated X-rays is drastically less efficient than detection of energy-loss electrons since the generated X-rays are emitted all around the sample but they are detected only with a few detectors depending on the configuration. Elemental mapping is possible with EDX,

but it is moderately slow since the X-ray maps need to be recorded by pixel at a time for a long dwell time due to the inefficient X-ray generation and detection. [32]

The corrections used in quantitative SEM-EDX do not apply to (S)TEM since the peak intensities are proportional to concentration and specimen thickness that can be presented as a k-factor which is an efficiency curve of the system. An example of (S)TEM-EDX k-factor curve is shown in Figure 11. However, if the sample thickness exceeds 100 nm, density and thickness corrections should be applied to acquire quantitative data. [34]

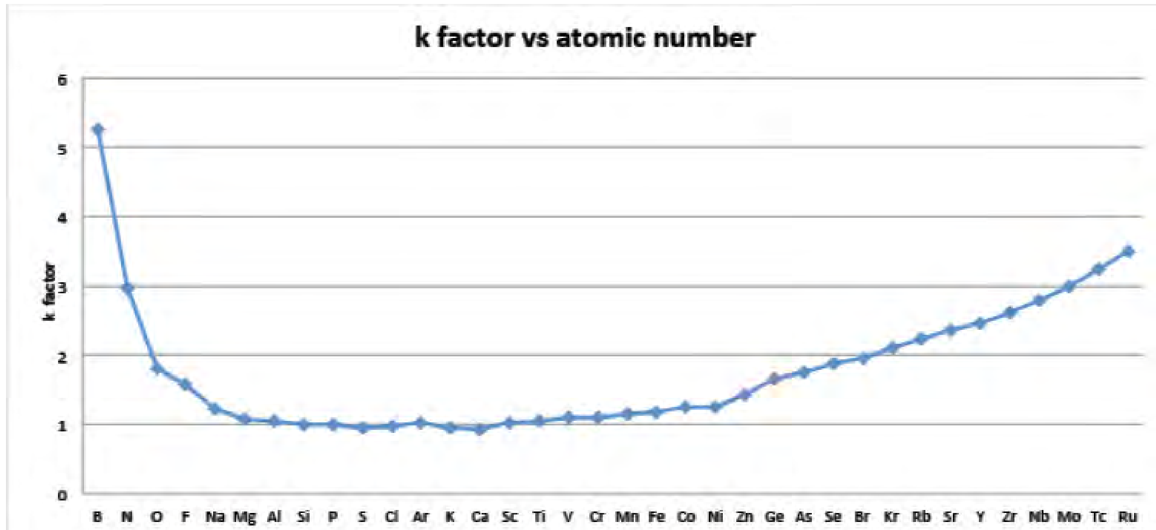

Figure 11: The k-curve shows a low efficiency for light and very heavy elements that is typical for EDX analysis. [34]

4.4 X-Ray Photoelectron Spectroscopy

XPS is probably one of the most used surface analysis technique. It can determine the surface composition and chemical states quantitatively. [31] Experiments that used X-Rays to obtain photoelectrons were reported as early as 1907 [27]. The analysed electrons are ejected from the sample as a result of a photoemission process. Most of the electrons are emitted from the top layer (∼3nm) due to short mean free path of electrons. Typically, an $Al - K_\alpha$ or $Mg - K_\alpha$ primary source is used to generate an X-ray photon that ejects an electron from an inner electron shell of an atom. [30] The kinetic energy (KE) of the ejected electron is measured to obtain a spectrum and the ejection process can be described as:

$$E_K = hv - E_B - \phi, \tag{2}$$

where hv is the energy of the X-ray, E_B is the binding energy (BE) with respect to the Fermi level, and ϕ is the work function of the tool. In other words, the photoemission is a one electron process and which is illustrated in Figure 12. The binding energy can be approximated as an orbital energy and different orbitals give different peaks in the spectrum and the peak intensity depends on the probability

for ionization. Since the core-level binding energies are unique, they can be used as a signature for different elements. However, the spectrum contains extra peaks due to the Auger emission, surface/bulk plasmons, and shake-off events.

XPS can be used to detect chemical shifts that can be described as an addition/deletion of valence electrons that increase/decrease the binding energy. However, the chemical shifting involves more complex effects such as spin-orbit splitting and the Auger electron emission. Analogous to AES, the spectrum contains background noise that is generated by inelastic scattering. [36]

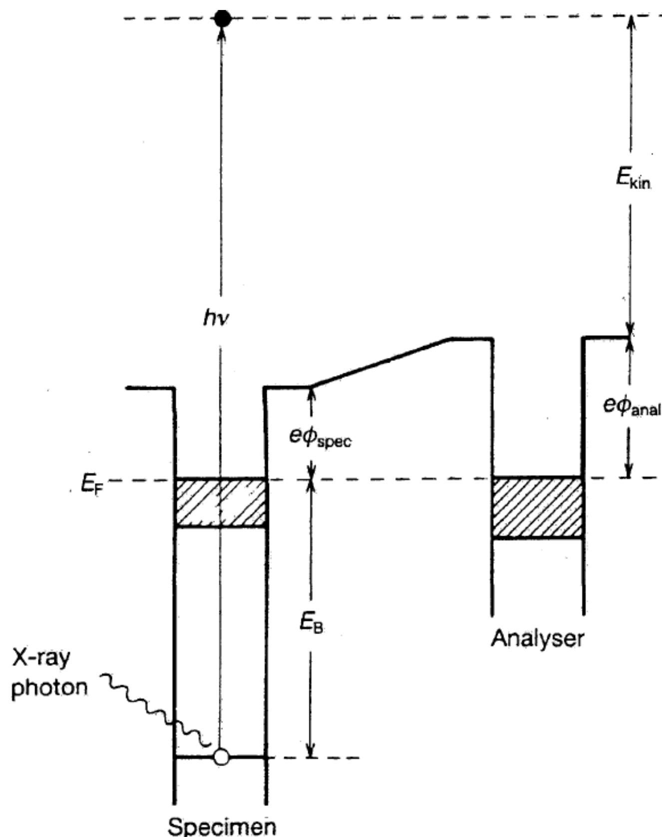

Figure 12: An X-ray photon excites an electron from a core-level. The kinetic energy depends on the X-ray photon energy, binding energy and work function of the tool. [36]

XPS is operated in a high vacuum and the tool consists of an X-ray source, a camera, a lens system, an energy analyzer, and a detector (HSA or CMA). The best energy resolution achieved is approximately 0.28 eV if a monochromator is used. However, there is always a trade-off between energy resolution and sensitivity. [36] Quantitative XPS analysis requires peak fitting and tables of sensitivity factors. Moreover, there exists several different software packages for XPS data handling and peak fitting. Unfortunately, different software might produce different results and accuracies. The vertical alignment of the sample is critical in some commercial instruments since misalignment of 0.1 mm might cause a 10 % error in the spectrum. In addition, the scale of the spectrum should be carefully calibrated so that the scale

differs less than 0.2 eV from the accepted values. The scale can be calibrated by an X-ray source and fitting by a quadratic equation. [31]

Similar to AES, XPS can be used for non-destructive depth-profiling for a maximum depth of three wavelengths. For deeper depth profiles, destructive sputtering is required. Typically used ions are 1-10 keV Ar^+-ions. During depth profiling, the analysis spot should be at the center of the ion beam and the ion beam should be kept constant. Granted, surface roughness and the channeling effect in polycrystalline materials decrease the depth resolution. Furthermore, the sputtering might cause atomic mixing, decomposition and segregation. Similar to SIMS sputtering, the depth profile resolution can be increased by sample rotation or multiple ion beams. [36]

The greatest disadvantage of XPS is the low lateral resolution that is usually in the range of tens of μms. However, the lateral resolution can be increased using a higher X-ray flux by a synchrotron or an X-ray laser. [30, 36] Similar to AES, XPS charges the surface of the sample causing broadening of the peaks. However, the charging is not as severe as with AES and it can be taken into account while fitting the peaks or the charge can be compensated by low energy electron/ion gun. [36]

4.5 Secondary Ion Mass Spectrometry

SIMS is a technique to obtain information about the molecular, elemental, and isotopic composition of the specimen. The sample is bombarded with primary ions resulting in the ejection of the secondary ions from the surface of the sample. Typically, the secondary ions are measured with a mass analyser that produces a mass spectrum with a sensitivity of ppm/ppb. [37] The phenomenon of secondary ion emission had been discovered already in 1915, however, the first SIMS prototypes emerged in the 1940s. [38]

Similar to the focused ion beam (FIB) (reviewed in section 5.3), the sputtering is caused by collision cascade that is based on a momentum transfer between the primary ions and the surface atoms. Likewise to FIB, the ion beam causes surface damage and implantation of the sample. The depth of damaged surface might be in tens of nanometers. However, the major part of secondary ions originates from a depth of 3-6 Å. [38, 39] Additionally, SIMS allows chemical mapping of the surface. [38]

SIMS can be operated either in dynamic or static mode. In the dynamic mode, the acceleration voltage and the current density are high. Due to that, the dynamic mode is suitable for high sensitivity depth profiling. On the other hand, the dynamic mode causes more damage and the spatial resolution is reduced due to the increased beam size. Sputtering rate varies from 0.1 to 100 nm/min depending on the primary ion energy, current density, type of primary ions and the angle of the incidence beam. The depth resolution can be increased by using raster-scanning. [38] An example of SIMS depth profile can be seen in Figure 13. SIMS is capable of identifying all elements in the periodic table, including hydrogen. However, the tool is most sensitive for alkali metals, halogens and oxygen and least sensitive for noble metals. [38] The dynamic SIMS is more sensitive (ppb) than static SIMS (ppm) due to the higher acceleration voltage.

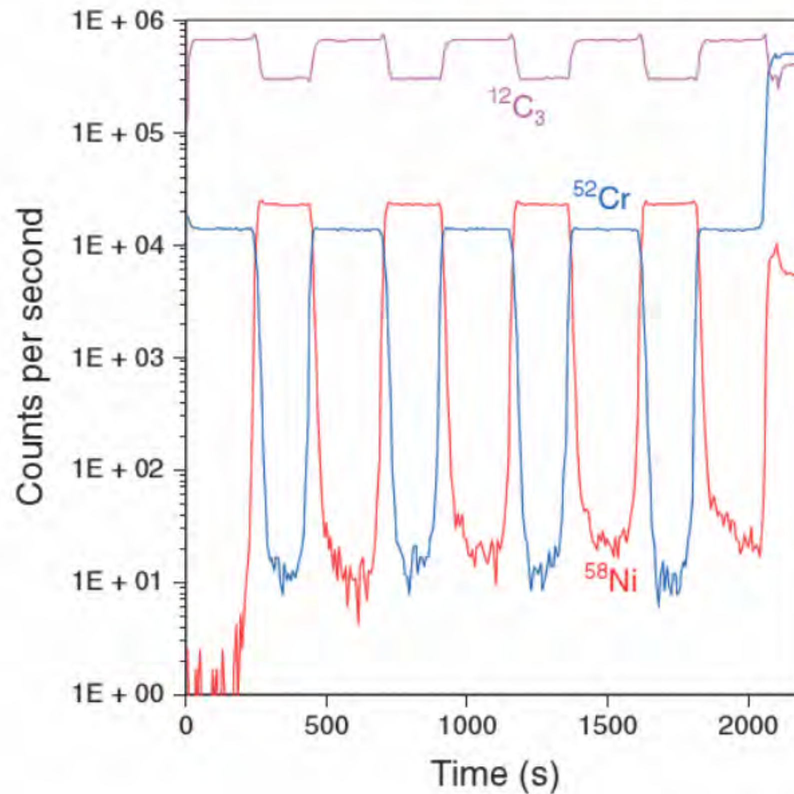

Figure 13: An example of SIMS depth profile of Cr/Ni thin-film stack with nominal thicknesses of 53 and 66 nm. The sharp transition between materials indicates a successful depth profile. An unsuccessful depth profile spectrum would have empty spacings between the transitions. [37]

The static SIMS mode allows non-destructive analysis of the surface layer due to low acceleration voltage and current density. The primary ion beam does not strike the same area twice and the spatial resolution is increased [38]. Furthermore, the total ion dosage is kept under the critical (static) limit and the method is especially suitable for sensitive samples, such as polymers and biological materials. [37]

SIMS instrument consists of an ion gun, a primary ion column, a vacuum chamber with a sample holder, a secondary ion extraction lens, and a mass analyzer that measures mass-to-charge ratio of the secondary ions. The vacuum pressure of 10^{-5} Pa is enough for dynamic SIMS, but the static SIMS requires vacuum pressure over 10^{-8} Pa. [38] An example of SIMS instrument is shown in Figure 14.

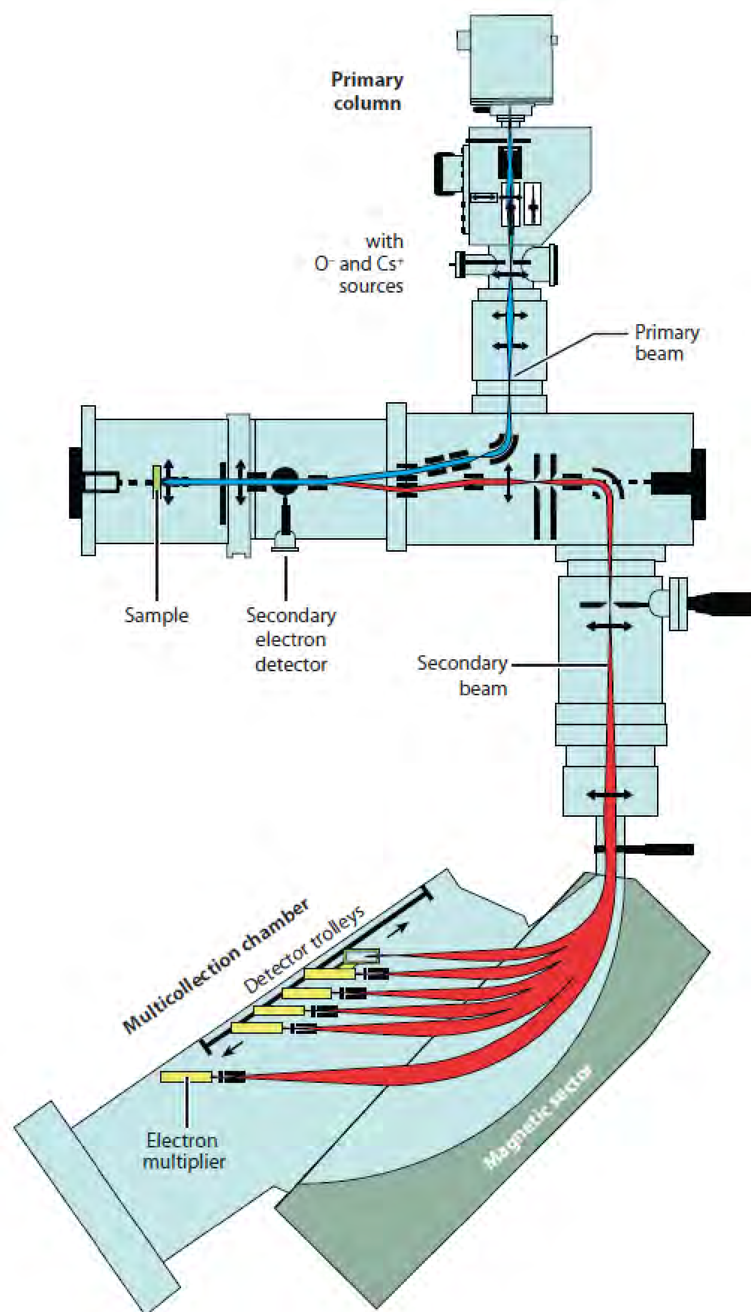

Figure 14: SIMS instrument consists of an ion gun, a primary ion column, vacuum chamber with a sample holder, the secondary ion extraction lens, and a mass analyzer. If the instrument does not use a time-of-flight detector, the amount of different ions detected depends on the amount of the detectors. [40]

Three basic types of mass analyzers are a magnetic sector field, a quadrupole, and a Time-of-Flight (ToF) analyzers. The magnetic sector field analyzer separates the masses by electrostatic and magnetic forces, the quadrupole by resonant electric field and the ToF by the secondary ion velocities. ToF is the only type of analyzer that can detect the whole range of secondary ions simultaneously. All the other analyzer types

require choosing of a specific range of ions to be measured. [38] Modern equipment has, at least, four different secondary ion detectors: an electron multiplier, a Faraday cup, an image plate, and an anode encoder. Some tools might have even 11 different detectors. However, it should be taken into account that not all detectors can be used simultaneously. [41, 42]

ToF analyzer can be used only with static SIMS and it further reduces the surface damage. ToF-SIMS usually uses a pulsed cluster (polyatomic) ion source that is especially recommended for surface analysis of organic materials. Cluster ion beam reduces penetration depth but increases sputtering yield. Thus, the usage of cluster ions improves the quality of the SIMS depth profile for organic materials. Although, ToF-SIMS suffers from a low spatial resolution since the beam pulses are compressed to increase the mass resolution. [40]

The choice for the primary ion type depends on the investigated sample. A typical SIMS instrument usually has at least two different ion sources. [40] For larger organic molecules, large inert ions such as Ar^+, Xe^+ or Kr^+ are used. Typical ion cluster sources are C_{60}^+, Bi_{23}^+ or Bi_3^+. For electropositive specimens, oxygen ions are used, whereas for electronegative elements Cs^+, Ga^+ or In^+ are used. For example, a typical SIMS equipment for metal depth profiling could use Cs^+ and O_2^- sources. The Cs^+ ions will reduce the work function of the specimen surface causing emission of negative secondary ions. In contrast, the O_2^- primary ions form metal-oxygen bonds with surface atoms. During sputtering, such bonds will be broken and the emitted secondary ions will be positive. [38, 40]

The ion counts from the spectra can be converted to concentrations if the relative sensitivity factors (RSF) are known [43] :

$$RSF = D * \frac{I_M}{I_D}, \tag{3}$$

where D is the concentration of the element, I_M total ion count of the matrix, and I_D total ion count of the element. The RSF-values for different matrices and elements can be found from the literature.

The determination of elemental concentration in the specimen is a difficult task. The ionization probability depends on the nature of the analyzed element, the sample matrix, the chemical state of the surface, and the type of primary ions used. Therefore, SIMS is usually classified as a semiquantitative method. The elemental concentration is derived from comparative measurements between the sample and known standard samples whose composition closely resembles that of the specimen. [38]

A rough surface produces artifacts in the depth profile due to preferential sputtering (distorted secondary ion yield). The same effect can be seen in metallic materials since the sputtering yield depends on the surface orientation. Generally speaking, monocrystalline or amorphous single phase and smooth surfaces that tend to amorphize during sputtering produce the most accurate depth profiles. In contrast, polycrystalline metallic materials have the most inaccurate depth profiles. Moreover, defects such as dislocations and stacking faults might change the sputtering yield and the depth resolution decreases when the sputtering depth is increased. RMS roughness of tens of nanometers might be acceptable, but the desired roughness

is in the range of a few nanometers. The surface roughness can be polished, for example, by wet etching, chemical-mechanical planarization (CMP) or low energy ion bombardment. If polishing is not possible, the artifacts can be minimized using sample rotation during measurement or dual ion beam system that has two ion guns at different incident angles. [44, 45]

Several shortcomings prevent SIMS being used as routinely as XPS for chemical analysis. For example, there is no solid theoretical foundation for the cascade collision phenomenon. Additionally, the matrix has a very strong effect on the intensity and shape of the spectra (Matrix effect) and the data handling is challenging. [38]

4.6 Rutherford Backscattering Spectrometry

Rutherford backscattering spectrometry (RBS) is based on elastic recoil collisions. Alpha particles (He^{+} or He^{2+}) with an energy of 500 keV - 4 MeV penetrate the sample and backscatter due to the elastic recoils. Incident beam angle is close to the normal and only a small fraction of incident ions will backscatter. If the energy would be much lower than 500 keV, the probability for backscattering would decrease drastically. The backscattered ion energy depends on the depth and mass of the atom that caused the recoil. [46, 47] RBS has long been used by nuclear physicists for a quick examination of target purity and thickness but, nowadays RBS is employed in a number of different fields. The tool is illustrated in Figure 15. [47]

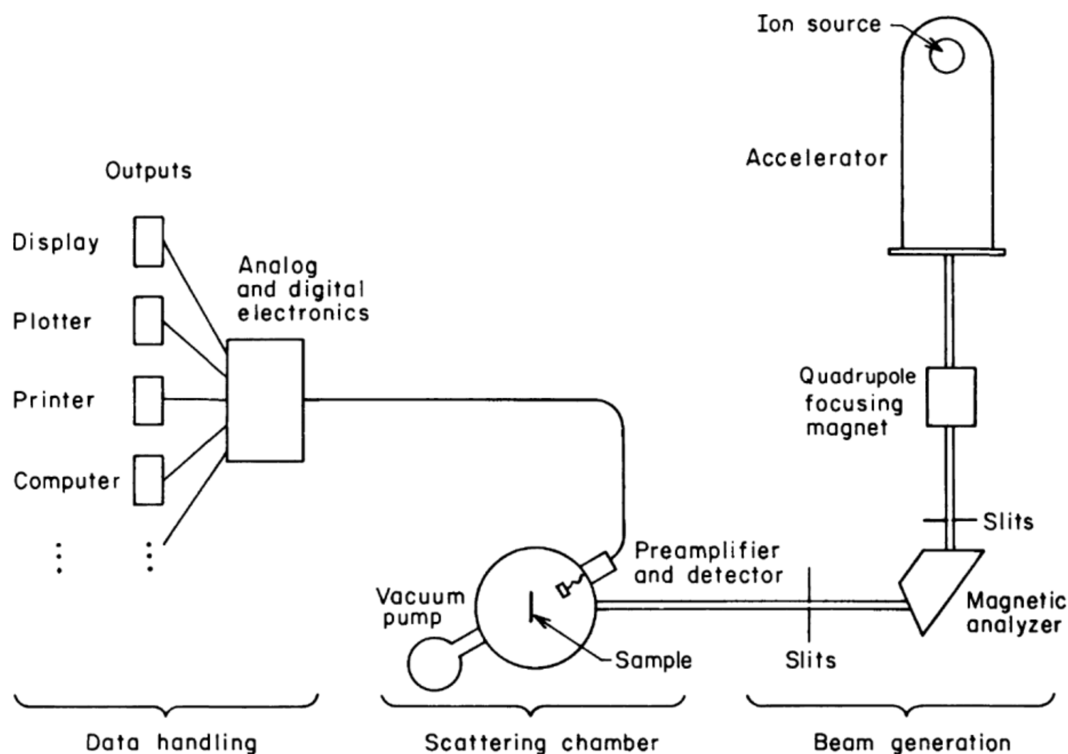

Figure 15: The incident ion beam energy is carefully measured since the incident energy is used as reference for data analysis. The scattering chamber is under moderate vacuum and the chamber contains multiple detectors in different angles. [48]

A common choice for ion source is a Van de Graff generator integrated with a particle accelerator. Silicon detectors at various angles count the number of scattered particles and their energies. The interpreted information contains data of composition, distribution of elements, and sample thickness. Typically, no heavier than He^{2+} ions are used since heavier ions would cause more surface damage and decrease the energy resolution of the silicon detectors. Usually, it is a good practice to acquire data at least from three different scattering angles. [47] The probability of scattering depends on the scattering cross-section which is defined as an amount of particles that will scatter into the differential solid angle $d\Omega$. In other words, the scattered particle can scatter to different directions from the scattering center and there is a finite probability of scattering from a target nucleus. For RBS, the scattering cross-section is fairly small since the probability of backscattering is low. [49] The scattering in RBS is demonstrated in Figure 16.

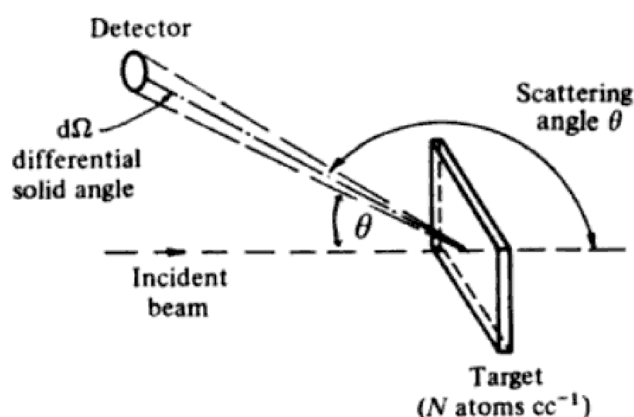

Figure 16: The incident ion beam is normal to the sample and there are different probabilities for scattering to occur in different directions. The backscattering probability is low for RBS and the probability can be modeled as a differential cross-section which depends on the scattering angle Θ, differential solid angle $d\Omega$, and impact parameter b that is defined as a distance between the scattering center and scattering cross-section. [47]

Elements lighter than the matrix are hard to detect using RBS. Furthermore, RBS is nearly blind to carbon, nitrogen and oxygen due to the low backscattering probability, and the incident ion energy is considerably low when then incident ion is backscattered from a light element. [50] Additionally, lighter element peaks in a spectrum tend to shrink if the sample contains even thin layers of heavier elements as seen in Figure 17.

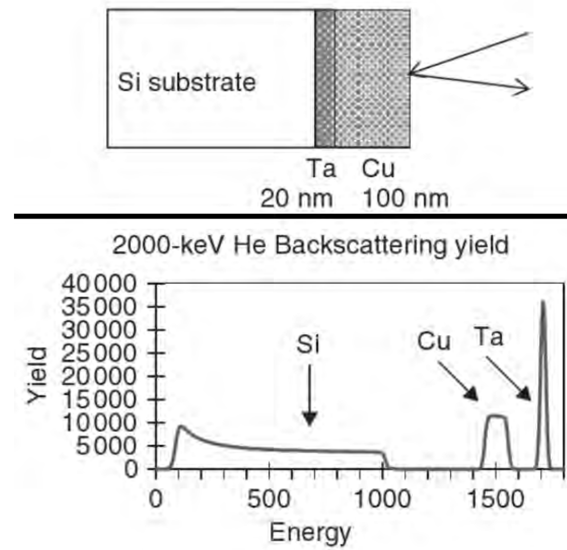

Figure 17: RBS suffers from masking by heavy elements. In this case, the Si substrate is covered by thin layers of Ta and Cu that are heavier elements than Si. The yield for the Si is not accurate. Likewise, if the sample matrix consists of heavy elements, the impurity profile for lighter elements will be inaccurate. [46]

A typical resolution limit is 0.5 at.% for lighter elements and ∼ppm for heavy elements. [46] The major disadvantage of RBS is that two elements of similar mass cannot be distinguished. [48] That disadvantage is highlighted for heavier atoms since the incident ions transfer less momentum to heavier atoms. The atomic mass resolution in relation to the atomic weight is plotted in Figure 18. [49]

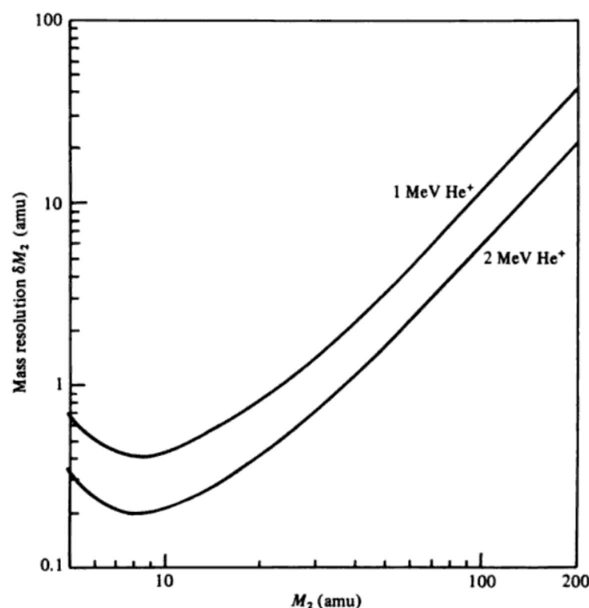

Figure 18: The mass resolution is low for heavy elements. RBS cannot differentiate heavy elements if their mass is not atleast 10 amu apart. [47]

The mass resolution for heavy atoms can be increased by using increased beam energy or using heavier incident beam ions. [47] Likewise, the resolution limit for lighter elements can be increased by increasing the incident ion energy and scattering angle. If the ion energy and scattering angle are high enough, the scattering cross-section becomes non-Rutherford and the traditional equations will not apply. Additionally, current equipment can use forward scattered particles to increase the resolution. [49]

RBS can be used for depth profiling with a resolution of 5-50 nm. The depth profiling does not destroy the sample and the achievable measurement depth is usually between 1-20 μm. [48, 49] Most of the scattering occurs at a deeper level below the surface where the energy of the projectiles is decreased. The penetrated ions slow down in the sample and the beam energy is spread due to the transfer of energy to electrons or nuclei. This phenomenon is called straggling. Therefore, near the surface the resolution is highest and the resolution decreases in the deeper regions. Practically, the straggling effect depends on the stopping power of different elements. One example of straggling is shown in Figure 17. On the other hand, the film thickness can be calculated by using energy difference of scattered ions from different depths. Although, the film thickness calculations require well-defined energies of particles regarding the depth. [47]

RBS requires a low surface roughness, similar to SIMS. Very often, a spectrum that shows diffusion or mixing of elements is actually a result of the surface roughness. Therefore, quantitative RBS analysis is usually limited to laterally homogeneous and smooth films. [44, 51] Three-axis sample holder can be used to find low index crystallographic directions by monitoring RBS yield when tilting the sample [49]. Furthermore, the ion channelling effect can be used to locate lattice positions of impurity atoms in a single crystal and usage the major crystallographic directions minimizes the background noise. [47]

4.7 Elastic Recoil Detection Analysis

In contrast to RBS, Elastic Recoil Detection Analysis (ERDA) is based on elastic recoil collisions. Furthermore, RBS detects only backscattered primary ions, whereas ERDA can detect recoiled target atoms. [50] The main advantage of ERDA is its almost equal sensitivity for heavy and light elements. ERDA was first time used in 1976 by L'Ecuyer. [52] It could be said that RBS and ERDA are complementary techniques since RBS is more sensitive for elements that have a larger mass than that of the matrix, whereas ERDA is more sensitive for elements that have a lower mass than the matrix. [50]

ERDA uses heavy primary ions from C to Au with an energy of several hundred MeVs that enables investigation of light elements. The most used primary ions are Cl, Cu, Br, I, and Au. [53] Furthermore, an absorber foil is usually placed in front of silicon detectors to protect the detector and stop the heaviest particles. Therefore, lighter ions will pass the foil and can be detected without masking by the heavy particles. In the optimal situation, the primary ions have approximately same mass than the atoms in the matrix. [50, 53] As a tool, ERDA and RBS are very similar. Essentially, RBS can be used as ERDA if absorber foil is used and the incident ions can be changed to heavier ones. [50] Figure 19 shows a solution from University of Jyväskylä that uses same ion accelerator for RBS, ERDA, particle-induced X-ray emission (PIXE), and ion beam lithography (IBL).

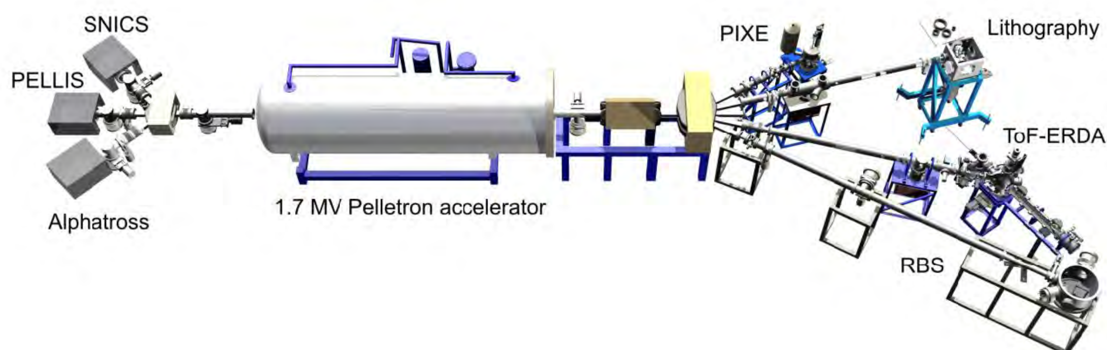

Figure 19: The ion sources are different but the same ion accelerator can be used for RBS, ERDA, PIXE, and IBL. [52]

ERDA is a real quantitative method and interpreting of the spectrum does not require heavy computations or simulations. In the spectrum, the peak area represents the density of the analysed atoms in the film. The peak height indicates the concentration of that particular element. If all elements in the sample do not contribute to the spectrum, the peak can be used to calculate relative concentrations. The accurate sampling depth is less than for RBS but the resolution is at least 0.1 at.%. ERDA is suitable for thin-film analysis, especially if time-of-flight (ToF) detector is used. [50]

Analogous to RBS, the ions can be generated by a Van de Graff generator. Typical accelerators are cyclotrons or tandem accelerators. Similar silicon detectors than in

RBS can be used, but the resolution is not good for heavy ions and the silicon gets easily damaged. Furthermore, since the foil is usually used, electrons lose energy due to the straggling effect in the foil. Therefore, silicon detectors are not most suitable for accurate depth profiling. ERDA systems for depth profiling use either gas ionization detectors, ToF detectors or magnetic spectrometers. In the case of gas ionization detectors, the recoil travels through a window to a detector gas chamber. The energy resolution is better than with the silicon detectors and the lifetime does not degrade by heavy ions. The drawbacks are lower ionization yield and some of the particles are lost when they try to enter the detector through a small window. Therefore, the gas ionization is usually used with heavy incident ions with high energies, such as Au with energy of 300 MeV. [50, 53]

ToF detectors have been used since 1983. [52] ToF does not present similar problems than the silicon detectors. However, the throughput is not as good since the ion detection is performed in a serial. Furthermore, the efficiency is lower for light elements and the scattering angle is critical since the detectors are far away from the sample. The efficiency for lighter elements can be increased by lowering the incident ion energy as seen in Figure 20. ToF-ERDA is based on the fact that heavier ions have a longer flight time than the lighter ions. [50] The longer the time of flight (distance between timing detectors), the better the energy resolution will be. The detectors are shown in Figure 21. Typically, ToF-ERDA uses Cl, Cu, or Br primary ions with less than 100 MeV energy. [53]

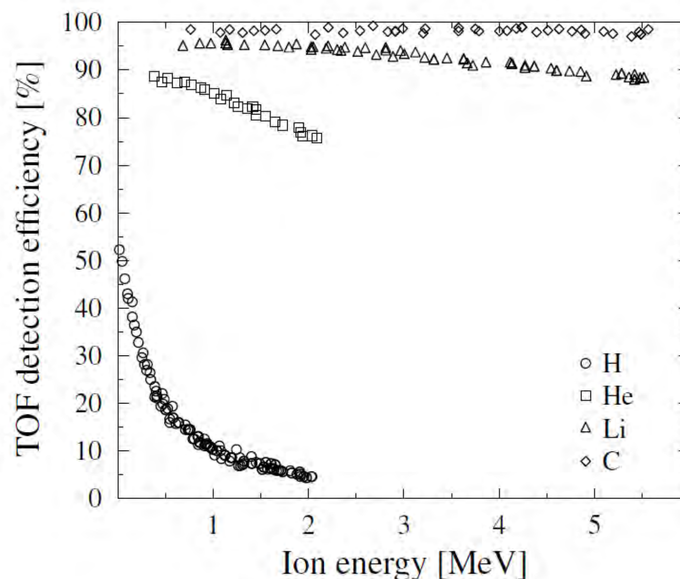

Figure 20: The efficiency of the ToF-ERDA for light elements depends on the ion energy. Usually, ERDA uses ion energies of tens or hundreds MeVs, but measuring light elements by ToF-ERDA requires lowering incident ion energy significantly. [53]

A typical ToF-system uses two ToF timing detectors and a conventional silicon detector. The first timing detector is placed at a fixed scattering angle near the sample. The second timing detector is placed at a variable angle at a longer distance.

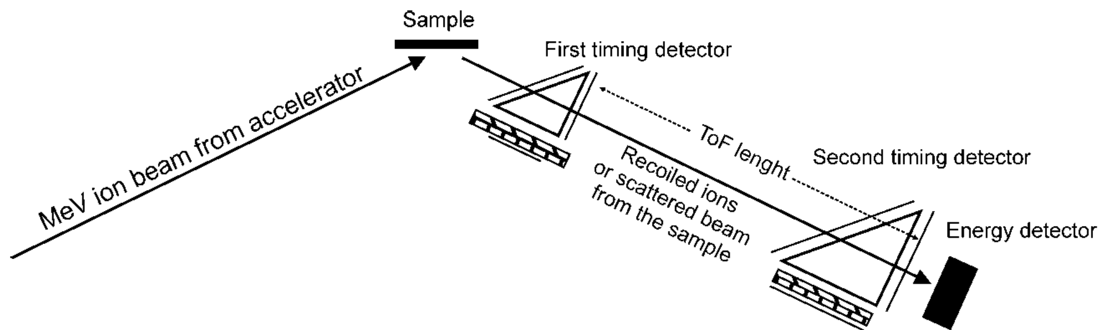

Figure 21: A typical ToF-ERDA uses two timing detectors that acquire the timing signal using carbon foils. The resolution depends on the stopping power of the coils and the distance between timing detectors. [52]

The acquired plot is not a spectrum, but a scatterplot as seen in Figure 22. [54]

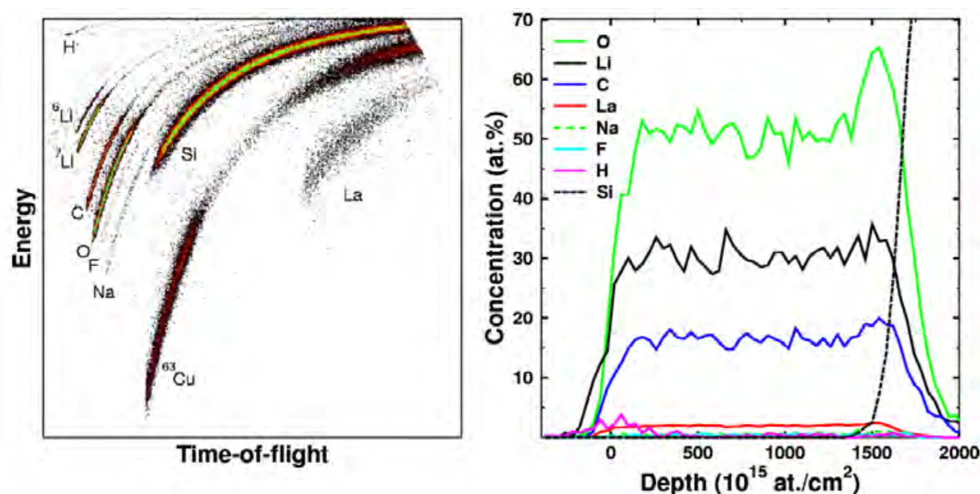

Figure 22: The ToF-ERDA produces a scatterplot. There is a visible correlation between atomic mass and in the position on the X-Y axis. The color collaborates to the concentration. The scatterplot is converted to a depth profile using computational methods. [52]

The timing detectors use a carbon foil to pick-up the timing signal and the detection efficiency for light elements is proportional to the stopping force and ion scattering in the carbon foils. The depth resolution is mainly limited by the timing resolution of the timing detectors and kinematic spreading in the sample. [52] ToF-ERDA sensitivity can be ∼10 ppm depending on the measurement conditions. The depth profiling is possible up to several microns. The depth resolution is ∼10 nm near the surface and decreases when the depth is increased. Unlike with the silicon detectors, the acquired scatterplot is evaluated using computational methods to extract the elemental information. [54]

The magnetic spectrometers use a magnetic field to measure charged recoiled particles that have different trajectory depending on their mass and velocity. All

recoils that have similar trajectory has same charge/momentum ratio and the recoils are identified by the energy in the detection plane. The high energy resolution is obtained by determining the particle location in the detection plane. Therefore, the depth resolution is drastically improved compared to the silicon detectors. [53] This type of detector allows usage of a very low ion dose for accurate measurements and enables a monolayer resolution at the surface. The depth resolution can be increased further using coincident elastic recoil detection (CERD) that requires very thin sample since both scattered and recoiled particles are measured. [50]

The collision cascade is a fundamental requirement for SIMS, whereas for ERDA, multiple scatterings will distort the elemental spectrum. Monte Carlo -simulations can be used to verify the amount of multiple scatterings to obtain reliable data. [52] Analogous to RBS, the sample should be laterally homogeneous and have a smooth surface. The beam size and the incident angle are critical for ERDA since all detected recoils should be ejected at the same direction and pass over the same path for accurate analysis. [50] Unlike in RBS, the scattering cross-section is large since the probability for forward scattering is high and the probability does not change with the mass of the element.

Indeed, ERDA is a unique method to get an accurate depth profile without destroying the sample. When combined to the ToF-detector, the tool is very accurate for thin-film analysis, such as atomic layer deposited (ALD) thin-films with a resolution of 0.5 at.%. [53] For the best accuracy, ERDA and RBS should be used as complementary techniques. ERDA is especially popular in polymer sciences since it can study the hydrogen content accurately. It should be remembered that the high energy beam might decompose or sputter the sample that lead to inaccurate impurity analysis.

4.8 Comparison

The reviewed techniques were distinguished into two groups based on the probing species as shown in Table 2. From the reviewed techniques, the two main categories were: a) probing by electrons b) probing by X-rays or ions. However the applications of each tool are discussed in Section 6 and this section focuses on comparative discussion.

XPS is probably the most used surface analysis tool. AES is almost similar to XPS, however, XPS results are easier to interpret. Furthermore, both techniques are limited to the surface area and the maximum sputtering depth is usually in the range of 1 μm. In other words, they are most commonly used for surface characterization similar to ERDA and RBS. In contrast, SIMS can be used to characterize films up to 20 μm. However, SIMS requires standards for quantitative results. The standardization can be acquired by other tools such as RBS or ERDA [50]. Currently, there are tools available that combine both AES and XPS. The combination enables more accurate characterization of complex materials since both techniques have different efficiency ranges as seen in Figure 8. However, the surface charging is a major problem for AES. On the other hand, AES has a superior lateral resolution to XPS. Nevertheless, the popularity of the tool is not a guarantee of superiority.

Table 2: Tabulated properties of the reviewed techniques based on Section 4. It should be taken into account that the values such as detection limit depends on the atomic mass of the element. For example, SEM has 1 at.% detection limit for heavier elements.

	AES	EELS	SEM-EDX	(S)TEM-EDX
Probe Species	Electrons	Electrons	Electrons	Electrons
Detected Species	Electrons	Electrons	X-rays	X-rays
Depth resolution	1-10 nm	Sample thickness	400-1000 nm	Sample thickness
Lateral Resolution	10-200 nm	1 nm	1 μm	<50 nm
Elements Detected	Z >2	All	Z >3	Z >3
Detection Limit	<1 at.%	<1 at.%	<10 at.%	<1 at.%
Chemical info	Limited	Yes	No	No
Quantification	Yes	Yes	Limited	Limited
Sputtering rate	~400 nm / hour	-	-	-
Depth profile	Down to 1 μm	No	No	No
	XPS	**SIMS**	**ERDA**	**RBS**
Probe Species	X-rays	Ions	Ions	He ions
Detected Species	Electrons	Ions	Ions and recoiled atoms	He ions
Depth resolution	1-10 nm	1-50 nm	>2 nm	>2 nm
Lateral Resolution	10 - 100 μm	10 nm - 100 μm	>10 μm	>500 μm
Elements Detected	Z >2	All	All	Z >4
Detection Limit	<1 at.%	<100 ppm	<0.1 at.%	<1 at.%
Chemical info	Yes	Only with ToF-detector	Limited	Limited
Quantification	Yes	Only with standards	Yes	Yes
Sputtering rate	~400nm / hour	~3 μm / hr	-	-
Depth profile	Down to 1 μm	Down to 10 μm	Down to 5 μm	Down to 20 μm

For example, based on Section 4.7, ToF-ERDA is superior to XPS for thin film characterization, especially if the film contains light elements, such as hydrogen.

The major advantage of RBS is its ability to acquire quantitative results without standards. Furthermore, it is a non-destructive technique and the depth resolution is relatively good. However, the lateral resolution is not that great. ERDA is almost analogous to RBS, although, attributes of ERDA are superior to RBS in almost every aspect. However, AES and XPS has a superior depth resolution compared to ERDA/RBS if the sputtering rates for each material are well known. Most of the reviewed techniques do not require special preparation other than deposition of a conductive surface layer in the case of surface charging. However, (S)TEM-based techniques require lamella preparation that might be very demanding depending on the sample. TEM-EDX lateral resolution depends on the sample thickness, for example, the spatial resolution is 20 nm for a 100 nm thick sample that is probed with a 100 keV beam. For the same sample thickness and beam energy, EELS offers 3 nm spatial resolution and the spectrum acquired by EELS will not contain peak overlapping. However, EELS cannot be used for thick samples due to the multiple electron scatterings.

One important aspect is the demand for processing the acquired data. For example, both XPS and AES require peak fitting that might lead to inaccurate results depending on the software and experience of the user. However, the most demanding tool is SIMS since the sputtering yield spectrum provides a negligible amount of data about the relative composition if the RSF values are not used. Altogether, most of the reviewed tools provide reliable results based on the acquired spectra without requirements of experience on the tool.

From the reviewed techniques, SEM-EDX is presumably the worst choice for quantitative analysis. However, it is usually used due to its wide availability and user-friendliness. On the other hand, the ability for EDX quantification can be increased if the tool is integrated to (S)TEM.

The best elemental analysis tool cannot be chosen if the requirements are not known. If the lateral resolution is the main requirement, EELS, (S)TEM-EDX or SIMS should be chosen. In contrast, SEM-EDX, XPS, and RBS offer the lowest lateral resolution. Likewise, if depth resolution is the main criteria, AES, XPS, SIMS, ERDA or RBS would be the main choice. For depth profiling, the most suitable techniques are SIMS, RBS and ERDA. Altogether, there do not exist a tool that fullfills all the demands. This thesis recommends using at least two different techniques for accurate quantitative analysis, for example, ERDA/RBS together with XPS/AES. The choices are discussed further based on the applications discussed in Section 6.

5 Structural Characterization

The word "structure" refers here to microstructure, IMCs, grains, defects, etc. In the best-case scenario, all of these listed structural properties could be characterized using a single tool. The other expectation is that the tool should be widely available. This section reviews some of the tools that might be able to measure more than one structural feature from a sample. However, tools such as SEM and optical microscope are not reviewed since they currently are well-known and commonplace. The first subsection introduces how the ASTM grain size method and linear intercept method can be applied to calculate an average grain size.

5.1 Grain Size Calculations

One widely used method to specify average grain size is American Society for Testing and Materials (ASTM) standard test method E112 which specifies the grain size as a comparative number n in equation:

$$N = 2^{n-1}, \tag{4}$$

where N is the number of grains per square inch when the magnification is 100x and n is the comparative grain size number [55]. According to the standard, twinned grains are not included as separate grains in the grain size calculations. If different magnification is used, the N can be calculated from:

$$N = Amount\ of\ Grains\ in\ True\ Area\ * \frac{0.0645mm^2}{True\ Area}, \tag{5}$$

where 0.0645 mm^2 is the true area of square inch area at 100x magnification. [55] If the N is known, Equation 4 can be solved with respect to the grain size number n:

$$n = 1 + \frac{log(N)}{log(2)}. \tag{6}$$

Mean area of the grain section $\overline{A}$ is:

$$\overline{A} = \frac{1}{N_A}, \tag{7}$$

where N_A is the number of grain sections per unit test area. The mean grain diameter $\overline{d}$ is the square root of $\overline{A}$. There exists the following relationship between the N_A and N:

$$N_A = N * (\frac{100}{25.4})^2, \tag{8}$$

where N is the number of grains per square inch at 100x magnification. Equations 4, 7 and 8 can be used to construct Equation 9 for average grain diameter $\overline{d}$:

$$\overline{d} = \frac{\sqrt{\frac{25.4^2}{2^{n-1}}}}{100}, \tag{9}$$

where $\overline{d}$ is the average grain diameter in millimetres and n is the ASTM grain size number. The calculated average grain diameters using equation 9 can be seen in Table 3.

Table 3: The table shows calculated average grain sizes for different ASTM grain size numbers. The relative sizes are for easier reference in the text.

ASTM size no.	Average Grain Size (μm)	Relative Size
-1	508	Very Coarse
0	359	
1	254	Coarse
2	180	
3	127	
4	90	Medium
5	64	
6	45	
7	32	
8	22	Fine
9	16	
10	11	
11	8	Very Fine
12	6	
13	4	
14	3	Ultrafine
15	2	
16	1	
17	0.99	Submicron
18	0.70	
19	0.50	
20	0.35	

These results can be confirmed using linear intercept method (LIM) that requires drawing lines in a micrograph. The number of grain-boundary intercepts along the lines are counted. The mean linear intercept $\bar{l}$ is then given as:

$$\bar{l} = \frac{L}{N}, \tag{10}$$

where L is the length of the line and N number of intercepts. The $\bar{l}$ does not provide the grain size however it can be converted to spatial diameter $\overline{D}$ of sphere by:

$$\overline{D} = 1.5 * \bar{l}. \tag{11}$$

The grain size growth of copper can be approximated:

$$D - D_0 = (kt)^{1/n}, \tag{12}$$

where D_0 is the initial grain size, D is the grain size at time t, n is the grain growth exponent, and k is a constant that is defined by:

$$k = k_0 * e^{\frac{-E_a}{RT}}, \tag{13}$$

where k_0 is a constant, E_a activation energy, R gas constant and T the annealing temperature. Various different activation energies have been calculated for copper grain growth ranging from 0.62 eV to 1.036 eV. [56, 57] For ideal grain growth, the grain growth exponent would be 2, however, it has been reported that it ranges from 3 to 4 for electroplated copper. [56, 57] Since there is no consensus about activation energy, the grain growth can be approximated using equation 12 if the k is known. Based on results by E. M. Zelinski et al. [58], the constant k was found to be 380 nm/hour when annealed at 150 °C and 540 nm/hour when annealed at 200 °C. Those values were used to approximate the grain growth. Table 4 approximates the copper grain growth at 150 °C using equation 12, n-value 3.2 and 350 nm initial grain size.

Table 4: Copper grain growth at 150 °C

Time (hours)	Growth (nm)	Grain size (nm)
0	0	350
1	236	586
2	293	643
4	364	714
8	452	802
12	513	863
16	561	911
20	602	952
24	637	987
32	697	1047
40	747	1097
48	791	1141
72	898	1248
144	1115	1465
1000	2043	2393

The calculations were done for 200 °C in similar fashion and the results are plotted in Figure 23.

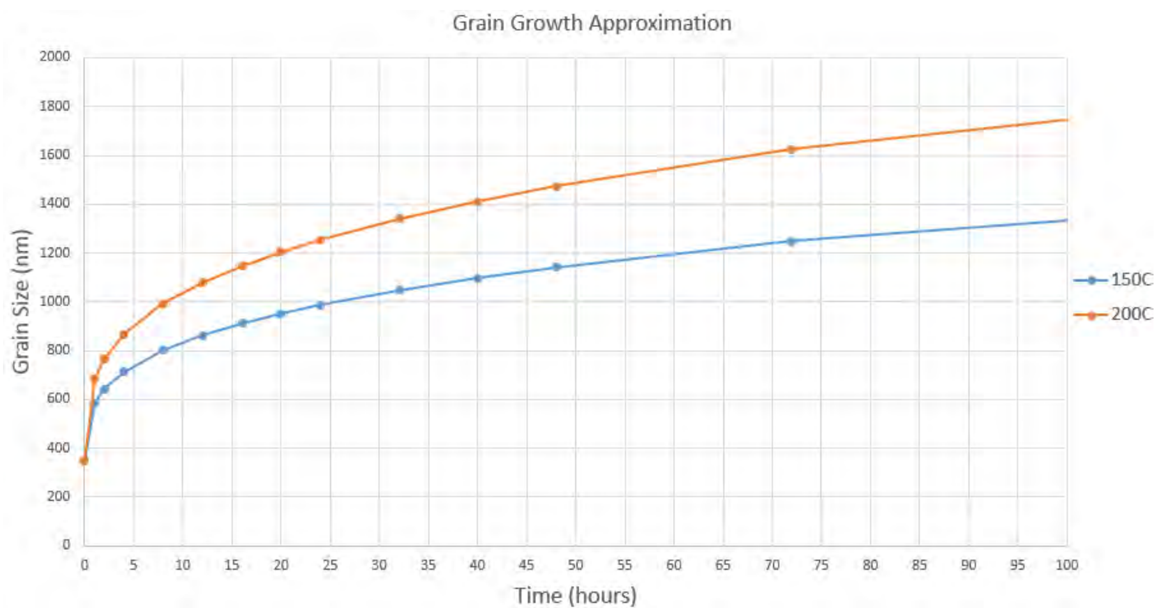

Figure 23: Equation 12 is used to approximate the copper grain growth at 150 °C and 200 °C. The plot can be used as a reference when choosing annealing times for a grain size study.

5.2 Transmission Electron Microscopy

Transmission electron microscope was developed in 1931 by Max Knoll and Ernst Ruska. Scanning transmission electron microscope (STEM) was developed in 1938 by Manfred von Ardenne. The goal was to achieve a resolution exceeding that of the optical microscope. The objective has been well reached since the first TEM instruments had a 40 nm resolution limit that has been increased to 0.05 nm with current equipment. The STEM was not a popular tool until the innovations by Albert Crewe. Between the 1960s and 1970s, Crewe published several articles regarding possibilities of the STEM overcoming the resolution limit of the conventional TEM and new imaging modes, such as annular dark field (ADF) imaging [32] .

The main components of TEM are an electron source, lenses, apertures, and a projection chamber. A typical TEM instrument and the different lenses are illustrated in Figure 24. The electron source is either thermoionic, field emission gun or cold field emission gun and the different types of electron sources are suitable for different applications. Thermionic tungsten (W) sources are the least expensive but offer lower brightness and lifetime. On the other hand, the total beam current is high. Replacing the W by LaB_6 increases the cost but provides more brightness and longer lifetime. Field emission guns are the most expensive, but they offer the highest analytical performance. Cold field emission offers high brightness but varying beam current and it requires frequent flashing. Thermally assisted field emission provides stable current and latest generation of these type of emitters attain brightness level close to the cold field emission. [59]

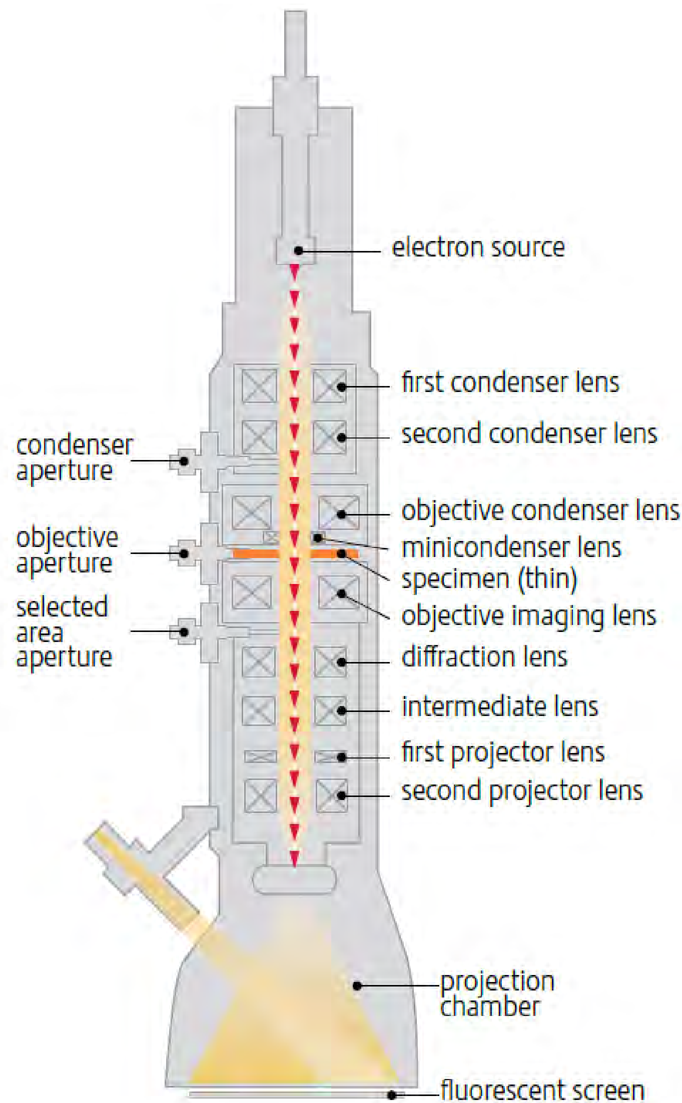

Figure 24: A TEM instrument uses multiple condenser lenses and apertures. The condenser lens system is above the sample and the objective lenses are below the sample. [59]

Different lenses have different functions. The condenser lens system focuses the electron beam and controls the beam size. The objective lens produces the image and the remaining lenses magnify the produced image. If the sample is crystalline, a diffraction pattern can be formed at the back focal plane below the objective lens. [59] The fundamental difference between STEM and TEM is the location of the specimen in the pathway of the electron beam. In TEM, the specimen is located between the condenser lens system and the objective lens. In STEM, the specimen is located below the objective lens. An example of STEM instrument is shown in Figure 25. [32]

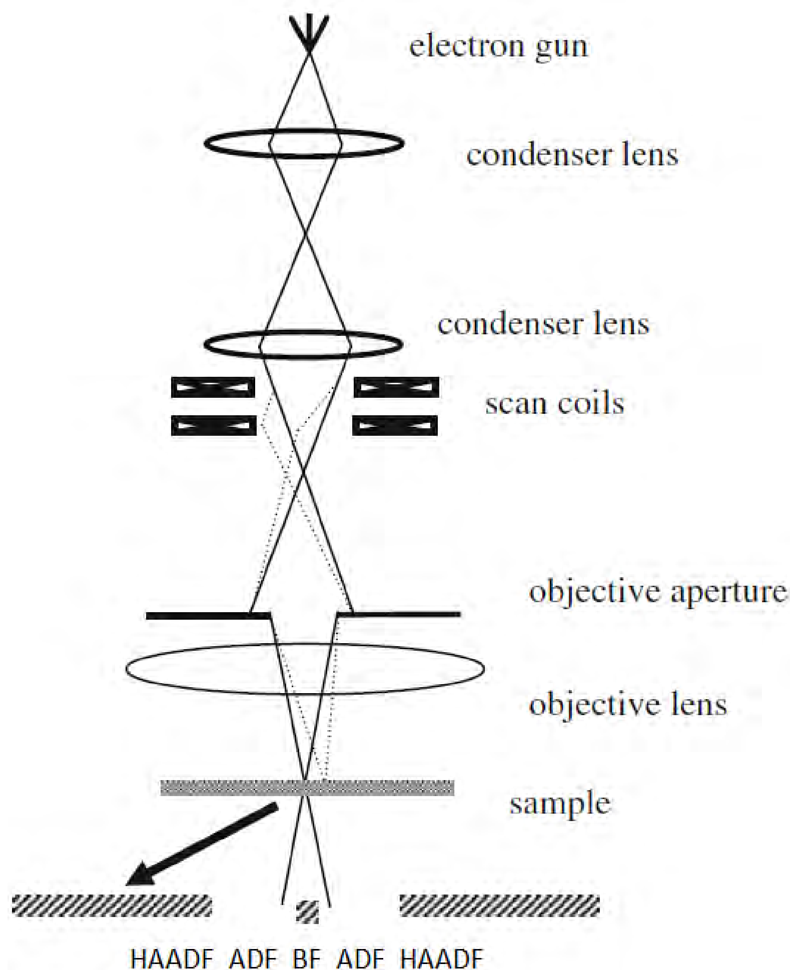

Figure 25: If STEM is compared to TEM, the optics are on reserved order. The objective lens is above the sample and the image is constructed using detectors, not lenses. [32]

Spherical aberration causes blurring of the image and it is the primary reason for resolution limitations of conventional TEM. The aberrations can be reduced by better lens design, thinner samples and by keeping the acceleration voltage as stable as possible. From the end of the 1990s, commercial TEMs have been using aberration-corrections that change the resolution limitation factor from spherical aberration to chromatic aberration. [32] The chromatic aberration can be reduced by minimizing the sample thickness and reducing the energy spread of the electron beam. [59] However, the usage of spherical and aberration corrections is limited by the high cost.

It could be described that the STEM combines principles used by both TEM and SEM. In addition to the reversed order of the optics, the STEM addresses each pixel in series, whereas TEM illuminates the whole area of interest and the electrons are collected in parallel as shown in Figure 26. The resolution of a STEM image is not degenerated by chromatic aberration since the transmitted electrons do not need to be refocused at the objective lens. The major drawback of STEM

is worse signal-to-noise ratio which is three times worse than that of TEM. [32, 59] There exists a wide range of possible detectors available for STEM, but the common ones are a bright field (BF) and an annular dark-field (ADF) detectors. An electron energy loss (EEL) and energy-dispersive X-ray (EDX) detectors are used for chemical analysis.

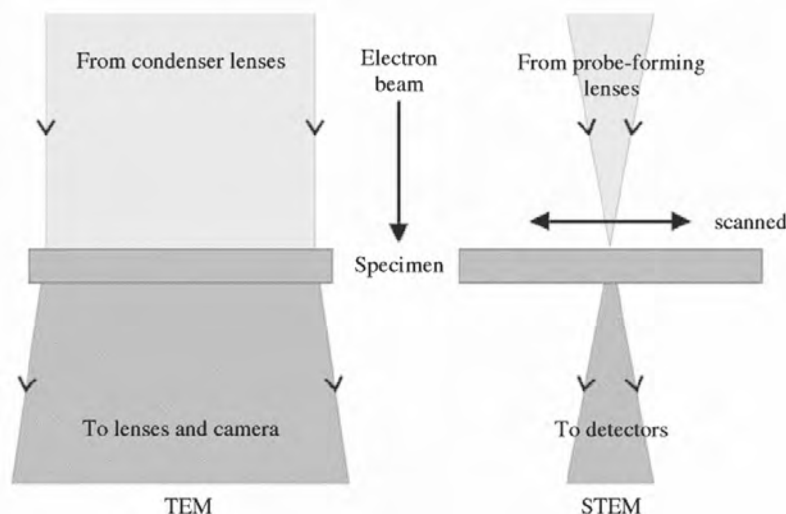

Figure 26: TEM scans the whole area of interest, whereas STEM addresses each pixel in series. [60]

The principles of the imaging modes are similar for STEM and TEM since the optics systems are analogous, only rotated another way around respectively. Accordingly, similar imaging modes are possible for both tools, such as bright field (BF), dark field (DF), Energy-dispersive X-ray (EDX), electron energy loss (EEL), and selected area diffraction (SAED) patterns. In addition to these, the STEM offers high-angle annular dark field imaging (HAADF) which is not possible for TEM. Depending on the tool, the imaging modes are differently optimised and some of the modes work better with TEM while others with STEM. [60] For TEM, the BF mode allows mostly the direct electron beam to pass and the image is produced by its interaction with the sample. The BF mode is used to acquire phase and amplitude contrast images that consist of mass-thickness contrast and diffraction contrast. Mass-thickness contrast is caused by higher incoherent elastic scattering in the areas that have higher Z and/or thickness appearing as a darker contrast in the images. [61] Diffraction contrast is caused by Bragg scattering. Thus, more crystalline areas appear as darker contrast and less crystalline areas as brighter contrast. Diffraction contrast is fundamentally a special form of amplitude contrast where the scattering occurs at Bragg angles. The mass-thickness contrast is usually weaker and overshadowed by the stronger effects of the electron diffraction. Therefore, it is easier to get mass-contrast for amorphous samples than for crystalline samples. In TEM, the objective lens aperture can be used to select only one Bragg scattered beam, whereas a STEM detector might collect several Bragg beams reducing the contrast. Therefore, TEM is usually used for diffraction contrast images. [61] Generally speaking, the whole BF

imaging mode in STEM is not adequate since the relatively small detector cannot collect all electrons in the detector plane. [32]

The DF mode is reversal to the BF mode. In TEM, the direct beam is blocked and only some of the diffracted beams are detected. The corresponding mode for STEM is the ADF mode that uses a detector to collect electrons that have diffracted 10-50 mrad off the axis. [32] Similar to the BF mode, the diffraction contrast is dominant, but the mass-thickness contrast might be visible also. STEM is more efficient for dark field imaging than TEM since the detector can collect all scattered electrons. Furthermore, TEM DF mode is often called as "low-resolution dark-field imaging". [61]

The speciality of the STEM is high-angle annular dark-field imaging (HAADF). It is essentially similar to ADF imaging, but the detectors collect electrons that are scattered over 50 mrad off the axis depending on the cameral length of the detector. High-angle scattered electrons are mostly caused by Rutherford scattering and they are usually insensitive to crystallinity or orientation of the sample. Furthermore, the scattered electrons are strongly dependant on the atomic number of the probed area. That is especially advantageous for a mass-thickness contrast of crystalline samples since the diffraction contrast is dominating in the BF and DF modes. The resolution of HAADF depends only on the uniformity of the specimen thickness and the beam size. An atomic level resolution is possible if the specimen is uniform and the beam diameter is less than one atom dimension. [32, 60]

Phase contrast images are acquired when the phase of the electron wave is altered by a very thin specimen. HRTEM refers to instruments that are designed and mostly used for the phase contrast imaging. If the sample is thin enough, the amplitude contrast does not take place and the contrast arises mostly from phase alteration caused by the potential of single atoms. With conventional TEM, the phase contrast is triggered by defocusing the objective lens and using a large objective aperture so that both transmitted and scattered electrons are used to form an image. The phase contrast imaging is used for very high resolution images or acquiring interference patterns (Fresnel edge fringes). Phase contrast imaging is challenging since the sample thickness, orientation, scattering factor, focus and astigmatism have an effect on the phase alteration. The advances in spherical and chromatic aberration corrections have enabled more reliable phase contrast imaging. [62, 63]

Selected area diffraction (SAED) mode uses a selected area aperture that allows only a small fraction of the electron beam pass though a hole in the aperture to the selected area. Each acquired spot corresponds to a satisfied diffraction condition with chosen zone axis. The minimum area is fairly large (hundreds of nms) and the acquired lattice parameters have an accuracy of 5%.

Since the electrons are easily stopped or deflected by matter, the specimen should be thin enough for electron transmission. The typical upper limit, depending on the imaging mode, sample type, and acceleration voltage, is few hundred nanometers. A thinner specimen is almost always better. [59] In most cases, the specimen is prepared from a larger sample. The sample preparation should not change the important features of the specimen. The ideal specimen must be thin enough that it can be treated as a weak phase object for HRTEM and electron beam spread should be

negligible. [64] On the other hand, the sample should be thick enough to support itself and there should be a sufficient signal from electron scatterings. Furthermore, the surface contaminations or defects should not dominate the acquired signal. The bulk samples can be thinned with several different techniques that are based on wet etching, ion bombardment, physical cracking or conventional polishing.

Twin-jet electrolytic thinning is en electrochemical technique for thin conductive samples. The technique produces a hole that has electron-transparent edges. It is typically used for bulk single-phase metals or semiconductors since preferential etching causes challenges for inhomogeneous and multiphase materials. Twin-jet electrolytic thinning is the only technique that does not produce preparation artifacts. In contrast to electrolytic thinning, twin-jet chemical thinning can be used even if the sample is not conductive or it consists of multiple phases. The sample can be slightly thicker, but the produced hole will be basin-shaped. Since the sample can be thicker, it can be easier to handle after the process. The major disadvantage is the surface contaminations caused by the chemical etching. [64]

It is not compulsory to use twin-jet etching. Instead, the sample can be etched in a full-bath. Similar to the twin-jet thinning, the full-bath thinning can be electrolytic or only chemical. This method does not produce a hole, but an edge that is electron-transparent. The area of interest is limited by isolating or masking film. The sample can be a lot thicker than for twin-jet thinning. The disadvantages are similar to the twin-jet thinning. [64]

Wedge-cleavage is the quickest method to obtain a thin slice from a monocrystalline sample. The edge of the sample is cleaved by fracturing along an atomic plane. The far side of the edge will be transparent to electrons. The sample is mounted on a holder that allows controlling the orientation during imaging. However, the ascending thickness does not allow using EDX or EELS. The disadvantages of the method are the following: it is suitable only for monocrystalline materials and sloppy cleaving might cause dislocations or dislocation clusters. [64]

Ultramicrotomy is a technique to produce slices by making a micro-crack. The fracture is induced by the blade of a knife. Ultramicrotomy requires a very small sample that has suitable hardness and plasticity to produce a fracture that does not break the whole sample. The micro-crack causes many types of artifacts and the operator is required to have a long training. In the other hand, the technique is fast for an experienced operator. The sample types can be expanded to polymers if the ultramicrotomy is done at cryogenic temperatures. [64]

In tripod polishing, the sample is attached to a tripod and it is polished by abrasive grinding on a slight angle producing an electron-transparent edge. The polishing is executed on a series of abrasives with grain sizes from 30 um to 0.05 um. The sample is polished from both sides in a similar way. For a large number of materials, the final electron-transparency is achieved by ion-milling since the abrasively polished slice is very sensitive and brittle. The major advantage for tripod polishing is the reduced time for ion milling. [64]

Additionally, the sample can be thinned using FIB which is reviewed in section 5.3. The other ion-based technique is ion milling that is very similar to FIB but uses a large-area ion beam with a maximum incident beam energy of a few keV. In

contrast to FIB, ion milling uses Ar^+ ions and the beam angle can be varied from 0 ° to 90 °. Since the beam is weak, ion milling is used to remove a maximum of 15 μm from the surface. Therefore, ion milling is usually used as a surface finish technique to remove defects caused by FIB or abrasive polishing. Furthermore, ion milling causes similar defects than FIB, such as redeposition, implantation, amorphization, and chemical diffusion. [64] However, if the ion beam energy is gradually decreased, the surface damage can be limited to the outermost 1 nm layer. [39]

5.3 Focused Ion Beam

The development of FIB began in 1974. Between the 1980s and 1990s, FIB was primarily used for device fabrication, device repairing, and mask prototyping. The processing time is usually too long to create structures on the scale of the whole wafer. At the end of the 1990s, FIB became a popular tool for TEM sample preparation. [65] FIB can remove material, deposit material using precursor gas or implant ions in the specimen. Moreover, these functions are carried out locally. However, the ion beam also causes lattice defects, amorphization, and implantation of ions. [66] Many of the current FIBs are called dual beam systems since they include an SEM-microscope. FIB instruments can be incorporated in other systems also, such as in TEM or SIMS.

The operating principle of FIB resembles that of SEM, but FIB uses a beam of ions, analogous to the way electrons are used in SEM. Fundamentally, FIB consists of an ion source, a focusing system, and a detector. The source is usually a liquid metal ion source (LMIS) that provides stable and highly focused ion beam. Gallium is a commonly used source material due to its low melting temperature, low volatility, low vapor pressure, and easy handling properties. [66] Liquid gallium provides a thin film that covers the tip of the emission source. When a positive voltage is applied to the needle, a high electric field is formed and it causes the liquid gallium to form a sharp Taylor cone due to electrostatic forces and surface tension. The gallium ions are generated by field ionization under the strong electric field. [39, 66] The disadvantage of the gallium is its propensity to implant the specimen surface causing contamination and amorphization of crystalline material. A sketch of the dual beam system and LMIS is shown in Figure 27.

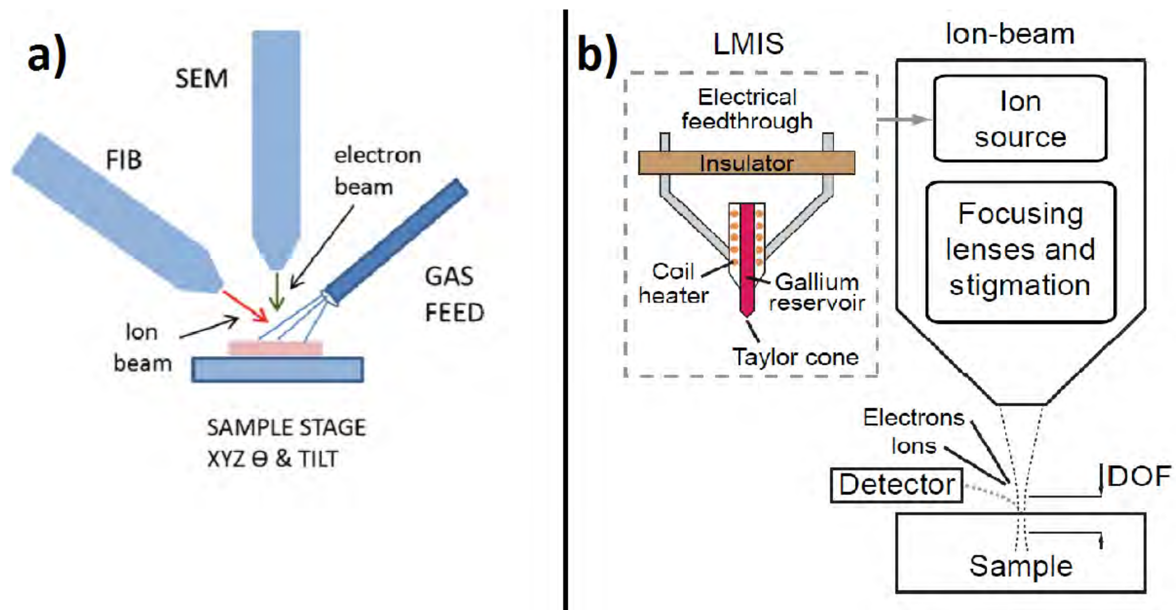

Figure 27: a) A dual beam system consists of FIB, SEM, and possible gas feed. The typical angle between SEM and FIB is 52°and the sample stage typically provides 5-axis movement (X, Y, Z, rotation and tilt) b) Positive voltage is applied to the liquid gallium covered needle. The gallium ions are generated by field ionization under the strong electric field. [67]

SEM and FIB can both provide a fine diameter beam. However, the dispersion of high energy ions limits the minimum beam size and SEM offers smaller beam diameter and better topographical contrast if same current and acceleration voltage is used. The beam diameter refers to a full width at half maximum (FWHM) value of the Gaussian profile of the beam. On the other hand, FIB outperforms SEM in a depth of focus (DOF) since heavy ions diverge more slowly than electrons. The DOF of FIB can be 100 μm but only 5-10 μm for SEM. [66]

FIB can use a two lens system or a one lens system. In a two lens system, an upper condenser lens is placed below the Taylor cone that collimates the ions into parallel beams that are passed through a mass separator. Below the mass separator, a drift tube disposes the ions that are not travelling as desired. The second lens is located underneath the drift tube and it reduces the spot size and improves focus. At the bottom, electrostatic beam deflector controls the path and probing location of the ions. The one lens system does not have the second lens since it uses an aperture to control the beam size. Furthermore, the one lens system produces a smaller beam size and higher milling speed than the two lens system. Additionally, the one lens system is inexpensive and heavy ion species can be used such as gallium. The advantage of the two lens system is the possibility to use various ion sources, such as H^+, He^+, and Ne^+. [68] The current density is controlled by the strength of the electrostatic lenses and/or size of the apertures. Figure 28 illustrates the two lens system.

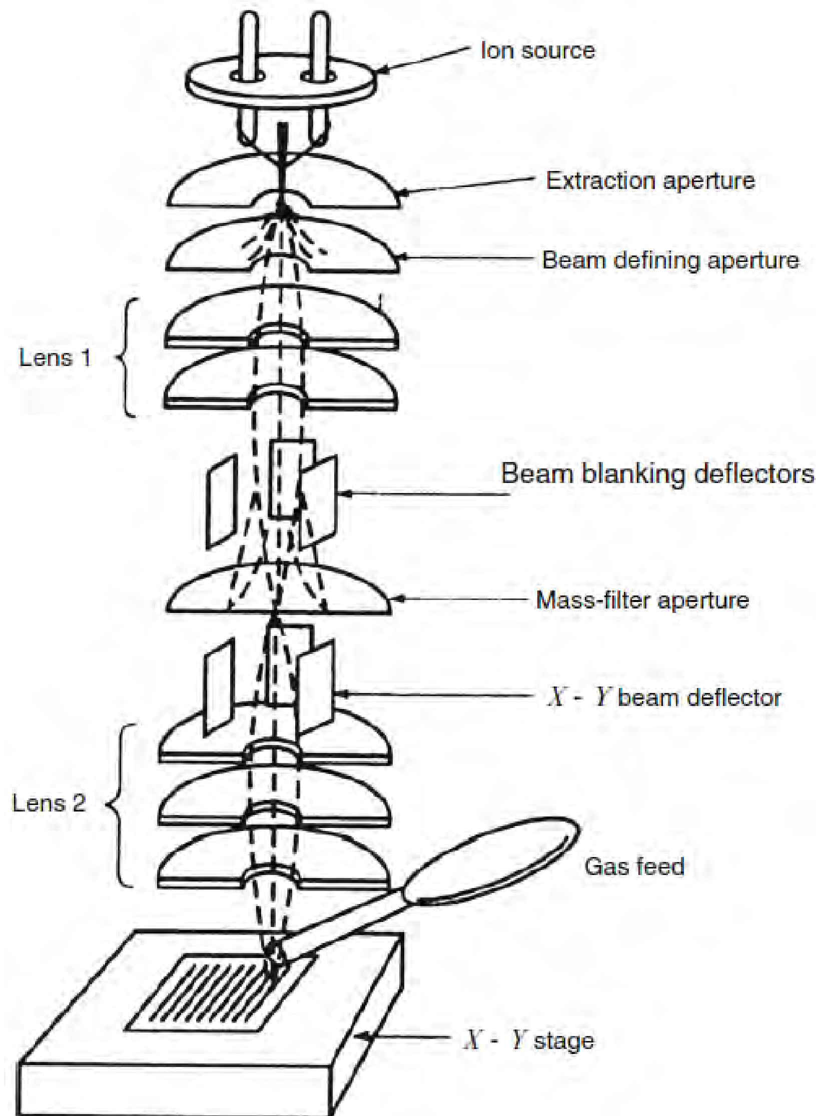

Figure 28: A two lens system consists of an ion source, an upper lens, a drift tube, a mass filter, beam deflector, and a second lens. In the one lens system, the second lens is replaced by the beam limiting apertures. [67]

The most important requirement for the ion source is that the ions should have high enough atomic mass to sputter the target atoms. Furthermore, the ion source material should have good wettability properties and it should not react chemically with the needle. For example, hydrogen or helium ions would cause only minimum sputtering since target atoms do not receive enough momentum to generate a collision cascade. [39] On the other hand, helium and neon ion beams can produce beam diameter below 1 nm if the source is cooled to cryogenic temperatures. This approach is used for very accurate and slow prototyping. A plasma ion source can generate a high current beam but the resolution is worse. However, the plasma ion sources are mostly used in the development of the multibeam systems that could be used for whole-wafer lithography. [67]

The interaction between the ion beam and the solid specimen is complex. Before stopping or ejecting from the sample, each incident ion may undergo multiple scatterings, elastic or inelastic processes. Elastic scattering causes sputtering if the transferred momentum is high enough to cause atom displacements. The struck atoms might generate secondary collisions causing a cascade of atomic collisions that is a requirement for the sputtering phenomenon. Inelastic collisions cause the transfer of energy to the target resulting in generation of subatomic particles as secondary electrons, Auger electrons, and photons. [39] An example of the interactions is shown in Figure 29.

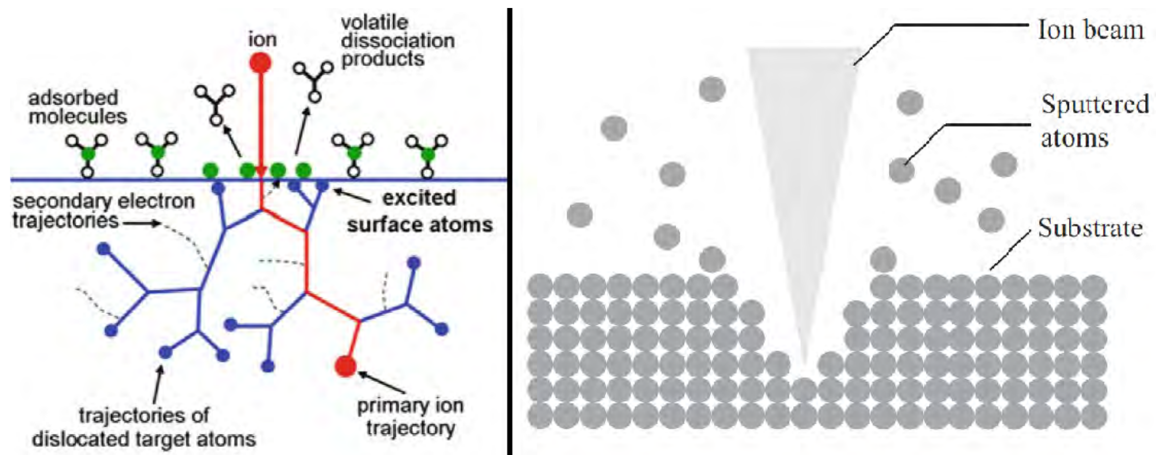

Figure 29: The incident ion penetrates in the specimen and might cause dislocation of the target atoms, that in turn can cause cascade collisions. With regular acceleration voltages, the primary ions stay in the specimen causing implantation. [67]

The sputtering rate is directly proportional to beam current and acceleration voltage. However, the most essential material parameter regarding ion milling is the sputtering yield, which is defined as a number of sputtered atoms per one incident ion. The sputtering yield depends on the incident angle since the ion path length inside the surface layer increases inversely proportional to the incident angle. In other words, the possibility for the target atom escape during the collision cascade increases when the angle of the collision is increased. Typically, the sputtering yield increases from 0°to 90°, 0°being perpendicular to the surface and the maximum is reached between 50 - 80°. On the other hand, the sputtering yield decreases when the ion beam approaches glancing incidence since the ions are reflected from the surface and collision cascades are terminated at the surface. The maximum sputtering yield depends on the sample material atomic number and acceleration voltage. [39] TRIM-simulations and measurements for sputtering yield in different angles are shown in Figure 30. Other things that affect the milling rate are surface contaminations, surface amorphizity, and local heating. Furthermore, one important parameter affecting the milling quality is the scanning speed. Slow scanning speed with no repetitive steps results in a higher milling rate but rougher and non-vertical surfaces. On the other hand, a fast scanning speed with repetitive steps results in a slower milling rate but good quality vertical sidewalls. [39]

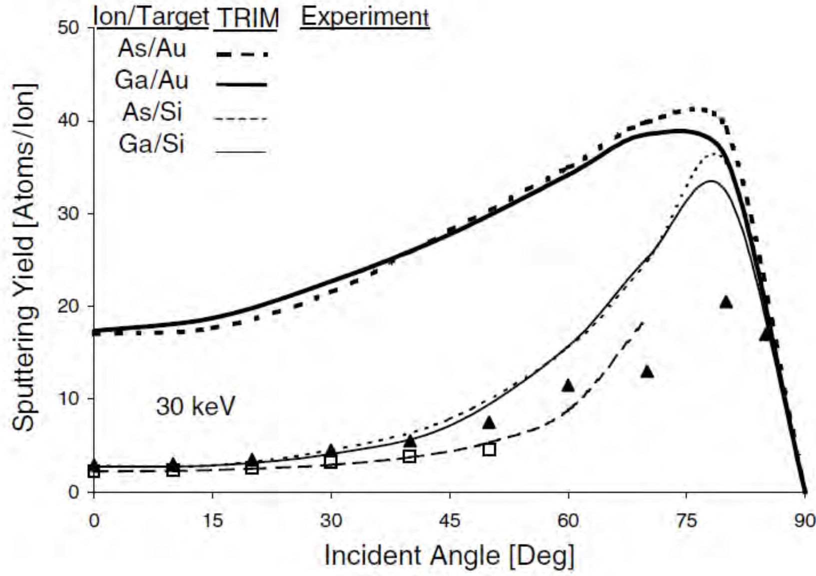

Figure 30: The sputtering yield depends on the specimen material, incident ion type, incident ion energy and incident ion angle. The 0°is perpendicular to the surface. [68]

The correlation between the sputtering yield and the milling rate is:

$$R = \frac{1}{N_T * q} * Y_S(\theta) * cos(\theta), \tag{14}$$

where N_T is the atomic density of the target material, q electronic charge, $Y_S(\theta)$ the sputtering yield and θ the incident angle. [69] If the materials are milled with same dosage and angle, the milling rate depends only on the atomic density and sputtering yield. The Equation 14 is used to calculate relative milling rates for silicon, copper, and tin in Table 5. [69]

Table 5: Tabulated relative milling rates for silicon, copper, and tin using equation 14. The milling rate depends on the sputtering yield and atomic density if the incident ion angle and ion dosage are constant.

Material	Silicon	Copper	Tin
Atomic density(cm^-3)	$5 * 10^{22}$	$8.46 * 10^{22}$	$3.7 * 10^{22}$
Sputtering yield (30 keV)	2.78	8.37	8.17
Relative milling rate	1	2	4

As seen in Table 5, FIB-milling is not very material selective. Practically, the calculated absolute values for milling rates might be too high. However, multiple studies have shown that the milling yield is closer to the 90° sputtering yield than the calculated value due to redeposition. [68] For that reason, it is useful to calculate relative milling rates if the specimen contains different materials, especially if different materials are not defined in the tool configuration. Generally speaking, normally

used acceleration voltages are that low that the incident ion never escapes from the specimen and the ion is always implanted within the specimen. If the acceleration voltage is considerably raised, the incident ions can escape from the specimen and the sputtering yield does not increase linearly. [66]

The grain contrast images of metals are formed by the combination of two phenomena. Firstly, different crystal planes have different etching rates. Due to that, the grain structure can be visible even in SEM after careful ion milling and polishing. Secondly, ions entering a crystal from a symmetry axis will encounter wide spaces between atoms penetrating deeper before scattering. This phenomenon is called channeling. Therefore, the channeling phenomenon results in roughened sample surface due to preferential milling rates. [67] Channeling contrast images are possible only for polycrystalline metals and not for crystalline semiconductors due to the ion beam induced surface damage.

Copper grains with different crystal orientations vary in mill rate by as much as 4. The (110) crystal orientation mills most slowly and it forms a Cu_3Ga phase when milled by Ga^+ ions. Furthermore, that phase is even more resistant to ion milling. [70] The relative milling rate for (110) orientation is 1, for (100) 2.3, and for (111) 3.6. In other words, the (110) plane has the most open lattice orientation (lowest atomic packing density). Therefore, the gallium ions can channel more deeply than in more densely packed lattice orientations. Figure 31 shows an example of sputtering yield of copper grains with different crystal orientations with respect to incident ion energy. The figure is based on measurements and transport of ions in matter (TRIM) -simulations. Differences in sputtering rates at different sections in the sample might produce curtain-like defects. The "curtaining" effect is more prominent if the specimen consists a stack of different materials that have different sputtering rates.

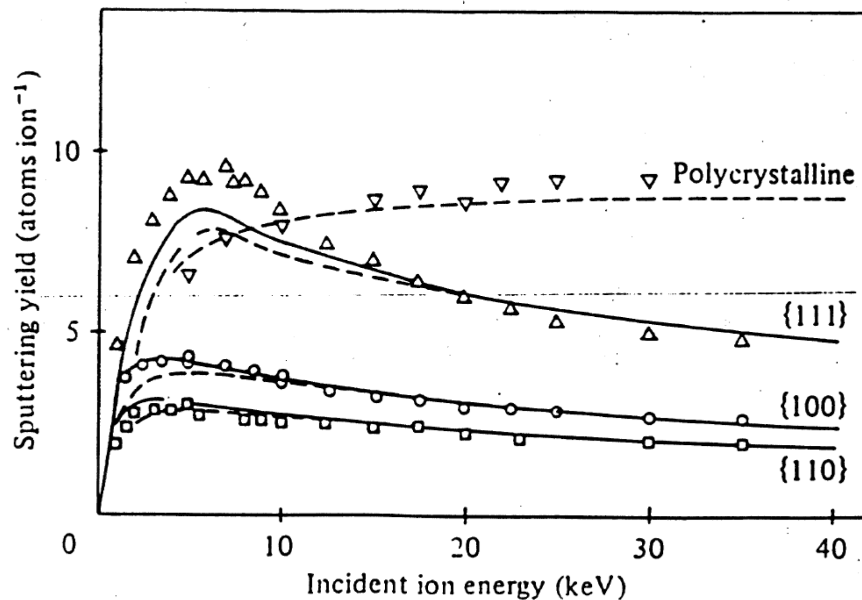

Figure 31: A sputtering yield of copper grains with different crystal orientations. The lines are based on TRIM-simulations. The values are calculated and measured for Kr^+ ions. [67]

Precursor gasses can be used for both deposition and enhancing milling of the material. Deposition with FIB is sometimes called ion beam assisted chemical vapor deposition that uses a hypodermic needle for has insertion. The ion beam crosses through the precursor gas, which is usually organometallic metal-carbon mixture. That means that if the substrate is not heated, the deposited material will contain a high amount of carbon and gallium. The metals deposited by FIB have clearly higher resistivity than the bulk material and, in turn, insulators have lower resistivity than the bulk material. Typical deposited materials are W, Pt, Al, Cu, C, and SiO_2. [67] The ions can induce chemical reactions by three mechanisms [67]: a) collision cascades that result in energetic surface atoms (dominant) b) emitted secondary electron that can participate in chemical reactions c) direct ion collision with a precursor gas molecule

In fact, there is a competition between milling and deposition since the dominant mechanism for both phenomena is the collision cascade. A collision cascade that reaches the surface and transfers sufficient momentum to the surface atom results in the sputtering. If there is a sufficient precursor gas surface coverage, the collision cascade dissociates the precursor gas. If the beam current density is too high, milling will occur even if there is precursor gas absorbed. The advantages of using precursor gas for FIB milling are highly increased milling rate and selectivity. For example, using Cl_2 gas for Si milling enhances the milling rate by 20x. Furthermore, the selectivity of precursor gases enables removing only desired parts of the sample. [67]

Forming an image or polishing by ion beam always sacrifices at least one monolayer of the specimen. The penetration depth for 30 keV Ga^+ ions is 29 nm in Si, 11 nm in Cu, and 17 nm in Sn. If the acceleration voltage is reduced to 5 kV, the penetration depths are reduced to 9 nm in Si, 5 nm in Sn and, 3 nm in Cu. [69] The penetration

depth corresponds to the thickness of the amorphized surface layer for crystalline materials. For polycrystalline metals, the penetration depth corresponds to surface layer with a high density of dislocation loops. [65] The penetration depths are not high if compared to SEM where the electrons penetrate in a depth of microns.

Other typical ion beam induced artefacts are defects, surface swelling, redeposition, and preferential sputtering. Those artifacts are challenging for TEM samples since they might result in decreased contrast in TEM imaging or additional peaks on EELS/EDX. The local heating effect is less than 100 degrees if the dwell time is on the order of microseconds. Strictly speaking, the heating effect is problematic only for polymers and biological samples. [65] Since the ion penetration depth is limited, thicker TEM samples will have relatively less damaged surface layer. Therefore, the TEM sample preparation with FIB is a tradeoff between defects and maximum imaging resolution. Generally speaking, conventional FIB sample preparation do not cause problems for (S)TEM and EDX, but the amorphized surfaces might be problematic for atomic-resolution HR-(S)TEM. Due to that, the last steps should be done using as low acceleration voltage as possible. To reduce the amorphized layer to zero, low energy argon ion polishing can be used for post-processing. However, the overall quality of the FIB-milled TEM sample is material dependent. Usually, a cross-section is broader at the bottom and the angle of the broadening depends on the materials in the sample. It is necessarily to tilt the specimen to each side before the final polishing steps to acquire parallel side walls. [65]

The advantage of the TEM sample preparation using FIB is that no mechanical preparation is necessary such as machining, dicing or polishing. It minimizes the sample deformation and preparation time. The commonly used lift-out technique is described in section 7.3. The other technique is the trench technique that requires sample preparation before milling and the geometry limits the tilt or rotation and EDX analysis is inaccurate due to spurious radiation from the side walls. [65] If the specimen surface is sensitive, a protective layer should be deposited prior FIB processing since FIB deposition will cause surface damage. [65] In fact, deposition process induces a 30 - 50 nm damage layer depending on the material and acceleration voltage [71]. The damage can be further minimized with dual beam systems, where the e-beam can be used for deposition. In addition to mentioned applications, FIB can be used for cleaning, via fillings, nanotomography, and etching mask designs.

5.4 Scanning Acoustic Microscopy

Scanning acoustic microscope (SAM) is a microscopy tool that uses mechanical waves which are sensitive to density and elastic properties of the sample [72]. The two types of acoustic waves propagating in a solid material are longitudinal and transverse waves. Furthermore, surface acoustic Rayleigh waves can also propagate along the sample-immersion liquid interface. The basic properties related to the mechanical waves are propagation velocity and absorption coefficient which increases proportionally to the used frequency. [73] The waves are attenuated in the material due to the absorption, scattering, and relaxation [74]. SAM measures the change in the amplitude and phase between the output signal and reference signal. The measurement obtains

information about wave velocity, acoustic impedance, attenuation, and geometric properties. [73]

A typical SAM consists of a transducer, a lens system, and an immersion liquid. If the microscope is a transmission type, there is an additional receiving lens and receiving transducer below the sample. The tool is illustrated in Figure 32.

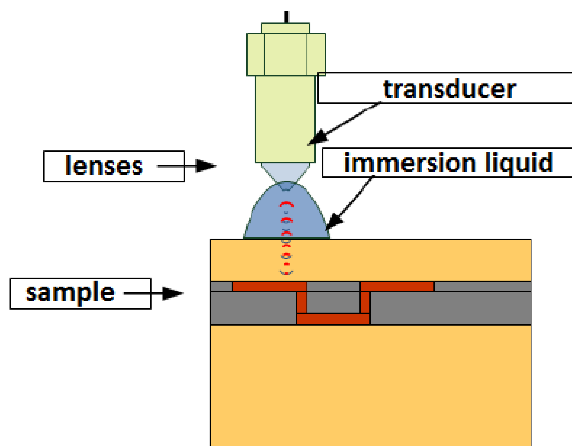

Figure 32: The piezotransducer generates mechanical waves that propagate through the lens system and immersion liquid to the sample. If the system is an echo-type, the same transducer is used to receive the signal, whereas transmission-type SAM has additional lens and transducer below the sample. [74]

Currently used transducers are piezoelectric and the generated acoustic waves propagate through a lens and a coupling material (liquid) to the sample. The coupling material has a larger refractive index than air and low absorption coefficient to increase the resolution and contrast of the microscope. The acoustic wave can be partially reflected or scattered in the sample. The microscope is operated in a reflection mode if the reflected wave is measured. In the same way, if the transmitted wave is detected, the microscope is operated in a transmission mode. [73]

The lateral resolution depends on the used frequency, lens system, immersion liquid material, focal length and properties of the sample. The depth resolution depends on the bandwidth which in turn depends on the mechanical and structural properties of the piezoelectric transducer. Although the resolution limitations are usually related to the lateral resolution that is in order of the wavelength of the wave in the immersion liquid. However, since the absorption coefficient increases proportionally to the frequency, there is always a trade-off between resolution and penetration depth. [73]

SAM can be used in different scanning modes. B-scan is a cross-section perpendicular to the surface, whereas C-scan is a cross-section parallel to the surface. A-scan is the acquired signal as a spectrum. There exist several different scanning modes, but the C-scan is the most popular for SAM-imaging. [75] Furthermore, there exists various modifications to the basic system. For example, SAM can be used in a scattering mode by rotating the lens in various angles. The mode is analogous to the DF mode in other microscopies offering controllable resolution depth. Another

modification example is the measurement of the local speed of sound, such as the velocity of surface Rayleigh waves. Moreover, SAM operated at cryogenic temperatures can achieve a resolution of 30 nm. The usefulness of SAM is extended by computer imaging processing that improves the image quality and resolution. [73] An example of a C-section is shown in Figure 33.

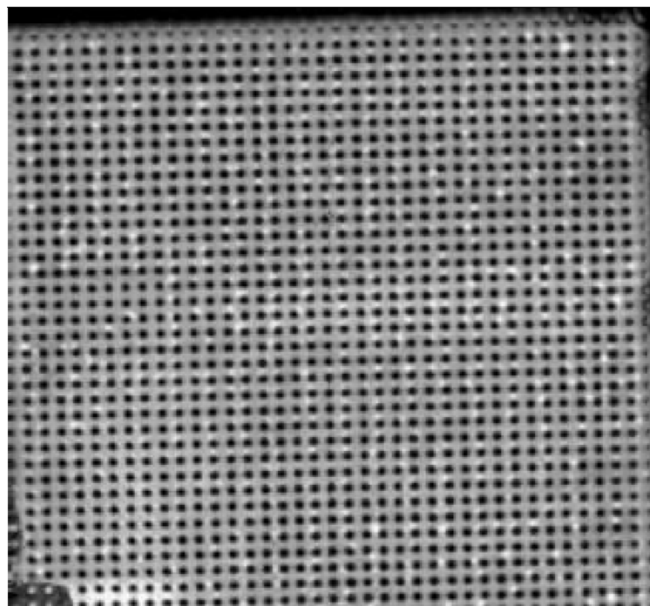

Figure 33: A processed C-section of a conventional flip-chip. The delaminated areas are shown as a brighter contrast. [75]

SAM is fairly sensitive to buried defects due to mismatch of acoustic impedance at the boundaries. The typical detected defects are adhesion failures, exfoliation, microcracks, thickness variations, size differences, orientation, and distribution of grains. [73] Furthermore, SAM is very sensitive to air gaps since air has very low density and high reflectivity. The ability to detect air gaps is greater than the resolution limit of SAM. Since the wave attenuates in the material, SAM is most sensitive to surface defects and less sensitive to defects that are located deeper in the material. A good practice is to use comparative measurements that use a reference sample to confirm the results. SAM is very sensitive to surface roughness since irregularities will scatter and reflect the mechanical waves, i.e. it is not possible to detect defects that are finer than the surface roughness. [72]

The typical frequency range for conventional SAM is 5-250 MHz but with current transducers the frequency can be raised up to 2 GHz. The increased frequency increases the lateral resolution from $\sim$30 μm to 1 μm but decreases the penetration depth from $\sim$100 μm to $\sim$10 μm limiting the usage of the tool for near-surface regime [74] Furthermore, GHz-SAM is even more sensitive to the surface roughness and the processing of the data is more demanding due to excitation of additional surface wave modes. [75] Low-frequency SAM uses pulsed waves, whereas GHz-SAM uses very high-energy pulses to compensate the attenuation. Moreover, the depth of

field is very narrow since the focal length must be reduced to accurately focus the high frequency waves. [72]

SAM is a non-destructive and relatively fast technique to obtain data from fairly large buried defects. The major disadvantage of the tool is the trade-off between penetration depth and lateral resolution which is still limited at 1 μm. Furthermore, the high-frequency use is mainly limited to the surface or near surface region.

5.5 Comparison

The techniques reviewed in section 5 were quite different. For example, SAM is usually used for detecting fairly large buried defects due to its low resolution, whereas FIB is useful for (S)TEM sample preparation and grain analysis. Table 6 presents a comparison between the reviewed techniques. However, the numerical values in the table are only approximations due to differences between tools, imaging modes and samples.

Table 6: Tabulated properties of the reviewed techniques based on Section 5

	TEM	STEM	FIB	SAM	GHz-SAM
Probe species	Electrons	Electrons	Ions	Acoustical waves	Acoustical waves
Detected species	Electrons	Electrons	Electrons/ions	Acoustical waves	Acoustical waves
Depth resolution	5 nm	5 nm	1 nm	<100 nm	<100 nm
Lateral resolution	0.1 nm	0.2 nm	10 nm	20-50 μm	1 μm
Penetration depth	500 nm	500 nm	20-50 nm	50-100 μm	5-10 μm

GHz-SAM is fairly new technique but the resolution is still lacking for submicron applications. For example, the typical size for Kirkendall voids in the range of 100 nm which is well below the lateral resolution limit of SAM. Furthermore, low frequency SAM is not usable for micro-connects at all due to very low lateral resolution. On the paper, the lateral resolution of FIB seems reasonable, but in real use usage of small diameter beam damages the sample quickly reducing the practical resolution to tens of nanometers. Likewise, the penetration depth of electrons in (S)TEM is fairly high but it is not the only factor for limiting the sample thickness. Generally speaking, TEM samples are usually <100 nm thick, whereas STEM samples can be a bit thicker due to the different operating principle. Certainly, STEM can be used for thicker specimens as well as for thinner specimens with higher intensity than TEM. However, it is not always possible to know beforehand whether STEM or TEM is more suitable for the particular sample.

6 State of the Art in Micro-Connect Characterization

This section reviews modern applications of the introduced techniques. The section of impurity analysis gave an insight into the typical impurities in electroplated copper and proposed different analysis techniques to detect those impurities. The reviewed techniques were selected on the basis of the usability for solid materials, availability and easiness of sample preparation that should not change the properties of the sample. Spectroscopes that involve dissolving the solid sample were not considered due to inability of depth profiling and inaccuracy in elemental concentrations due to different level of dissolutions. This section gives an insight into research that is related to micro-connects using the reviewed techniques.

RBS has not been used for micro-connect impurity analysis since RBS is nearly blind to lighter elements. In the field of 3D integration, RBS is usually used for diffusion barrier evaluation [76–78], electromigration studies [79], copper line studies [80], diffusion studies [81], SLID bonded ceramic-metal interdiffusion studies [82] or as a complementary technique to other elemental analysis techniques, such as SIMS [83]. The possibility for non-destructive depth-profiling of the whole micro-connect has not been yet used. RBS is very accurate for heavy elements if their mass difference is high enough, as seen in Figure 18. Since the copper micro-connects contain relatively heavy elements, such as Sn, Ag, Al, Ti, and Mn as layers or alloying elements, RBS could be used to measure the exact composition through the whole interconnect without destructing the sample. Additionally, RBS could be used for diffusion measurements near the silicon interface to evaluate the diffusion barrier properties. This kind of measurements could be done to evaluate the effect of annealing, electromigration and metal deposition parameters on the characteristics of the micro-connect.

ERDA, especially ToF-ERDA is a rarely used technique, probably due to its low availability. In Finland, it has been used by University of Jyväskylä and University of Helsinki to measure impurity contents in ALD metal nitride, copper, and ruthenium thin films. [84–87] Metal nitride thin films are traditionally used as diffusion barriers and copper thin films as seed layers. The ability to measure light elements without destructing the sample is attractive and ToF-ERDA has been used to measure hydrogen and carbon contents in low-k dielectris [88]. The technique is quantitative without standards, therefore, there exists less uncertainty compared to SIMS. Since the depth profile is not as deep as for RBS, ToF-ERDA is not necessarily suitable for measuring a depth-profile through the whole micro-connect. However, the lateral resolution is superior to RBS. This kind of surface technique would be most suitable for surface analysis. Furthermore, the impurities, such as Cl and S are located at the surface of the copper micro-connect and those impurities might have a drastic effect on the interconnect reliability. Finally, most of the fabrication processes involve wet etching that causes impurity residuals in the material. Those residuals could be accurately measured and the effect on the reliability could be studied.

Since most of the current (S)TEMs have an EELS detector, the usage of EELS is mostly limited by the sample preparation process. The sample thickness should usu-

ally be less than 50 nm depending on what elements are measured. Additionally, the sample should not have surface contaminants or defects from the sample preparation process. Nevertheless, EELS has been used a lot to characterize segregation in copper for elements such as nickel [89], bismuth [90], tin [91], silver, and antimony [92]. However, the ability to measure light elements precisely, which is the greatest advantage if compared to EDX, is less used for impurity segregation studies. The feature of light element detection has mainly been used to detect oxygen at bonding interfaces of SLID bonds [93] or copper-copper bonds [94]. Though, it is possible to map the whole area of a SLID bond [85] or a microbump [95]. Due to the high resolution of EELS, it can be used for very specific purposes, such as analysing bonding mechanism inside of an IMC layer [96]. Granted, that the sample preparation is challenging, there should not be a reason not to analyse a micro-connect by EELS if (S)TEM is used for structural characterization. By one measurement session, the user can acquire the structure as well the impurity segregation at grain boundaries and composition of the interconnect.

AES should not be confused with inductively coupled plasma atomic emission spectroscopy (ICP-AES) that is mainly used for liquid samples in biosciences, whereas AES is a surface technique for solid samples. Usually, XPS is favored over AES for surface characterization since AES suffers from problems related to surface charging. However, sputtering depth profiles with AES are more simple, the detectors are not sensitive to angle variations and the lateral resolution is good. AES is especially suitable for micro-connects since they consist mostly of conducting materials. That has been noticed and AES has been used for depth profiling Cu-Sn SLID bonds [97] and chemical mapping of microbumps [98–100]. Similar to the other techniques, AES has been used for diffusion barrier evaluation [101]. The most interesting application regarding this thesis is the measurement of S near Cu_3Sn/Cu interface related to Kirkendall voiding [17, 18]. Since it is a good practice to measure impurities with at least two different techniques, AES has been used as a complementary technique for ToF-SIMS [102]. Furthermore, AES can be used for traditional solder composition studies [103, 104]. As can be noticed, AES is not yet a forgotten technique and it has seen more usage during the last ten years. Fundamentally, AES is a rivalling technique to XPS. Therefore, it should be carefully considered which one is more suitable for the chemical analysis.

SEM-EDX is probably the most used chemical analysis technique due to its wide availability. In addition, it is quick, versatile, inexpensive, and it enables possibility for point analysis, line scanning and dot mapping. However, SEM-EDX is usually classified as qualitative or, at most, as semi-quantitative technique, especially for lighter elements. Therefore, SEM-EDX is used for numerous different applications. Some applications are, for example, interconnect composition analysis [105, 106], interconnect IMC identification [107, 108], and microbump metallurgy analysis [109, 110]. All these applications are limited by the fact that SEM-EDX cannot be used for trace analysis or depth profiling similar to the other techniques. (S)TEM-EDX offers more possibilities regarding those areas due to better spatial resolution, lower interaction volume and increased quantification possibilities. However, (S)TEM-EDX has been used remarkably less for micro-connect related characterization. The typical

applications have been an evaluation of copper, tin, and bismuth diffusion [111, 112], Cu-Cu bonding characterization [113], and diffusion barrier evaluation [114]. The most interesting application regarding this thesis is the impurity segregation analysis in copper [111, 112]. Although, (S)TEM-EDX has not yet been used for impurity segregation analysis inside Kirkendall voids.

SIMS is the most sensitive surface analysis technique with an elemental detection limit in the range of ppm/ppb. Due to the high sensitivity, it is very suitable for trace element analysis. Therefore, it has been used a lot to analyse impurities in copper thin films [16–18, 20, 22–25, 115] or copper TSVs [116], for example, in studies related to Kirkendall voiding. However, SIMS depth-profiling is challenging due to high sensitivity to surface roughness and ion channelling effect. In the case of multiple phases, such as Cu/Cu_3Sn, SIMS is used to analyze the copper and Cu_3Sn is analysed by a complementary technique, such as AES [15, 19]. SIMS is a quantitative technique if standards are available for the characterized material. Therefore, the simplest application is confirmation of elemental presence, such as confirmation of a seed layer removal [117], confirmation of an oxide layer removal [118] or confirmation of the functionality of a diffusion barrier layer [119]. Additionally, SIMS can be used to analyse impurities at grain boundaries if the grains are big enough [120, 121]. SIMS is very attractive for trace element analysis due to its high sensitivity and availability of standards. However, the challenges related to the surface roughness and depth profiling of multiphase samples require using a complementary technique to verify the results.

XPS is a true surface analysis technique similar to AES. However, XPS can be used to measure insulating samples but the beam size is drastically larger and XPS cannot detect hydrogen and helium accurately. XPS cannot differentiate sections of elements if the sections are smaller than the beam that is 10-200 μm wide. Due to the low lateral resolution, XPS is suitable only for characterization of a micro-connect average chemical composition. Compared to AES, there exist considerable fewer XPS studies related to copper based interconnects. XPS is typically used for bonding characteristics of wafer level Cu-Cu bonds [122, 123], composition studies of copper surface [124, 125], Sn-Ag surface studies [126, 127], and Cu-Sn surface studies [128]. Similar to ERDA, XPS is very suitable for thin film characterization, such as for thin diffusion barriers [129]. The novel applications of XPS include analysis of copper surface segregation [130, 131] and TSV stress characterization [124, 125].

SEM is still the tool for electron microscopy due to easiness of operation and sample preparation. However, (S)TEM is the first choice if the resolution of SEM is not enough. Moreover, the only major limitation is the challenging sample preparation. (S)TEM can be used for numerous different applications. Just to name a few, (S)TEM can be used to inspect twin boundaries in copper [132], IMC/Cu interface [133–135], Cu-Cu bond interface [136, 137], microbump bond interface [138], and Kirkendall voids [18, 133]. However, due to the sample preparation challenges there exists less micro-connect (S)TEM studies that one would assume based on the availability of the tool. There is clearly a need for further (S)TEM studies regarding Kirkendall voiding and grain boundaries inside of a micro-connect.

No other technique can compete with FIB for accurate TEM sample preparation.

Recently, FIB has been used more and more for imaging purposes due to high grain and material contrast. Furthermore, FIB is used even for SEM cross-sections due to challenges in abrasive polishing that might cause surface defects and material transportation. The resolution of FIB is lower than that of SEM but still in the same order of magnitude. However, FIB is not a competitive technique to SEM since most of the current FIB-systems are dual beam systems. The major disadvantage of FIB imaging is the surface damage and residual gallium ions. FIB imaging is mostly used for characterization purposes, such as for evaluation of copper microstructure [139, 140], Cu-Sn microbumps [135, 141–143], SLID bonds [143–145], and Cu-Cu bonds [146, 147]. Additionally, there exist more unique applications, such as EBSD sample preparation [141], inspection of nanotwinned copper [148, 149] and inspection of Kirkendall voids [135, 143, 150]. Altogether, FIB is a great tool for cross-sectioning and polishing, especially if the features are small such as Kirkendall voids [151]. If the operator is experienced, FIB can produce decent pictures for microstructure evaluation relatively fast. Furthermore, the grain analysis does not require heavy computation as shown in section 5.1.

SAM is a non-destructive technique to characterize buried defects and inhomogeneities, such as microcracks, voids, and delaminations. However, the lateral resolution of typical SAM is in the range of tens of μms and the penetration depth is approximately 100 μm. The resolution and penetration depth depend on the used frequency (in water) which is typically a few hundred MHz. However, if the frequency is raised to 1-2 GHz, the lateral resolution is increased below 1 μm but the penetration depth is decreased to 10 μm and the depth of field suffers drastically. SAM can detect defects, such as voids, below the lateral resolution limit but those defects appear as too big in the captured images due to beam spreading. Usually, SAM is used to detect defects in flip-chip interconnects [152, 153] which are considerably larger than micro-connects. The other uses are inspecting the interface of wafer level SLID bond [154] or Cu-Cu bond [155], detecting voids in copper TSVs [156], and inspecting underfill quality [157, 158]. GHz-SAM is a newer technique and it has been mainly used for TSV characterizations [72, 74]. However, SAM requires a smooth and homogeneous surface to detect accurately buried defects and that might result in very challenging sample preparation process.

Each reviewed technique has their advantages and disadvantages but the requirements for sample surface roughness and homogeneity are quite similar. Furthermore, most of the ion-sputtering based depth profiling techniques suffer from the sensitivity for matrix coefficient that is especially challenging with IMCs such as Cu_3Sn. In that sense, chemical analysis of Cu-Sn based micro-connects requires atleast two different complementary techniques, such as SIMS for trace analysis of copper and AES to analyze impurities in IMCs. Furthermore, (S)TEM-EDX is the most suitable technique for locating the impurities since sample preparation for EELS might dissipate impurities that are located in small defects such as Kirkendall voids. SEM is helpful only for general overview of the micro-connect, therefore (S)TEM should be used for accurate characterization of grain boundaries, interfaces, and defects. FIB has its worth for grain analysis due to its high grain and material contrast without complicated sample preparation.

7 Materials and Methods

This section presents the used sample preparation methods. The chosen approach was to investigate the Kirkendall voids and the microstructure by large-area depositions since manufacturing of micro-connects is time-consuming. The behaviour of Kirkendall voids in large-area metal films is assumed to be same as in micro-connects if the film thicknesses are in the same order magnitude as the typical micro-connect dimensions. The Cu and Sn films were electroplated on a silicon wafer and the chosen investigation tools were FIB, SEM, GHz-SAM, (S)TEM and STEM-EDX.

7.1 Sample Preparation

The typical substrate choices to characterize electroplated Cu-Sn are silicon wafers and brass plates. However, the seed layer type has an effect on the microstructure of the electroplated copper. Therefore, the brass plates are discarded since silicon wafers combined with PVD-deposited seed layers are closer to the real world applications. The used 4" silicon wafers were n-type and the metals were deposited on the whole wafers. A chromium diffusion barrier and a copper seed layer were deposited directly on top of a native oxide using an Oxford Instruments Sputter Plasmalab. Both sputtering recipes used a 500 W plasma power and a 50 sccm argon flow and the tool was operated at the room temperature. The target thicknesses were 100 nm for both chromium and copper films. However, the known thickness variation of the Oxford Instruments Sputter Plasmalab depositions is approximately 20%.

The list of the used samples is tabulated in Table 7. The layer thicknesses were chosen so that the total thickness is low enough to represent a micro-connect but thick enough to form a sufficient amount of IMCs when annealed at 150 °C. The used additives for the electroplating were Bis-(3-sulfopropyl)-disulphide (SPS), Polyethylene glycol (PEG), and SPS+PEG since they are the most commonly used. The basic solution A was a low purity electrolyte, whereas the basic solution B was semiconductor grade containing fewer impurities. The A/B/D-type samples were deposited using approximately one-year-old copper electroplating solution, whereas C-type samples were deposited using a high purity, freshly made solution. The chemistry and the manufacturers of the used copper electrolytes are described in Appendix A.

Table 7: Tabulated list of the samples used in this thesis. The layer thicknesses are target values and bath age "new" refers to freshly prepared electrolyte, whereas "old" refers to the one-year-old electrolyte.

Sample	Tool	Copper bath type	Layer thicknesses	Annealing
A-1	TEM	SPS old	3 μm Cu+3 μm Sn	No
A-2	TEM	SPS old	3 μm Cu+3 μm Sn	150 °C 4 hours
B-1	FIB	SPS old	3 μm Cu+3 μm Sn	No
B-2	FIB	SPS old	3 μm Cu+3 μm Sn	150 °C 4 hours
B-3	FIB	SPS old	3 μm Cu+3 μm Sn	150 °C 24 hours
B-4	FIB	SPS+PEG old	3 μm Cu+3 μm Sn	No
B-5	FIB	SPS+PEG old	3 μm Cu+3 μm Sn	150 °C 4 hours
B-6	FIB	SPS+PEG old	3 μm Cu+3 μm Sn	150 °C 24 hours
C-1	FIB	SPS new	3 μm Cu	No
C-2	FIB	SPS new	3 μm Cu+3 μm Sn	150 °C 24 hours
C-3	FIB	PEG new	3 μm Cu	No
C-4	FIB	PEG new	3 μm Cu+3 μm Sn	150 °C 24 hours
C-5	FIB	Basic solution A new	3 μm Cu	No
C-6	FIB	Basic solution B new	3 μm Cu	No
D-1	FIB	SPS+PEG old	10 μm Cu	150 °C 24 hours

The A/B/D-type samples were deposited using a conventional setup that is shown in Figure 34. The used current profile was DC with an open voltage and the total current was controlled by the power supply. The used current density was 10 mA/cm^2 for all depositions. The current density was chosen based on the preliminary tests that showed worse quality depositions for higher current densities. The current was turned on before the samples were inserted in the bath (hot-entry) to avoid premature copper seed layer etching and the electrolyte was agitated by a magnetic stirrer at 300 rpm. After the copper electroplating, the wafers were immersed in DI-water to avoid post-etching. The tin layers were deposited in a similar fashion using a NB Semiplate Sn 100 (NB Technologies) electrolyte.

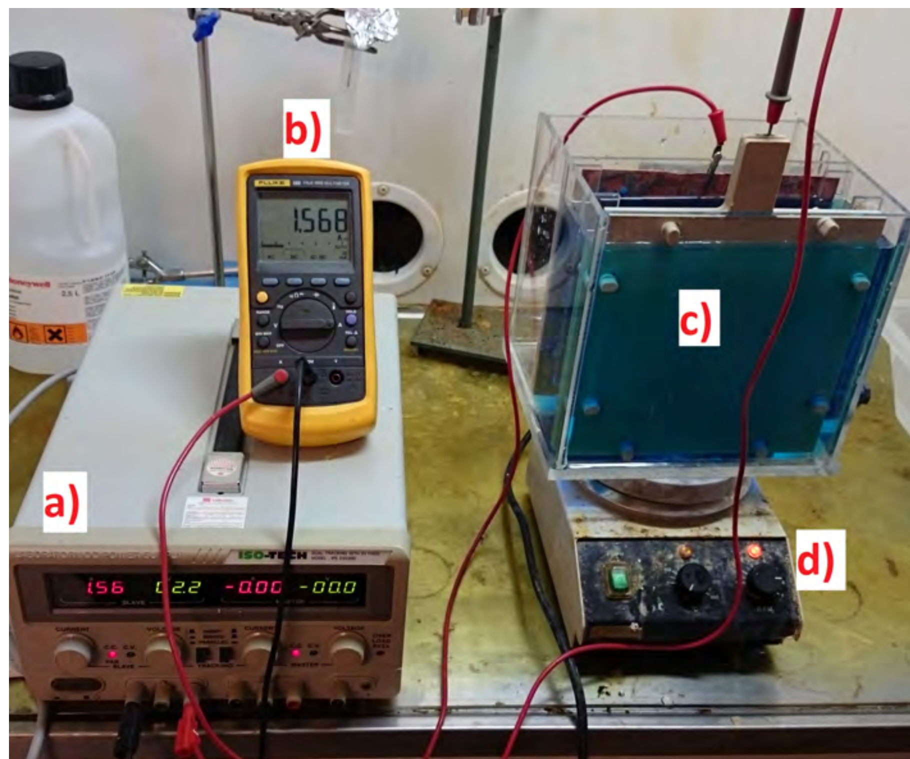

Figure 34: The conventional setup consists of a) a power supply b) a current meter c) an electroplating bath, a cathode, and an anode d) a magnetic stirrer.

To decrease the amount of impurities, C-type high purity samples were deposited using a hull-cell shown in Figure 35. The 267 ml trapezoidal hull cell reduces the amount of wasted electrolyte and the silicon wafers can be cut in a half. Since the specimen is placed at an oblique angle, a range of current densities can be analysed in a single electroplating run. However, only the section corresponding to 10 mA/cm^2 was used for characterization. In addition, the C-type samples were cleaned using a 500 W oxygen remote plasma prior the copper electroplating to reduce the amount of impurities and to the increase wetting properties of the wafer surface. After the electroplating processes, the samples were diced into 1.5 x 1 cm pieces. However, the samples were not characterized immediately after the depositions but they were stored at a room temperature for several weeks.

Figure 35: The high purity samples were electroplated using a hull cell. The wafers were cut into two halves and a piece of copper-tape was attached to the edge for the electrical contact.

7.2 Grain Revelation by FIB

FIB was chosen as an alternative technique in place of EBSD, XRD or metallographical etching to study the grains. The samples were prepared using a FIB Helios 600 by following steps and it was assumed that the combined Cu-Sn thickness was ~6 μm:

1. Tilt sample to 52 ° (eucentric height)
2. Mill a 10*20*1.6 μm rectangle cross-section with a 30 kV 21 nA beam
3. Tilt sample to 57° (5 ° relative to the ion gun)
4. Polish by a 100 nm deep cleaning cross-section with a 30 kV 38 pA beam
5. Polish by a 100 nm deep cleaning cross-section with a 30 kV 9.7 pA beam
6. Polish by a 50 nm deep cleaning cross-section with a 16 kV 11 pA beam
7. Polish by a 50 nm deep cleaning cross-section with a 16 kV 3 pA beam
8. Repeat the last cleaning steps until the grains are visible and the amount of defects is decreased

It should be noticed that the chosen depth of 1.6 μm is actually with silicon parameters and it translates to 10 μm depth in the Cu-Sn. However, it was discovered that this kind of approach is slow and the curtaining effect is strong. The sample preparation was changed into following to maximize the efficiency:

1. Tilt sample to 52° (eucentric height)

2. Deposit a 12*2*2 μm platinum rectangle with a 30 kV 0.92 nA beam

3. Mill a 16*10*2 μm rectangle cross-section parallel to the platinum with a 30 kV 21 nA beam

4. Tilt sample to 54° or 50° depending on which side is the rectangle in relation to the platinum rectangle

5. Polish by a 30 kV 2.8 nA cleaning cross-section (adjust depth for 2-minute run)

6. Polish by a 30 kV 0.28 nA cleaning cross-section (adjust depth for 2-minute run)

7. Repeat the last polishing step until the grains are visible and the amount of defects is decreased

The sample preparation time was reduced from seven hours to one hour. Furthermore, the amount of polishing steps could be reduced since the gallium ions could not damage the sidewall and the Sn surface due to the protective platinum layer. The preparation was taken even further to prepare samples for BSE-SEM. The problem with a BSE-detector is the short distance between the detector and sample surface. Therefore, a 45° sample holder should be used to minimize the need for tilting. The sputtering angle was changed to 7° producing a 45° cross-section since the ion gun is in a 52° angle. Since the cross-section and the BSE-SEM holder are both in a 45° angle, the combined angle is 90°. Therefore, the electron beam is perpendicular to the sidewall during the imaging. However, if the layer thicknesses are calculated from the BSE-SEM images, the non-typical angle for the cross-section should be taken into account. Samples manufactured by the same method can be used for SE-imaging also. The used dedicated SEM was JEOL JSM-6335F that uses a field emission gun (FESEM).

7.3 TEM Lamella Preparation

The TEM-samples were prepared using a FIB Helios 600 by following steps and it was assumed that the combined Cu-Sn thickness was $\sim$6 μm and lamella target thickness 200 nm to prevent dissipation of impurities:

1. Bend the non-used poles before attaching the sample holder and the copper grid

2. Tilt sample to 52°

3. Deposit a 15*2*2 μm platinum rectangle with a 30 kV 0.92 nA beam

4. Mill a 20*12*2 μm rectangle cross-section at both sides of the platinum with a 30 kV 21 nA beam (additionally, a small rectangle cross-section at the nose of the platinum so that the lamella is attached only from one side)

5. Polish by a 20*2*2 cleaning cross-section with a 30 kV 2.8 nA beam
6. Tilt sample to 0°
7. L-Cut: cut through the lamella from the bottom and the attached side with a rectangle cross-section that is $\sim 1\mu$m wide and 3 μm deep (leave 4 μm silicon to hold the sample in place)
8. Rotate the sample by 180° and check that the L-Cut goes through the sample
9. Rotate sample back to the default position and insert the micromanipulator and position it within ~200 nm of the lamella
10. Insert GIS needle and deposit a ~1*1*1 μm platinum rectangle between the micromanipulator and lamella
11. Do not remove the GIS needle yet! Raise the beam current to the maximum and cut through remaining silicon so that the L-Cut is transformed into an U-Cut
12. Lift the sample using the micromanipulator and remove the GIS needle
13. Find the copper grid and change the eucentric height based on the grid (grid is lower than the sample holder)
14. Position the lamella within 1 μm of the grid (on the top part) and insert the GIS needle
15. Position the lamella within ~200 nm of the grid and deposit ~1*5*1 μm platinum rectangle between the lamella and the grid (one side is enough!)
16. Do not remove the GIS needle yet! Raise the beam current to the maximum and cut through the platinum between the needle and the lamella
17. Raise the micromanipulator and retract the GIS needle
18. Tilt sample to 54°
19. Polish by a 1 μm deep cleaning cross-section with a 30 kV 0.46 nA beam
20. Repeat with a 50° tilt
21. Repeat both previous steps until the sample thickness is 200-300 nm
22. Tilt sample to 57°
23. Clean the sample by a rectangle cross-section with a 5 kV 46 pA beam (adjust depth for 2 minute run)
24. Repeat with 45° tilt

25. The sample should be finished, remember to bend the pole back into the position

The amount and type of polishing depend on the sample type. For example, the Cu-Sn samples are sputtered fairly fast and the user should be very careful not to mill through the sample while polishing. Furthermore, since silicon is milled six times slower than the Cu-Sn, the lower section of the lamella stays too thick while Cu-Sn is totally polished. Due to the same effect, it is challenging to approximate the sample thickness since the silicon is dominating when imaging from above. The average time to prepare a TEM-sample is 5-10 hours depending on the amount of failed runs. With a perfect run, the sample can be prepared in 3 hours. The surface gallium concentration should be less than 10 at% and the total average gallium contamination $\sim$1 at% [39]. The used STEM was FEI Titan^3 G2 60-300. The next section discusses the problems faced with the FIB Helios 600 at Micronova.

7.4 Practical Advice for FIB Helios 600

Each FIB is a unique system. Therefore, there exist types of faults whose origin is not clear. For example, the depth of the cross-section should be controlled since too deep cross-section causes "shadowing" at the sidewalls. The shadowing complicates accurate imaging and tracking of the ion polishing process. Choosing correct depth parameter might be challenging since the software does not have sputtering yields for most of the metals. For example, the Cu-Sn will be milled six times faster than silicon. Moreover, when polishing the sample or a feature, the cleaning cross-section should not be too small or too large. If the drawn box for polishing/milling goes over or below the feature, the curtaining effect will be definitely seen. Operating FIB requires good spatial perception since it is not always clear how the sample should be tilted based only on the SEM/FIB images. Furthermore, the parameter for depth behaves differently if the specimen is tilted. It was observed that the FIB Helios 600 at Micronova is prone to drifting if the total sample preparation for a single time is short or if a single polishing step is too long. Adding more graphite tape for better contact did not help. The drifting could be decreased by preparing a dummy cross-section with a maximum beam current. Furthermore, if the same specimen was used again in the next day, the drifting disappeared.

TEM-sample preparation with the FIB Helios 600 at Micronova is definitely challenging. The learning process is iterative and each user has their practices to prepare the sample. However, different practices may not have any scientific base. The most problematic feature regarding the FIB Helios 600 is the vibration during insertion/removal of the GIS needle. To bypass this problem, the GIS needle should be left in place while lifting/attaching the lamella. However, since the GIS needle is inserted, some metal is deposited if high enough current is not used, i.e. the sample is easily destroyed if the operator has not properly focused the image before the GIS needle insertion. The second problem is related to the micromanipulator. The sensitivity of the X- and Y-axis are different. The user might use high sensitivity in order the save time but destroying the sample when forgetting the sensitivity

difference. A good compromise is to move the micromanipulator in different directions separately while changing the sensitivity. The third problem is related to the attaching of the lamella to the copper grid. The lamella is easily disoriented when depositing the platinum between the grid and lamella. This problem can be reduced by bending the not needed grids before the attachment. However, the grids should be bent back into place after the polishing to protect the sample. Additionally, TEM Grid Boxes are suitable only for storing the sample and sending the sample in the mail requires using Gel-Paks.

8 Results and Discussion

The results of structural and impurity analysis are presented in this section. First, the results of characterization using FIB, SEM, TEM and GHz-SAM are presented in Section 8.1. The results of the impurity analysis are presented in Section 8.2. The main focus of this whole section is to present analysis and discussion related to grain size, IMC identification, Kirkendall void identification, and impurity analysis near or inside Kirkendall voids.

8.1 Structural Analysis

The focus for the structural characterization is in the grain size analysis. However, size and distribution of the voids are not forgotten and the IMCs are identified in each case. GHz-SAM is used only for the void characterization in contrast to FIB, SEM, and TEM. The grain size growth should depend on the copper thickness and plating bath chemistry [159]. Even though, the correlation between the plating bath chemistry and grain size is yet not well understood. Furthermore, grain size analysis is required for each unique electroplating tool, especially, if the grain size should be linked to diffusion parameters. If a dedicated tool such as electron backscatter diffraction (EBSD) is not available, this thesis recommends using conventional methods that involve calculation of grains manually (ASTM and liner intercept).

It is generally accepted that impurities may pin grain boundaries during post deposition annealing. Furthermore, the pinning is likely orientation-dependent, leading to abnormal grain growth. However, the existence of grain boundary pinning is debatable, since the model assumes that impurities would be attracted to a free surface that is not noticed in a research by M. Rizzolo et al. [160].

8.1.1 FIB

FIB was used for the grain revelation using the sample preparation process described in Section 7.2. The grains were manually counted and the data was analysed using the ASTM standard and linear intercept methods introduced in Section 5.1. Since the grains were counted manually, the error is assumed to be $+/-$ 1 grains for the ASTM and $+/-$ 0.5 grains for the linear intercept method. For the ASTM standard method, the amount of grains was manually calculated inside of 1-16 μm^2 areas depending on the size of the grains. The area has to be varied since the results would

not be reliable if a single grain would be larger than the analysed area. The area analysis was repeated five times per sample to get an average result. An example of the manual counting is shown in Figure 36. The twinned grains were not treated as separate grains and the partial grains inside the areas were taken into account. The actual ASTM grain size numbers were calculated using Equations 4 and 9. The numerical data is shown in Appendix C.

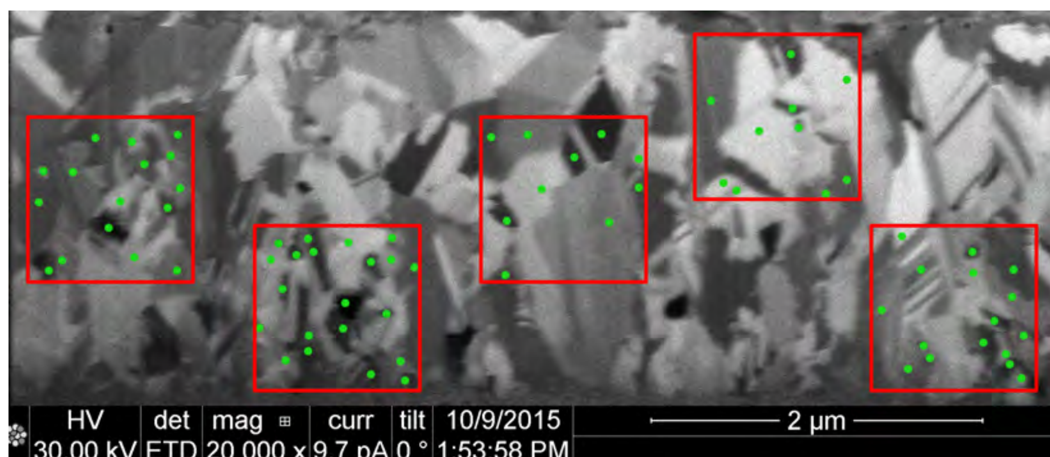

Figure 36: Five 1 μm^2 areas were drawn in the FIB grain contrast image and the grains are calculated manually. However, the twinned grains were not calculated as separate grains and the partial grains had to be taken into account.

The linear intercept method was used to confirm the results. Five lines were drawn in the grain contrast image and the amount of intersections was calculated manually. Since this method requires less interpretation than the ASTM method, the error was assumed to be +/- 0.5 grains per line. An example of the method is shown in Figure 37. It was discovered that the grains did not grow during the 150 °C annealing as shown in Figure 38. However, comparison required several measurements at different temperatures, thus all sample-types could not be compared. The only samples that had increased grain size were electroplated using a freshly made, semiconductor grade SPS solution. However, this data is not enough to prove the grain boundary pinning since the plot has only a few data points. The other observation is that the initial grain size is ~0.5 μm for all but the SPS+PEG samples. Furthermore, when the thickness of the SPS+PEG copper layer was increased to 10 μm, the average grain size was doubled to 2.2 μm. In fact, it is known that the average grain size increases when the film thickness is increased. Although that does not tell the reason for the behaviour of the SPS+PEG samples or the general lack of grain growth. The initial grain sizes are shown more accurately in Figure 39. All results were confirmed using the linear intercept method and the comparison is shown in Figure 39. To summarize, both grain size calculation techniques work well and the results are in the same order of magnitude. Moreover, if the error bars are taken into account, the results are practically same. Since the both techniques produce similar results, the linear intercept is more practical. The ASTM method requires more computing

and it is more prone to errors. The linear intercept method is simple, quick, and it produces comparable results.

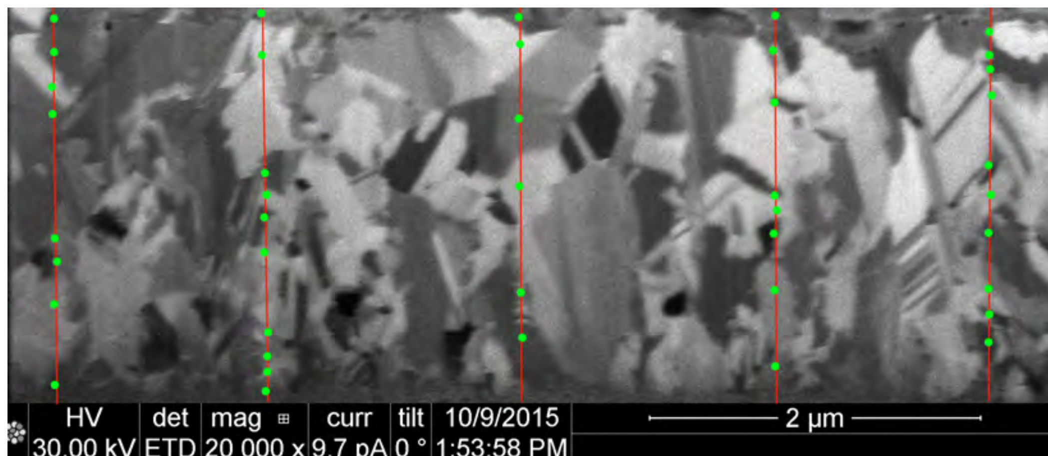

Figure 37: Five 2.2 μm lines are drawn in the FIB grain contrast image and the intercepting grains are calculated manually. Equation 11 is used to calculate the average grain size.

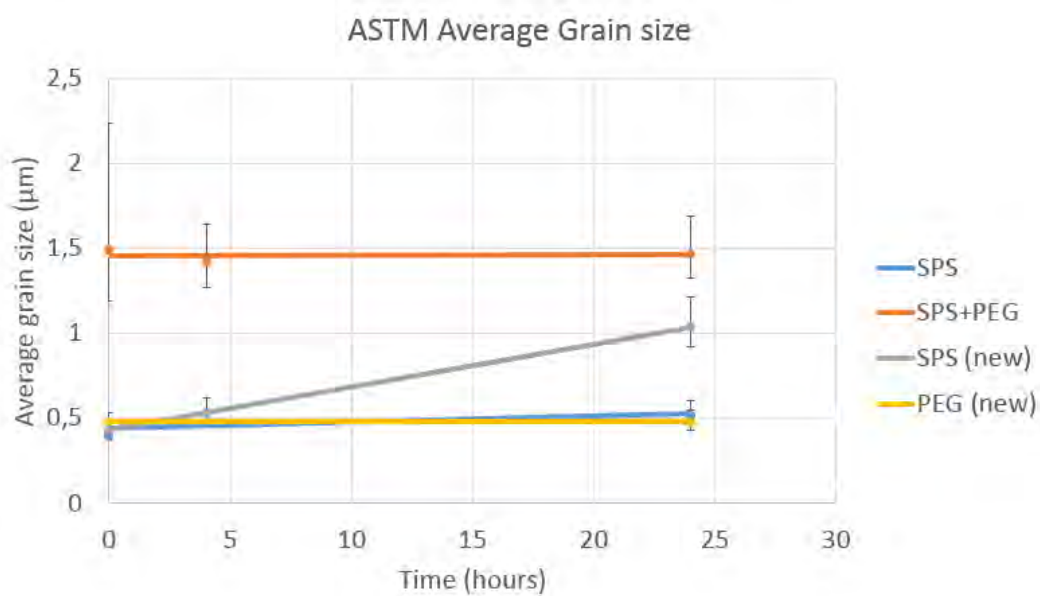

Figure 38: The only samples whose grain size increased when annealed at 150 °C were electroplated using the freshly made SPS electrolyte.

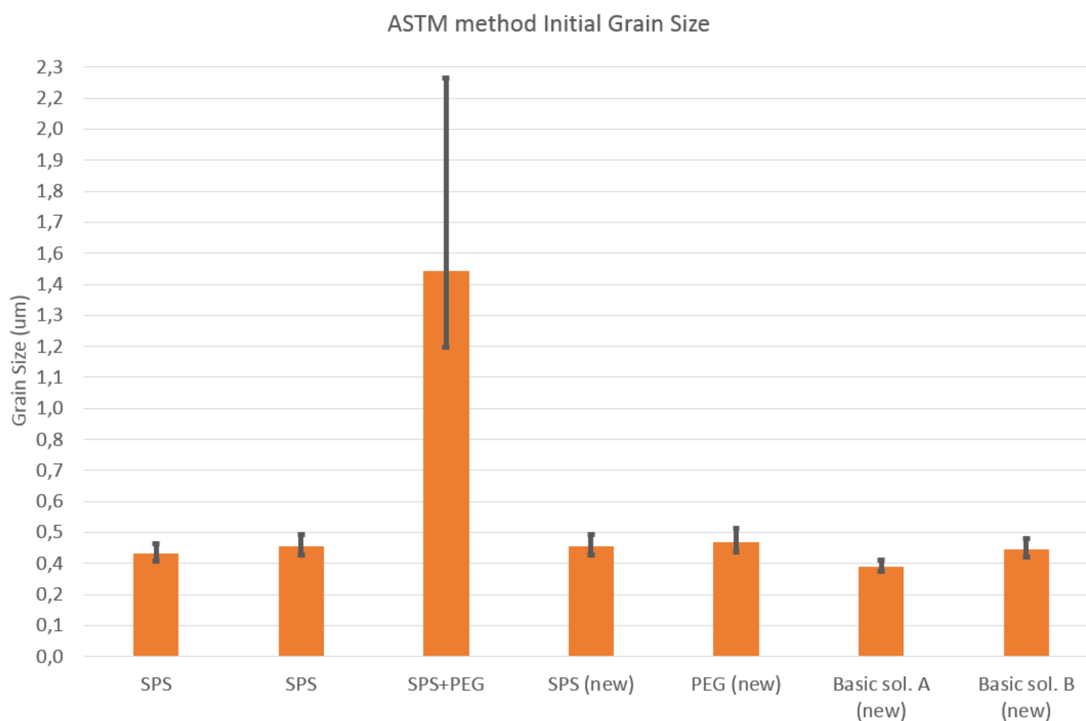

Figure 39: The initial grain size is ∼0.5 μm for all but the SPS-PEG samples. However, the samples were stored at room temperature for several weeks and that might have caused self-annealing.

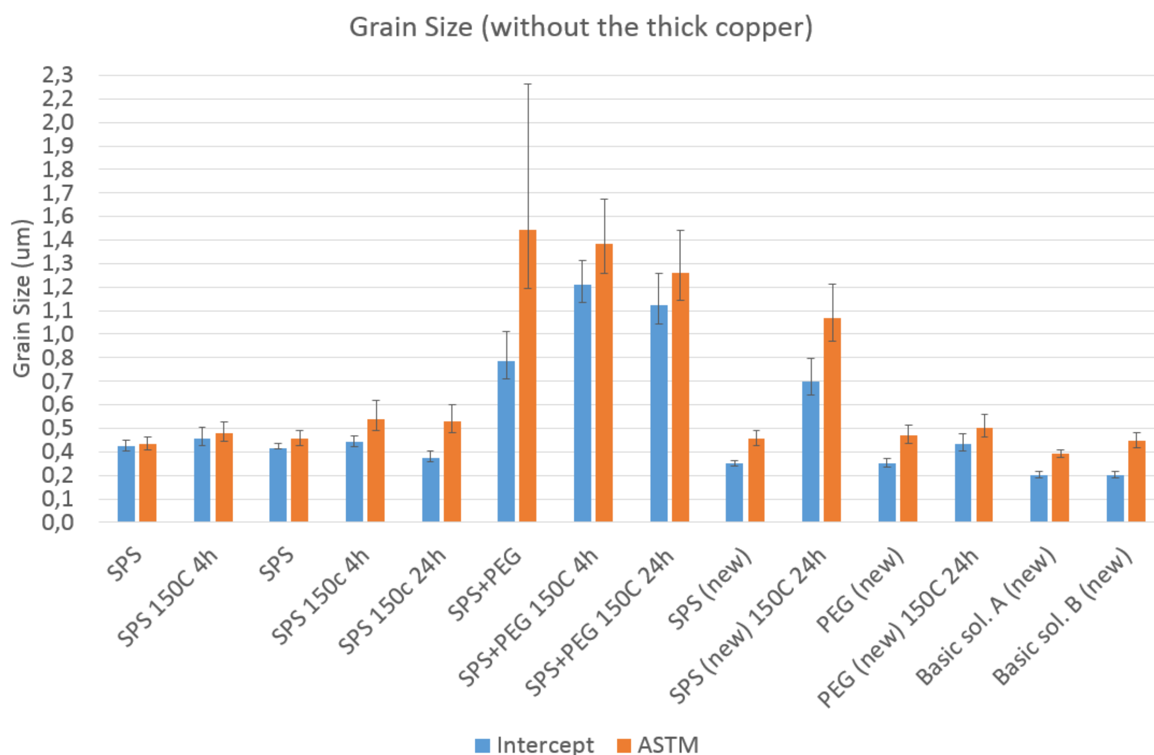

Figure 40: The results that are given by the linear interecept method and the ASTM method are comparable. The difference is in the range of 100 nm for most of the samples if the errorbars are taken into account.

Altogether, the reason for the lack of grain growth is unclear. It could be due to the grain boundary pinning but there is not enough evidence to support this conclusion. Another explanation could be the fast rate of self-annealing at room temperature since the samples were not imaged immediately after electroplating. Therefore, there is a need for further research. To evaluate the self-annealing, similar types of samples should be imaged immediately after the electroplating process. Furthermore, a series of analysis should be done for samples annealed at different temperatures to interpolate the activation energy of the grain growth. Since the approximation in Figure 23 was unrealistic, the interpolated activation energy should be compared to the literature to confirm why the approximation was not accurate.

FIB can be also used for general characterization. For instance, it was discovered that the electroplated copper and the tin layers varied greatly from the desired thickness. The copper thickness varied from 1.9 to 3.6 μm and the tin thickness from 1.2 to 1.6 μm. An example from the sample B-1 is shown in Figure 41. The copper thickness is 2.20 μm the tin thickness 1.40 μm. Since the sample B-1 was not annealed, the Cu_6Sn5 is $\sim$0.1 μm thick and the average void diameter $\sim$50 nm. Additionally, Figure 41 shows particles that possibly have eutectic composition. Binary Ga-Sn phase diagram in Figure 42 [161] shows an eutectic point near the Ga-rich end. The gallium-rich areas that contain tin, such as surfaces and borders, might have that eutectic composition. However, the eutectic microstructure is not observed in 41.

the gallium-rich areas that contain tin, such as surfaces and borders, might have an eutectic composition but the structure is not seen.

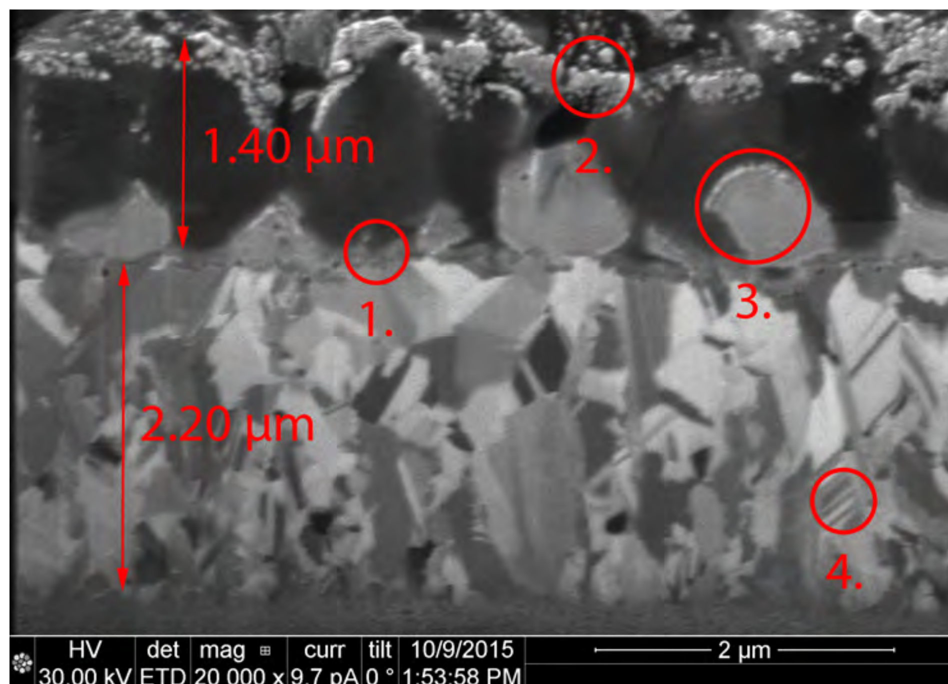

Figure 41: FIB grain contrast image of the sample B-1. (1) Cu_6Sn5 thickness is $\sim$0.1 μm (2) Eutectic SnGa (3) Unidentified grains that might be eutectic SnGa (4) Twinned copper grains

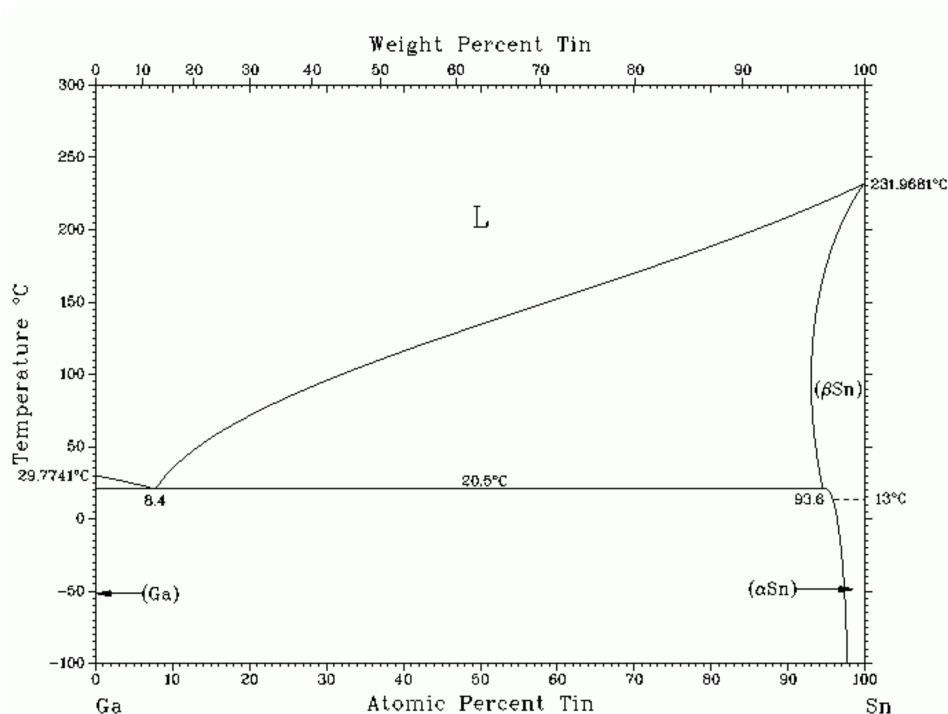

Figure 42: A binary phase diagram of Sn-Ga system. [161]

Figure 43 shows the B-2 sample after 4 hours of annealing. The combined IMC thickness has grown from ~0.1 μm to ~0.6 μm and average void size from ~50 nm to ~100 nm. The voids are clearly visible and they are located at the Cu/Cu_3Sn interface. Furthermore, some of the tin have been consumed and its thickness has been reduced to ~0.5 μm. However, the combined thickness of the Sn and IMC is less than that of the sample B-1. That is due to the Sn electroplating that produces a rough surface with varying thickness. The major disadvantage of the FIB polishing is the surface damage. As seen in Figure 43, the Sn layer is sensitive to the gallium ion-induced damage. Moreover, copper should be less sensitive than tin, but it was discovered that some of the copper grains changed color during the polishing process. The same phenomenon happened with almost all samples. First, it was assumed to be only a defect, but later it was noticed that the (110) oriented copper grains tend to form a Cu_3Ga phase when bombarded by the gallium ions [70]. Furthermore, the contrast is very high since the Cu_3Ga phase has a lower sputtering rate compared to the copper. It is interesting that FIB can be used to find grain orientations. However, there is not yet applications for this specific property of the copper. The third observation is the grain size distribution difference. For most of the samples, the grain size decreased near the seed layer and the grain size increases when getting further away from the seed layer. That is probably due to the seed layer since the seed layer has a strong effect on the copper grain size and orientation near the seed layer. As the copper grows thicker, the seed layer effect is decreased and the copper can grow "freely".

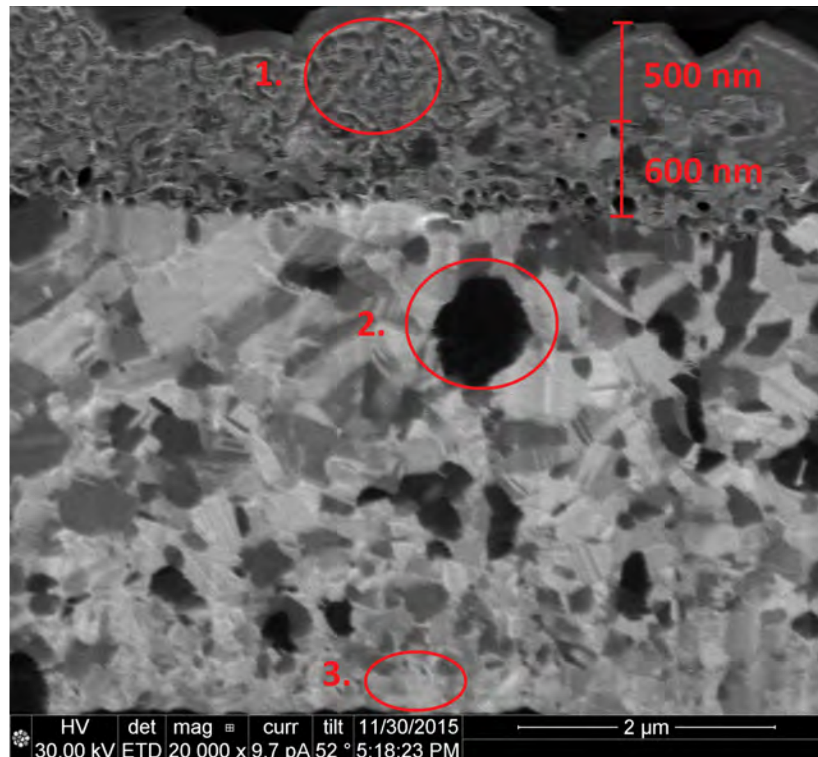

Figure 43: The B-2 sample was annealed for 4 hours. 1. The Sn layer is easily damaged by the gallium ion beam 2. Possible Cu_3Ga phase 3. The grain size is decreased near the seed layer.

Since Sn is sensitive to the gallium ions, the grain structure is not usually visible. However, if the sample preparation process is successful, Sn grains can be visible as shown in Figure 44. It can be observed that the Sn grains are rather large compared to the Sn layer thickness. Usually, the IMCs have minuscule grain sizes and the grains are not visible in the FIB grain contrast images. However, the grain size in the IMCs depends on the grain size of the copper. Since PEG+SPS samples had a large initial grain size, the grains in the Cu_3Sn are visible in Figure 44.

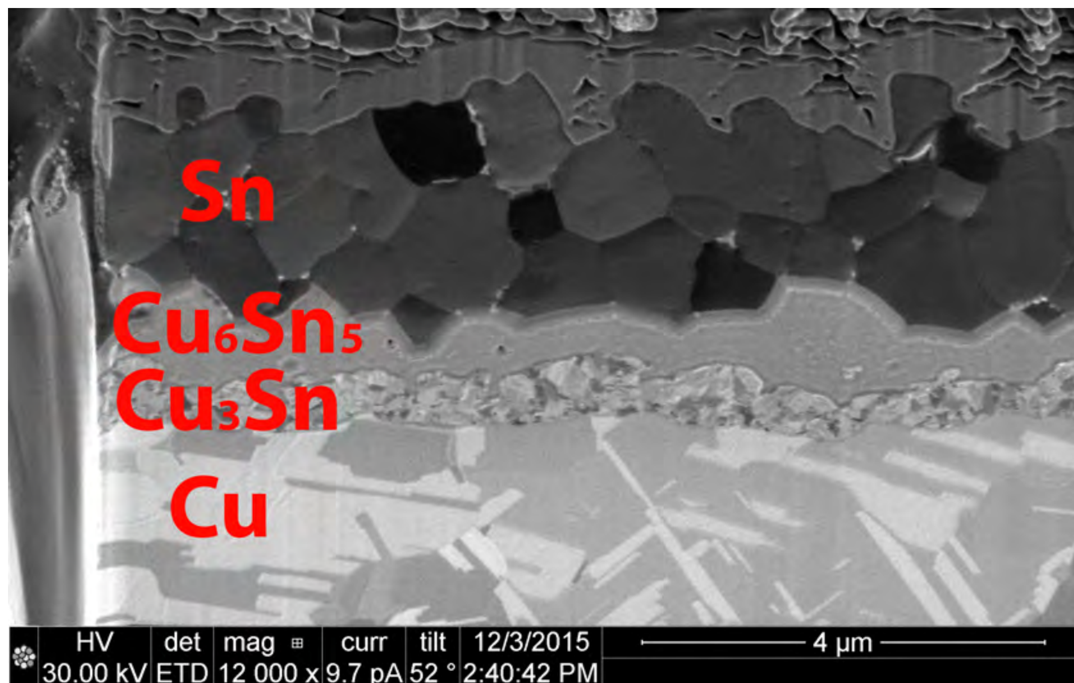

Figure 44: A FIB grain contrast image of the sample B-5. If the polishing process is successful, the Sn grains can be visible. Furthermore, if the initial grain size is large, the grains in Cu_3Sn are also visible.

8.1.2 SEM and TEM

The secondary electron (SE) pictures taken by FIB do not exhibit a strong grain contrast. A typical example is shown in Figure 45. Nevertheless, the capability of back-scattered electrons (BSE) was tested using FESEM since it was assumed that the BSE-detector would reveal higher grain contrast than the SE-detector of the FIB [65]. The sample B-5 was chosen for the testing since the polishing had been done exceptionally well. The polishing process was similar to the previous FIB grain study, but the sample was polished in a 7° angle (Section 7.2). It was discovered that the grain contrast of the BSE-detector was not great as shown in Figure 46. The grain boundaries are almost invisible and the image is blurry. However, it was observed that the SE pictures taken by FESEM were sharp and high resolution. Figure 47 is taken from the same sample and it shows an SE picture (FESEM) taken from the interfaces. The copper grains are visible at the bottom part, but the most interesting part is the visibility of the IMC grains. The Cu_3Sn has too small grains to be actually measured but the structure of the Cu_6Sn5 is interesting. The objects inside the Cu_6Sn5 are pillar-like and it is unclear if those were grains or defects caused by the gallium ion polishing. The second observation is the preferential milling which is shown as an artificial layer between the Sn and Cu_6Sn5.

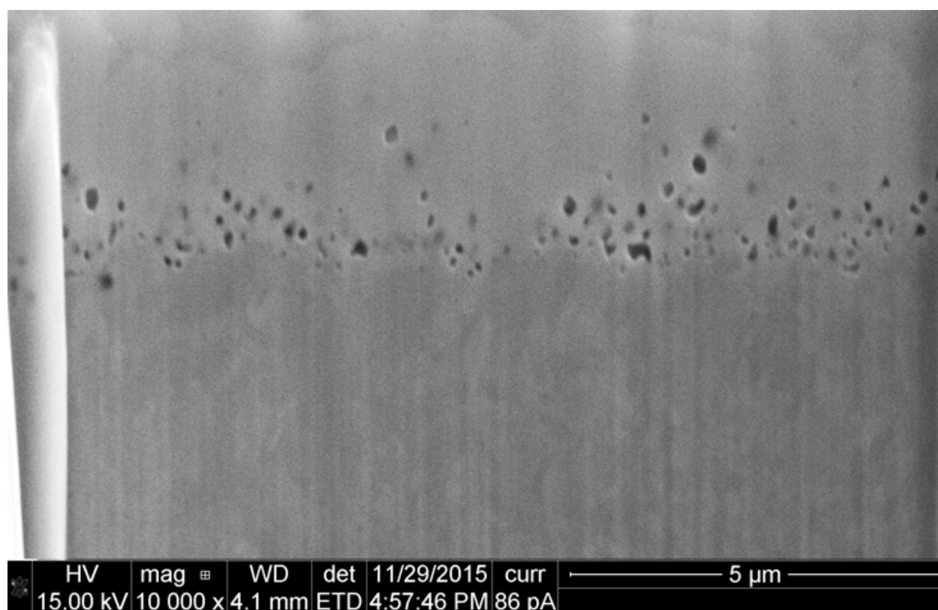

Figure 45: The SE images taken by the dual beam system do not usually reveal a strong grain contrast. However, the SE detector is useful to check topographical properties, such as void sizes.

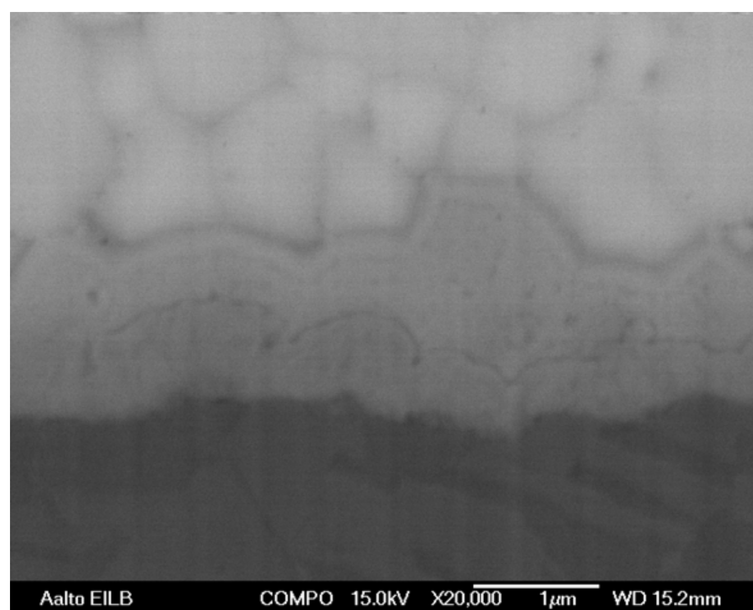

Figure 46: SEM-BSE micrograph shows that the BSE-detector was not better than SE-detector in the dual beam FIB system. The image is blurry and the grain boundaries are almost invisible.

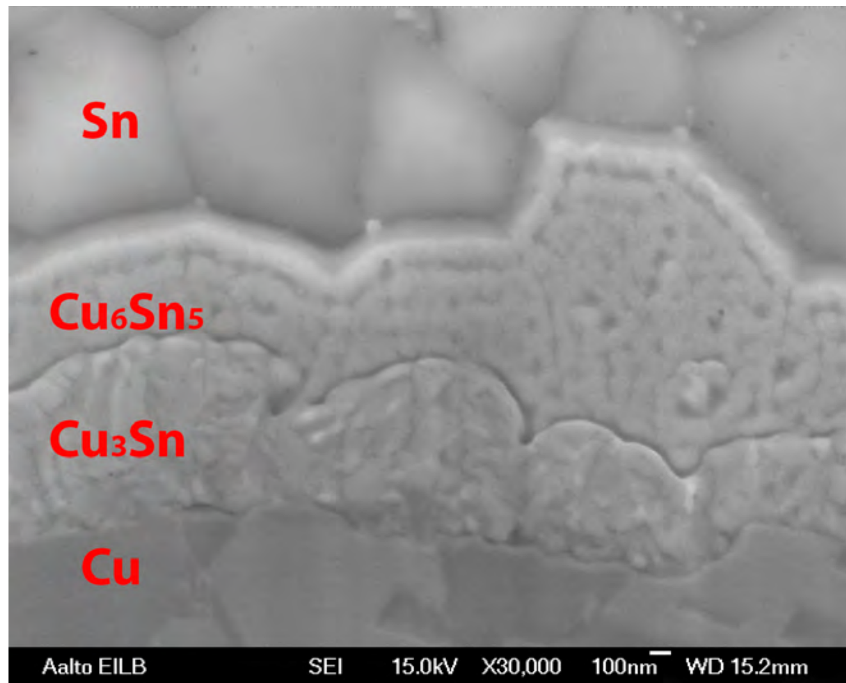

Figure 47: The SE images taken by a dedicated SEM were sharp and high resolution. The grains of the IMCs could be seen. However, it is unclear are the objects in the Cu_6Sn5 grains or defects from the polishing.

Before the STEM-EDX analysis, TEM-BF and STEM-HAADF pictures were taken from the samples A-1 and A-2 . (S)TEM analysis of the Kirkendall voids was done at Fraunhofer IMWS. The general view pictures were taken by TEM-BF and the lamellas are shown in Figure 48 and Figure 49. However, the overviews do not reveal more than the FIB-analysis. The large voids between the Sn and IMCs are defects from the polishing process. The copper grains are visible in both figures, but the grain boundaries are not easy to identify. Despite that, the Kirkendall voids are visible in Figure 49. Most of the voids are located at the interface between the Cu and Cu_3Sn

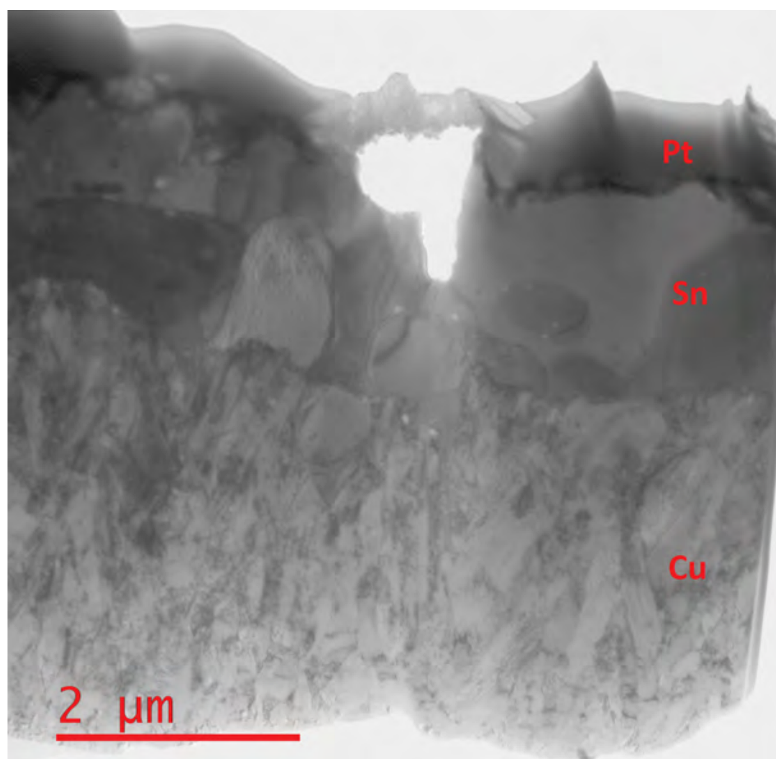

Figure 48: An overview of the sample SPS (A-1) imaged by TEM-BF.

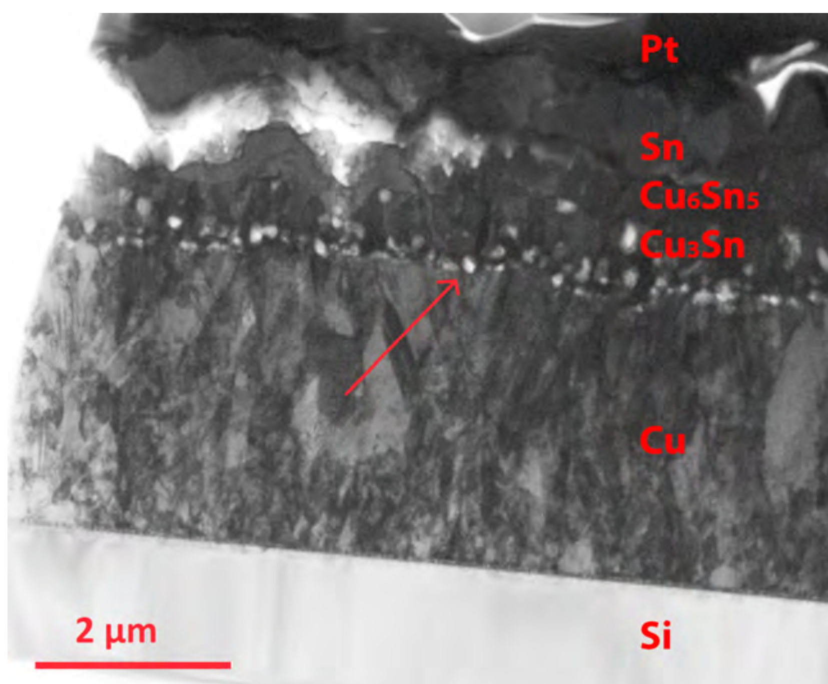

Figure 49: An overview of the sample SPS annealed (A-2) imaged by TEM-BF. The voids are seen between the Cu and Cu_3Sn,

To evaluate the samples further, STEM-HAADF was used with a higher magnifi-

cation. STEM-HAADF picture of the Cu-IMC interface in A-1 in Figure 50 reveals that some of the voids are closed and some of the voids are through-voids. The size of the closed voids is less than 50 nm and the through-voids are from 50 to 100 nm. Therefore, the sample is probably thinner than expected since there are no closed voids over 50 nm diameter. The voids are mostly located at the interface and IMC but some of the voids are partially on the copper side.

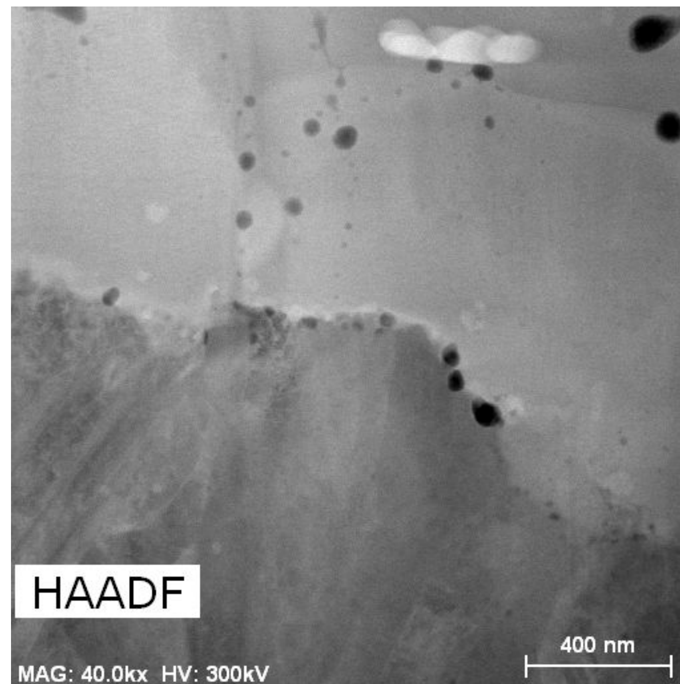

Figure 50: Some of the voids are through-voids and some of the voids are closed. The voids are not restricted to the IMC side.

In the HAADF image of the annealed sample (A-2) (Figure 51), it can been seen that the size of the through-voids has been increased to 100-200 nm and there exist voids that have a diameter of 200 nm. Therefore, the thinning process of the sample A-2 was more successful since the target thickness was reached. Furthermore, the number of voids is higher, but similar to the sample A-1, the voids tend to reach to the copper side.

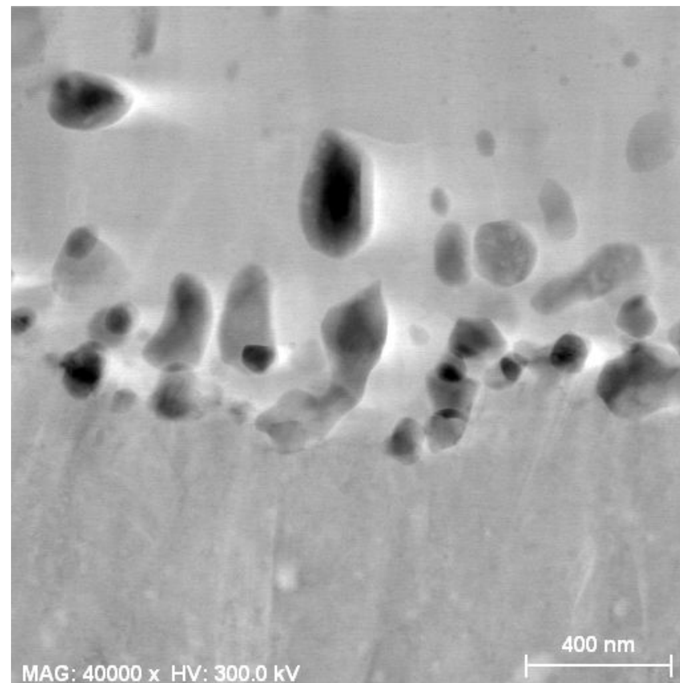

Figure 51: Similar to the non-annealed sample, some of the voids are through-voids are some of them closed. The amount of voiding is high.

8.1.3 GHz-SAM

GHz-SAM analysis of the Kirkendall voids was done at Fraunhofer IMWS. The sample type was SPS (B-3) but it was annealed for an additional 48 hours and the combined thickness of the deposited metals was in the range of GHz-SAM penetration depth. However, the high roughness of the Sn layer made the imaging from the top side challenging as seen in Figure 52. Furthermore, the Sn surface was polished but it did not decrease the RMS roughness enough. The reason for the indistinct pictures is the inability of SAM to detect defects that are smaller than the RMS roughness of the specimen surface.

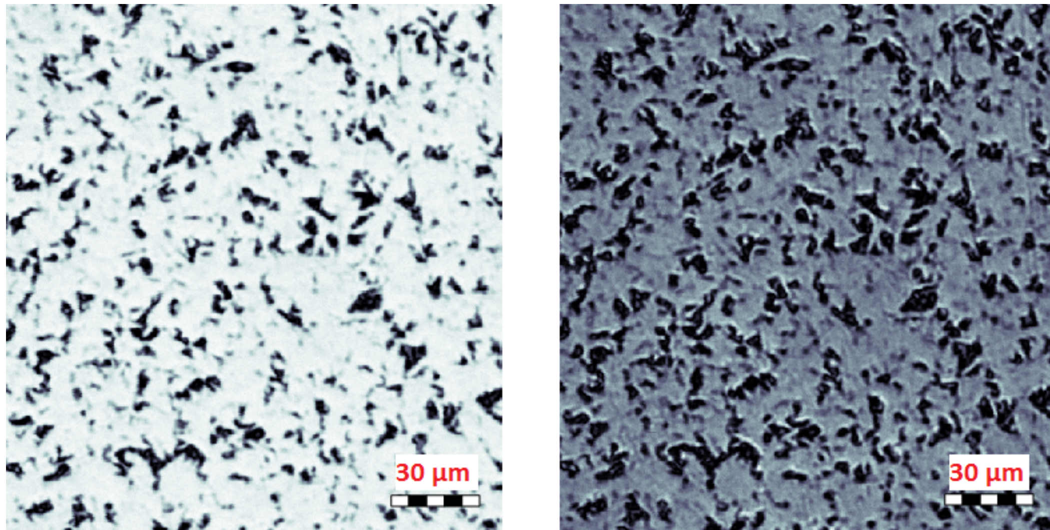

Figure 52: The Sn top layer was too rough for GHz-SAM imaging. The left picture is focused on the surface and the right picture inside the bulk. Since the geometries from the surface are copied to the bulk picture, it is evident that the surface roughness is too high.

However, even the top side pictures might give some evidence about the Kirkendall voids. By combining the two pictures from Figure 52, the geometries that were not found on the surface could be colored as shown in Figure 53. The yellow-green parts represent the defects found both from the surface and the bulk, whereas the red parts represent the defects found only from the bulk. The red defects are considerably smaller than the surface defects. However, the interpretation of this kind of approach is challenging since the red-colored defects could be actually from the surface that are not visible due to the larger surface-defects or they might present defects such as Kirkendall voids.

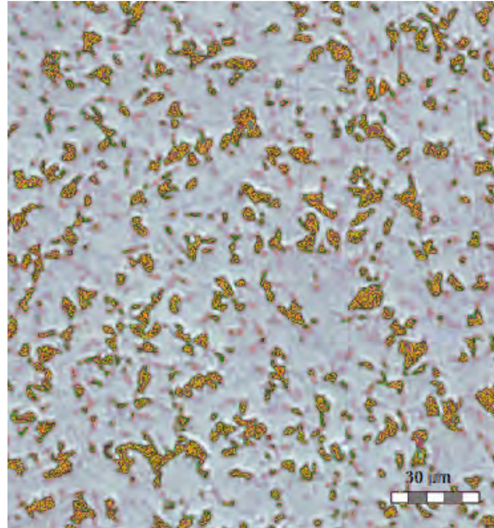

Figure 53: By combining the surface and bulk pictures, it can be seen that the bulk picture shows more details than the surface picture. The yellow-green parts are visible on both the surface and the bulk, but the red parts are visible only in the bulk picture.

Eventually, it was discovered that the adhesion between silicon and the deposited layers was low and the stack of films could be peeled off from the silicon. Usually, a bad adhesion is a nuisance, but in this case, the interesting part of the sample could be peeled off and the copper could be imaged from the smooth backside. The most probable explanation for the low adhesion is the low quality of Cr adhesion barrier or the existence of a native silicon oxide layer that was not removed prior the depositions.

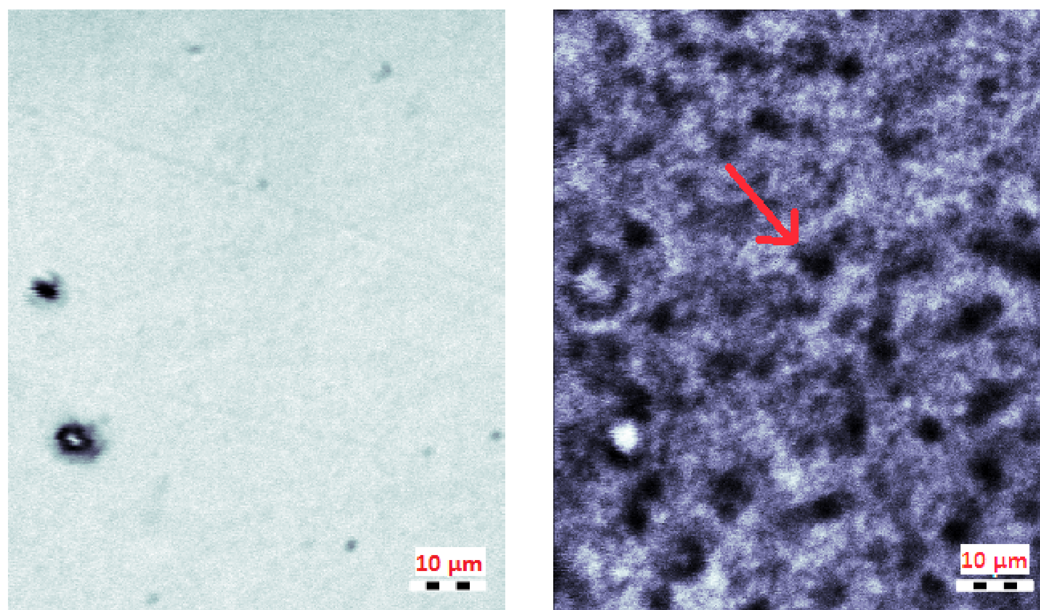

Figure 54: The problem from the surface roughness could be bypassed by peeling the sample and imaging from the backside. The left picture shows the surface focus and the right picture the bulk focus. As can be seen, the surface contains only a few defects and the bulk contains a significant amount of spherical defects whose size is apparently in the range of 2-4 μm

Figure 54 shows the GHz-SAM images from the backside of the peeled samples. It can be seen that there is only a few defects on the surface and the bulk picture clearly shows spherical defects. However, the size of the defects is on a different magnitude that is usually linked to the Kirkendall voids. The reason is probably the acoustical wave spreading. GHz-SAM can show air-filled defects below its resolution of 1 μm since the reflection percent of the air is almost 100. However, the scale of the defects is incorrect due to the spreading of the acoustical waves. Furthermore, based on the cross-sections reviewed in Sections 8.1.1 and 8.1.2, the diameter of the Kirkendall voids should be less than 500 nm. In that sense, this type of imaging is not a reliable source to evaluate the size of the Kirkendall voids, but a tool to evaluate the distribution of the voids. Altogether, this is the first time that Kirkendall voids (assumed) have been probed by GHz-SAM. The technique is promising but more research is required to confirm the results. Furthermore, if the sample will have a better adhesion, the peeling technique cannot be used. In that case, some other technique is required to reduce the surface roughness, such as backside etching or CMP.

8.2 Impurity Analysis

The impurity analysis is the second main focus of this thesis. As described before, the relation between electroplating bath chemistry and Kirkendall voiding is complicated. Therefore, there was a need to compare impurity analysis tools to specify the most suitable techniques for the micro-connects. The selected techniques were SIMS, AES

and ERDA. SIMS was used in preliminary testing, but it turned out that the high surface roughness combined with multiple phases produced too large errors in depth profiles. Therefore, STEM-EDX was chosen as a primary technique to characterize impurities near and inside the Kirkendall voids.

The target thickness for the STEM-sample thinning was 200 nm which is thicker than normally recommended. The reason is that it was assumed that volatile impurities will dissipate from the voids if the sample is too thin. The investigated impurities were C, Cl, Ga, N, O, and S. However, gallium is not an impurity from the electroplating, but a defect from the thinning process. The amount of gallium can be used to evaluate the success of FIB-thinning and to evaluate the thickness of the sample since the gallium content should be limited to the uppermost layer of the specimen.

8.2.1 STEM-EDX

STEM-EDX analysis of the Kirkendall voids was done at Fraunhofer IMWS. The investigated samples were A-1(reference) and A-2(annealed) that were thinned using a FIB (Section 7.3). Before the investigations, the samples were cleaned by an oxygen plasma. The phases in the non-annealed A-1 sample were identified using the Cu and Sn elemental maps shown in Figure 55. The IMC can be identified as Cu_6Sn5 since it tends to grow event at the room temperature. However, there might be some Cu_3Sn between Cu and Cu_6Sn5. Surprisingly, the combined IMC thickness was $\sim$0.6 μm even without annealing. Moreover, impurities that are usually related to the Kirkendall voiding, were not detected. As shown in Figure 56, the only impurities found were Ga and N. The high gallium content might be related to an unsuccessful thinning process since too thin sample contains relatively more gallium than a thicker sample. The other reason could be unsuccessful cleaning steps during the FIB-thinning since those last steps should remove most of the gallium-implanted outer layer. It can be seen that the nitrogen content is limited only to the areas that contain tin. However, the reason for nitrogen content is not clear. It might be due to the commercial tin electroplating solution, due to the limited energy resolution of EDX for lighter elements or due to absorption from the atmosphere. However, it is unknown whether nitrogen is important regarding the Kirkendall voiding. However, Figure 56 shows that the voids do not contain nitrogen. The rest of the chemical maps regarding sample A-1 can be found from Appendix B.

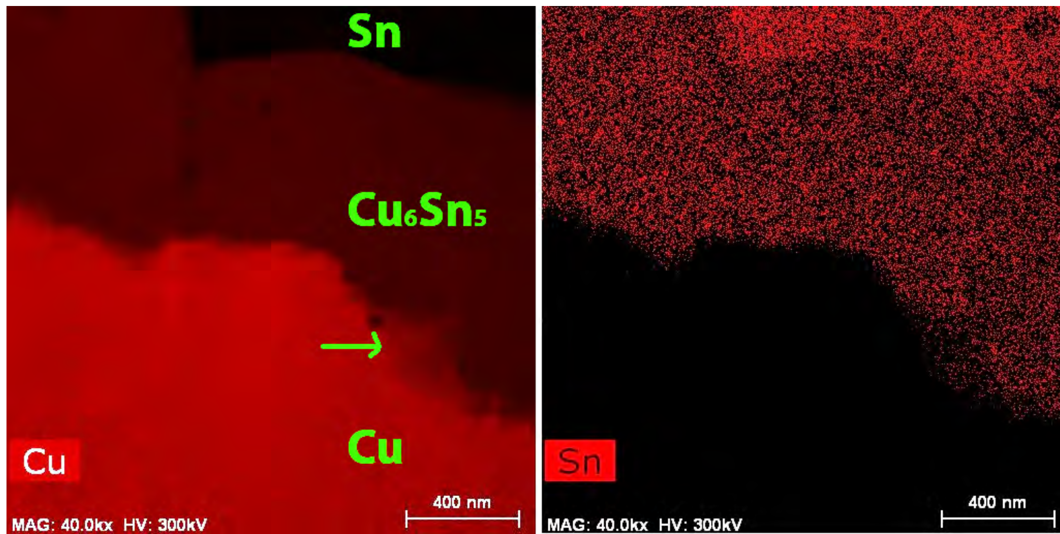

Figure 55: The phases could be identified as Cu, Cu_6Sn5, and Sn by comparing the elemental maps. The arrow shows area that might be Cu_3Sn. The combined IMC thickness is ∼0.6 μm.

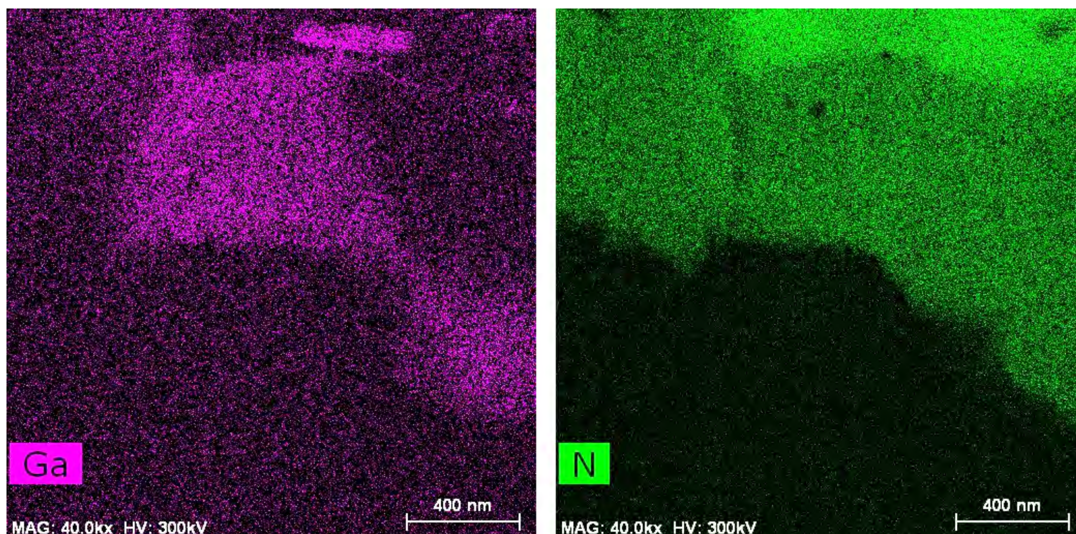

Figure 56: The only impurities found in the sample A-1 were Ga and N. The gallium is introduced during the FIB-thinning but the origin of the nitrogen is unclear. However, the voids seen in the nitrogen map do not contain nitrogen.

The results from the sample A-2 (annealed) were clearly different compared to the sample A-1. The gallium content has decreased, but the nitrogen content is same which shown in Figure 57. The reason for the different gallium content is probably due to better thinning-process or the sample is thicker than the sample A-1. The hight amount of voids can be seen even in the chemical maps, even though, the sample does not contain S which is typically related to the Kirkendall voiding. Similar to the sample A-1, the phases were identified using the Cu and Sn chemical maps that are shown in Figure 58.

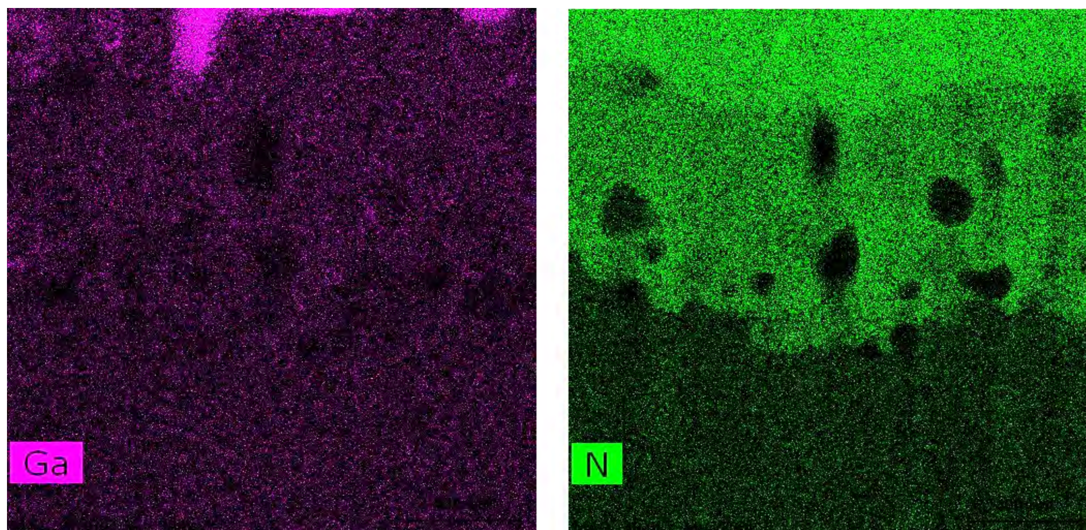

Figure 57: The sample A-2 contained less gallium than the sample A-1, but the amount of nitrogen was similar.

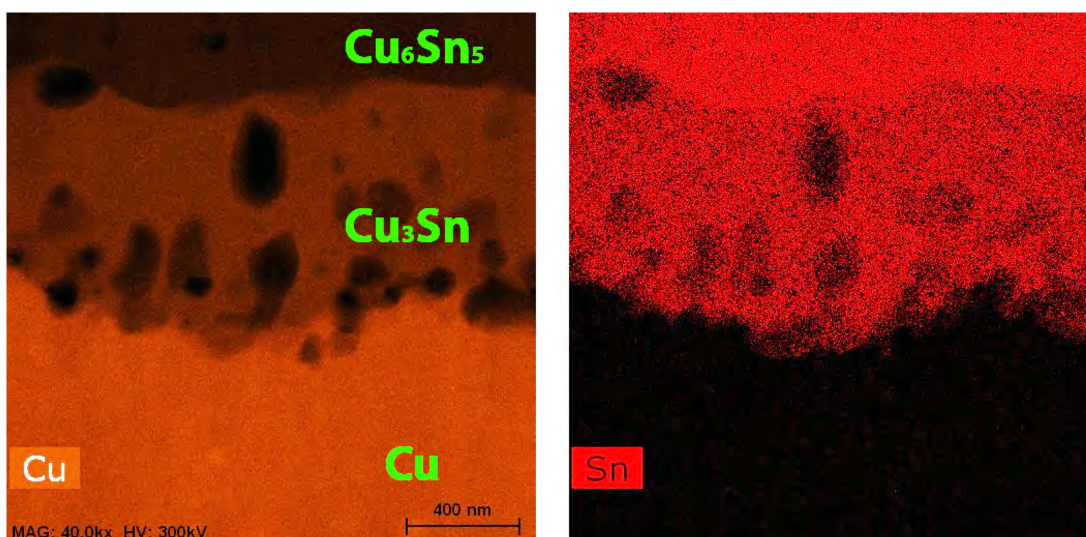

Figure 58: The voids are located in the Cu_3Sn that has grown during the annealing.

The most interesting result of this thesis is shown in Figure 59. The Kirkendall voids in the sample A-2 contained a significant amount of Cl and O. This is the first time that impurities have been directly measured inside the Kirkendall voids and, in addition, the found impurities are not usually associated with the Kirkendall voiding.

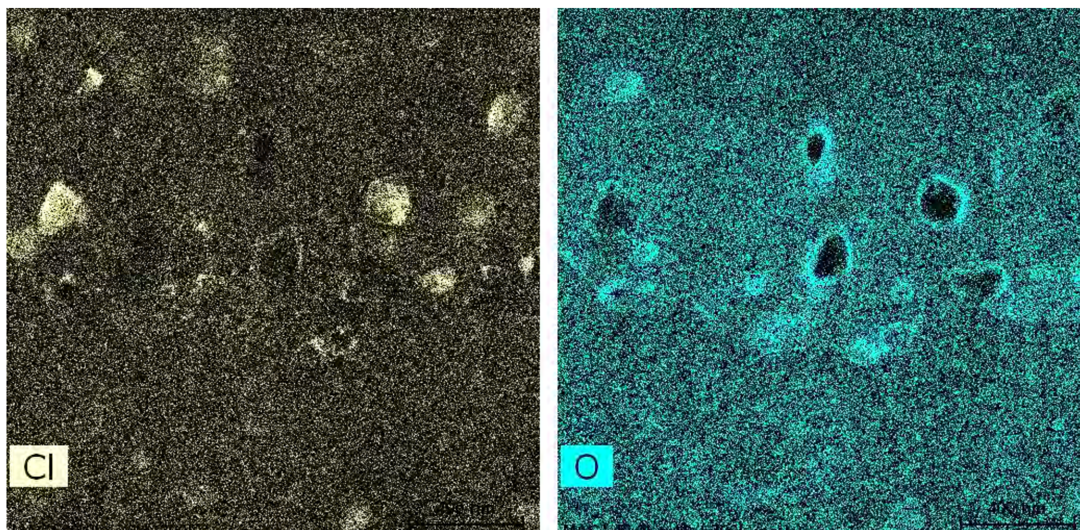

Figure 59: The Kirkendall voids in the sample A-2 contained chlorine and oxygen that are not usually associated with the Kirkendall voiding.

However, all voids do not seem to contain chlorine. By combining the Cl, Cu, and O maps in Figure 58, it was discovered that the through-voids do not contain chlorine and the oxygen exists only at the edges of these voids. That is supportive evidence for the hypothesis of impurity dissipation in too thin (S)TEM-samples. Altogether, it is unclear that has the chlorine segregated during the annealing or would the sample A-1 contained chlorine if it would have been thinner. Secondly, the origin of the oxygen is unknown. One explanation could be that the oxygen plasma cleaning have had an effect on the sample. However, the oxygen deficiency in the sample A-1 does not support that conclusion since the pretreatment for the both samples was similar. The rest of the chemical maps can be found from Appendix B.

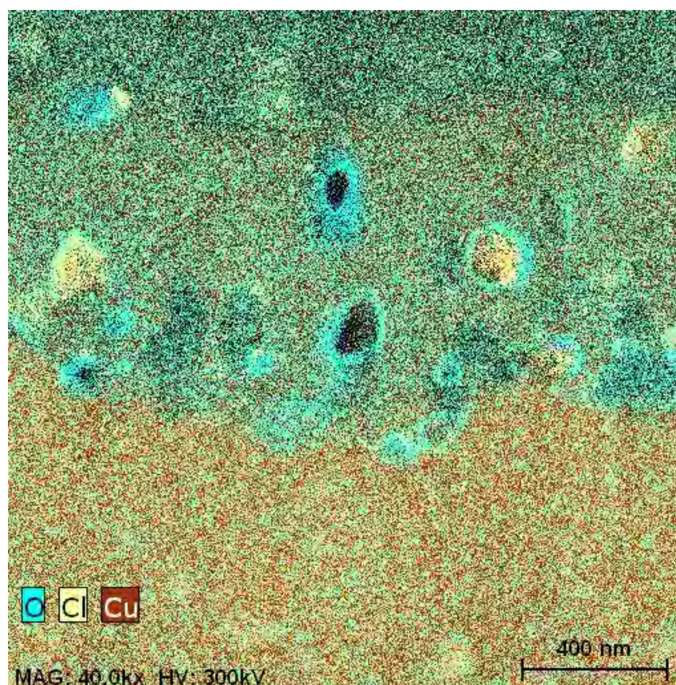

Figure 60: By combining the Cl, O, and Cu maps, it could be discovered that the exposed voids did not contain chlorine. Furthermore, the exposed voids had oxygen only near the edges.

Altogether, the chlorine content in the Kirkendall voids was surprising. There exists only a few mentions of chlorine content in Cu_3Sn [16, 162], but it has not been associated to the Kirkendall voiding. Furthermore, it has been a common belief that the chloride ions should have high local stability and the literature does not even consider the negative effect of the chlorine ions [20, 163]. It is known that the combination of PEG and Cl forms a passivation layer on top of the electroplated copper but the combination of SPS and Cl should not have any special effect [16, 164]. The evidence presented in this thesis does not support the theory that the root cause for the Kirkendall voiding is the high sulphur content since sulphur could not be found at all even though the level of voiding was high.

However, the results should be approached with caution. The size of the analysed area is small and the impurity situation could be different at a different location. Moreover, the results were acquired only from two samples since the (S)TEM sample preparation and imaging is time-consuming. Additionally, the impurity content was artificially high since the used electroplating solution was not freshly made. The results should be confirmed using a complimentary technique such as SIMS or AES since (S)TEM-EDX is not fully quantitative for lighter elements.

9 Conclusions

The objectives of this thesis were to compare and select appropriate characterization methods for Cu-Sn micro-connects. The characterization was especially focused on impurities and microstructure of electroplated Cu-Sn. The main criterion for choosing the impurity analysis techniques was the ability to characterize solid samples. However, it is not easy to choose techniques based only on the specifications since the tools might have non-advertised problems, such as sensitivity to surface roughness. Based on the literature review, this thesis recommends using SIMS, AES, or ERDA for micro-connect impurity analysis since the listed techniques fulfill the demand for high lateral resolution, depth profiling, and solid sample characterization. From the reviewed impurity analysis tools, RBS, ERDA, and XPS have not been much used in the research fields related to micro-connects. Therefore, they might have novelty value in future research.

GHz-SAM was the most novel tool from the reviewed structural characterization methods. The tool was utilized in the experimental section since it has never been used before for Kirkendall void characterization. The void analysis was partially successful, but it seems that the lateral resolution of the tool is not high enough. However, GHz-SAM could be possibly used to study the distribution of the voids.

The grain size analysis was concluded by applying the ASTM standard test E112 to FIB-polished samples. The ASTM method is usually recommended for grains that are visible with an optical microscope, but this thesis showed that the method can be applied to sub-1 μm grains. It was discovered that the grain size did not increase at 150 °C for most of the samples. The reason cannot be identified without further research since the grain boundaries can be pinned due to the impurities or the samples had self-annealed before the analysis.

This thesis gave a profound insight of how to prepare grain contrast samples and TEM lamellas using a FIB. Moreover, most of the sample preparation limitations are described and practical advice reported. It was discovered that FIB alone is a great tool for characterization of Kirkendall voids and other defects. In addition, it seems that FESEM with an SE-detector is a suitable tool for grain contrast imaging. Additionally, it was observed that BSE-SEM imaging does not provide any additional information to FIB grain analysis.

SIMS was used in the preliminary tests for the impurity analysis, but it turned out that the tool was too sensitive to surface roughness and preferential sputtering. Therefore, STEM-EDX was chosen as a primary technique to characterize impurities inside Kirkendall voids due to the high availability of the tool.

The novelty of the TEM-sample preparation was in the chosen lamella thickness which was greater than normally recommended. The reason for the unusual thickness was the hypothesis that impurities can dissipate from overly thin lamella. The assumption was correct, and for the first time, the impurities were measured directly inside the Kirkendall voids. Furthermore, in previous studies, sulphur has been identified as a common impurity that might cause Kirkendall voiding. However, this thesis did not find any sulphur in or near the Kirkendall voids. The only impurities found were, to the knowledge of the author, chlorine, oxygen and nitrogen. There

exist studies that consider chlorine content in Cu_3Sn, but it has never been linked before to the Kirkendall voiding.

However, it should be remembered that the impurity content may vary due to chosen characterization method, surface contaminants, different electroplating additives, different room temperature exposure times, and varying copper thickness. If research in the future supports the findings of this thesis, it would be important to measure similar types of samples using complementary techniques, such as SIMS or AES. Finally, it would be interesting to evaluate the chemical state of the chlorine to observe whether it has bonded with copper or other impurities.

Despite what has been reported to be the root cause(s) for the Kirkendall voiding, the issue requires further investigation. This thesis suggests that there might be a different driving force for the voiding than what has been assumed before. Sulphur, that has been the main suspect before, might not be the only decisive impurity. Therefore, this thesis recommends continuing the research of less studied impurities, such as chlorine, by using the selected impurity analysis techniques.

References

[1] K.-E. Elers, *Copper Diffusion Barrier Deposition on Integrated Circuit Devices by Atomic Layer Deposition Technique.* PhD thesis, Helsingin Yliopisto, 2008.

[2] Y. Lamy, J. Colonna, G. Simon, P. Leduc, S. Cheramy, and C. Laviron, "Which interconnects for which 3D applications? status and perspectives," in *3D Systems Integration Conference (3DIC), 2013 IEEE International*, pp. 1–6, IEEE, 2013.

[3] J. Colonna, R. Segaud, F. Marion, M. Volpert, A. Garnier, L. Di Cioccio, Y. Beillard, S. Mermoz, F. De Crécy, C. Laviron, *et al.*, "Towards alternative technologies for fine pitch interconnects," in *Electronic Components and Technology Conference (ECTC), 2013 IEEE 63rd*, pp. 872–878, IEEE, 2013.

[4] A. Rautiainen, H. Xu, E. Österlund, J. Li, V. Vuorinen, and M. Paulasto-Kröckel, "Microstructural characterization and mechanical performance of wafer-level SLID bonded Au-Sn and Cu-Sn seal rings for MEMS encapsulation," *J. Electron. Mater.*, vol. 44, no. 11, pp. 4533–4548, 2015.

[5] H. Li, R. An, C. Wang, Y. Tian, and Z. Jiang, "Effect of Cu grain size on the voiding propensity at the interface of SnAgCu/Cu solder joints," *Mater. Lett.*, vol. 144, pp. 97–99, 2015.

[6] G. Ross, "Void formation in Cu-Sn micro-connects," Master's thesis, Aalto University, https://aaltodoc.aalto.fi/handle/123456789/17699, 2015.

[7] G. Ross, V. Vuorinen, and M. Paulasto-Krockel, "Void formation in Cu-Sn micro-connects," in *Electronic Components and Technology Conference (ECTC), 2015 IEEE 65th*, pp. 2193–2199, IEEE, 2015.

[8] B. Wu, A. Kumar, and S. Ramaswami, *3D IC stacking technology.* McGraw-Hill Professional, 1st ed., 2011.

[9] S. Bansal, "3D ICs with TSVs: Design challenges and requirements." `http://www.soccentral.com/results.asp?CatID=488&EntryID=39652`. Accessed: 2015-11-20.

[10] D. Vye, "The dawn of nano-scale system-on-package," *Microwave Journal*, vol. 52, p. 24, 2009.

[11] M. G. Farooq and S. S. Iyer, "3D integration review," *Science China Information Sciences*, vol. 54, no. 5, pp. 1012–1025, 2011.

[12] C.-T. Ko and K.-N. Chen, "Reliability of key technologies in 3D integration," *Microelectronics Reliability*, vol. 53, no. 1, pp. 7–16, 2013.

[13] K. Tu, H.-Y. Hsiao, and C. Chen, "Transition from flip chip solder joint to 3D ic microbump: Its effect on microstructure anisotropy," *Microelectronics Reliability*, vol. 53, no. 1, pp. 2–6, 2013.

[14] H. Manhaeve, H. Manhaeve, and H. Manhaeve, "TSV BIST: An innovative method for 2.5D/3D IC interconnection integrity monitoring," tech. rep., Ridgetop Group Inc., 2013.

[15] S. Kim and J. Yu, "Heat-treatment to suppress the formation of kirkendall voids in Sn-3.5 Ag/Cu solder joints," *Mater. Lett.*, vol. 106, pp. 75–78, 2013.

[16] L. Yin and P. Borgesen, "On the root cause of kirkendall voiding in Cu3Sn," *J. Mater. Res.*, vol. 26, no. 03, pp. 455–466, 2011.

[17] Y. Jung and J. Yu, "Electromigration induced kirkendall void growth in Sn-3.5 Ag/Cu solder joints," *J. Appl. Phys.*, vol. 115, no. 8, p. 083708, 2014.

[18] J. Kim and J. Yu, "Effects of residual impurities in electroplated Cu on the kirkendall void formation during soldering," *Appl. Phys. Lett.*, vol. 92, no. 9, p. 092109, 2008.

[19] J. Kim, J. Yu, and S. Kim, "Effects of sulfide-forming element additions on the kirkendall void formation and drop impact reliability of Cu/Sn–3.5 Ag solder joints," *Acta Mater.*, vol. 57, no. 17, pp. 5001–5012, 2009.

[20] S. Kumar, J. Smetana, D. Love, J. Watkowski, R. Parker, and C. A. Handwerker, "Microvoid formation at solder–copper interfaces during annealing: a systematic study of the root cause," *J. Electron. Mater.*, vol. 40, no. 12, pp. 2415–2424, 2011.

[21] C.-H. Liao, *An environmentally friendly electroplating process of copper from an alkaline solution.* PhD thesis, Case Western Reserve University, 2012.

[22] D. Malm and M. Vasile, "A study of contamination on electroplated gold, copper, platinum, and palladium," *J. Electrochem. Soc.*, vol. 120, no. 11, pp. 1484–1487, 1973.

[23] Q. Huang, B. Baker-ONeal, C. Parks, M. Hopstaken, A. Fluegel, C. Emnet, M. Arnold, and D. Mayer, "Leveler effect and oscillatory behavior during copper electroplating," *J. Electrochem. Soc.*, vol. 159, no. 9, pp. D526–D531, 2012.

[24] J. Kelly, T. Nogami, O. Van der Straten, J. Demarest, J. Li, C. Penny, T. Vo, C. Parks, P. DeHaven, C.-K. Hu, *et al.*, "Electrolyte additive chemistry and feature size-dependent impurity incorporation for Cu interconnects," *J. Electrochem. Soc.*, vol. 159, no. 10, pp. D563–D569, 2012.

[25] Q. Huang, A. Avekians, S. Ahmed, C. Parks, B. Baker-ONeal, S. Kitayaporn, A. Sahin, Y. Sun, and T. Cheng, "Impurities in the electroplated sub-50 nm Cu lines: The effects of the plating additives," *J. Electrochem. Soc.*, vol. 161, no. 9, pp. D388–D394, 2014.

[26] D. Klemm, M. Stangl, A. Peeva, V. Hoffmann, K. Wetzig, and J. Eckert, "Analysis of interface impurities in electroplated Cu layers by using gd-oes and tof-sims," *Surf. Interface Anal.*, vol. 40, no. 3-4, pp. 418–422, 2008.

[27] J. Cazaux and L. DTI, “Capabilities and limitations of high spatial resolution aes,” *Journal of Surface Analysis*, vol. 3, no. 2, pp. 286–311, 1997.

[28] C. Brundle, “The application of electron spectroscopy to surface studies,” *Journal of Vacuum Science & Technology*, vol. 11, no. 1, pp. 212–224, 1974.

[29] J. C. Vickerman and I. S. Gilmore, *Surface analysis: the principal techniques*, vol. 2. Wiley Online Library, 2009.

[30] N. H. Turner, *X-Ray Photoelectron and Auger Electron Spectroscopy*. John Wiley & Sons, Ltd, 2006.

[31] N. H. Turner and J. A. Schreifels, “Surface analysis: X-ray photoelectron spectroscopy and auger electron spectroscopy,” *Anal. Chem.*, vol. 72, no. 12, pp. 99–110, 2000.

[32] S. J. Pennycook and P. D. Nellist, *Scanning transmission electron microscopy: imaging and analysis*. Springer Science & Business Media, 2011.

[33] R. Jenkins, *X-Ray Techniques: Overview*. John Wiley & Sons, Ltd, 2006.

[34] O. Instruments, “EDS in the TEM explained.” `http://www.oxford-instruments.com/OxfordInstruments/media/nanoanalysis/brochures%20and%20thumbs/TEM-Explained.pdf`. Accessed: 2016-01-09.

[35] D. E. Newbury, C. R. Swyt, and R. L. Myklebust, “"Standardless" quantitative electron probe microanalysis with energy-dispersive x-ray spectrometry: is it worth the risk?,” *Anal. Chem.*, vol. 67, no. 11, pp. 1866–1871, 1995.

[36] F. Reniers and C. Tewell, “New improvements in energy and spatial (x, y, z) resolution in AES and XPS applications,” *J. Electron Spectrosc. Relat. Phenom.*, vol. 142, no. 1, pp. 1–25, 2005.

[37] C. M. Mahoney, “Cluster secondary ion mass spectrometry of polymers and related materials,” *Mass Spectrom. Rev.*, vol. 29, no. 2, pp. 247–293, 2010.

[38] B. Cornils, W. Herrmann, M. Beller, R. Paciello, M. Che, and J. Vedrine, *Characterization of Solid Materials and Heterogeneous Catalysts*. Wiley Online Library, 2012.

[39] A. A. Tseng, *Nanofabrication: fundamentals and applications*. World Scientific, 2008.

[40] S. G. Boxer, M. L. Kraft, and P. K. Weber, “Advances in imaging secondary ion mass spectrometry for biological samples,” *Annual review of biophysics*, vol. 38, pp. 53–74, 2009.

[41] W. A. Lamberti, “Imaging secondary ion mass spectrometry,” in *Handbook of Microscopy for Nanotechnology*, pp. 207–225, Springer, 2005.

[42] F. Hillion, F. Horreard, and F. Stadermann, "Recent results and developments on the cameca nanosims 50," in *12th International Conference on Secondary Ion Mass Spectrometry*, pp. 209–212, 1999.

[43] M. Douglas and P. Chen, "Quantitative trace metal analysis of silicon surfaces by tof-sims," *Surf. Interface Anal.*, vol. 26, no. 13, pp. 984–994, 1998.

[44] S. Herner, B. Gila, K. Jones, H.-J. Gossmann, J. Poate, and H. Luftman, "Surface roughness-induced artifacts in secondary ion mass spectrometry depth profiling and a simple technique to smooth the surface," *Journal of Vacuum Science & Technology B*, vol. 14, no. 6, pp. 3593–3595, 1996.

[45] A. Benninghoven, C. Evans Jr, R. Powell, R. Shimizu, and H. Storms, "Secondary ion mass spectrometry sims-ii. proceedings of the second international conference, held at stanford, ca, usa, 27-31 august 1979.," in *Secondary ion mass spectrometry SIMS-II. Proceedings of the second international conference, held at Stanford, CA, USA, 27-31 August 1979., by Benninghoven, A.; Evans, CA, Jr.; Powell, RA; Shimizu, R.; Storms, HA. Berlin (FR Germany): Springer, 13+ 298 p.*, vol. 1, 1980.

[46] S. Franssila, *Introduction to Microfabrication.* Wiley Online Library, 2010.

[47] J. Walls, *Methods of surface analysis: techniques and applications.* CUP Archive, 1990.

[48] W.-K. Chu, *Backscattering spectrometry.* Elsevier, 2012.

[49] H. Verma, *Atomic and Nuclear Analytical Methods: XRF, Mössbauer, XPS, NAA and Ion-Beam Spectroscopic Techniques.* Springer: Berlin, 2007.

[50] W. A. Bik and F. Habraken, "Elastic recoil detection," *Reports on Progress in Physics*, vol. 56, no. 7, p. 859, 1993.

[51] H. Metzner, M. Gossla, and T. Hahn, "Rutherford backscattering spectroscopy of rough films: Theoretical considerations," *Nuclear Instruments and Methods in Physics Research Section B: Beam Interactions with Materials and Atoms*, vol. 124, no. 4, pp. 567–574, 1997.

[52] L. Mikko, *Improvement of time-of-flight spectrometer for elastic recoil detection analysis.* PhD thesis, University of Jyväskylä, 2013.

[53] K. e. a. Mizohata, *Progress in elastic recoil detection analysis.* PhD thesis, University of Helsinki, 2012.

[54] E. Strub, W. Bohne, S. Lindner, and J. Röhrich, "Possibilities and limitations of ERDA: examples from the ERDA ToF set-up at the hahn-meitner-institut," *Surf. Interface Anal.*, vol. 35, no. 9, pp. 753–756, 2003.

[55] A. International, "Standard test methods for determining average grain size," 2010.

[56] S. Simões, R. Calinas, M. Vieira, M. Vieira, and P. Ferreira, "In situ TEM study of grain growth in nanocrystalline copper thin films," *Nanotechnology*, vol. 21, no. 14, p. 145701, 2010.

[57] K. Yin, Y. Xia, C. Chan, W. Zhang, Q. Wang, X. Zhao, A. Li, Z. Liu, M. Bayes, and K. Yee, "The kinetics and mechanism of room-temperature microstructural evolution in electroplated copper foils," *Scr. Mater.*, vol. 58, no. 1, pp. 65–68, 2008.

[58] E. Zielinski, R. Vinci, and J. Bravman, "Effects of barrier layer and annealing on abnormal grain growth in copper thin films," *J. Appl. Phys.*, vol. 76, no. 8, pp. 4516–4523, 1994.

[59] FEI, "An introduction to electron microscopy." `http://www.fei.com/documents/introduction-to-microscopy-document/`. Accessed: 2015-12-22.

[60] R. Brydson, *Aberration-corrected Analytical Electron Microscopy*, vol. 3. John Wiley & Sons, 2011.

[61] B. Fultz and J. M. Howe, *Transmission electron microscopy and diffractometry of materials*. Springer Science & Business Media, 2012.

[62] K. Nagayama and R. Danev, "Phase contrast electron microscopy: development of thin-film phase plates and biological applications," *Philosophical Transactions of the Royal Society of London B: Biological Sciences*, vol. 363, no. 1500, pp. 2153–2162, 2008.

[63] J. C. Spence, *High-resolution electron microscopy*. Oxford University Press, 2013.

[64] J. Ayache, L. Beaunier, J. Boumendil, G. Ehret, and D. Laub, *Sample preparation handbook for transmission electron microscopy: techniques*, vol. 2. Springer Science & Business Media, 2010.

[65] M. Sugiyama and G. Sigesato, "A review of focused ion beam technology and its applications in transmission electron microscopy," *J. Electron Microsc. (Tokyo)*, vol. 53, no. 5, pp. 527–536, 2004.

[66] M. e. a. Erdmanis, *Modern fabrication techniques for nanostructures and photonic components*. PhD thesis, 2014.

[67] H. Hocheng and H.-Y. Tsai, *Advanced analysis of nontraditional machining*. Springer Science & Business Media, 2012.

[68] A. A. Tseng, "Recent developments in micromilling using focused ion beam technology," *Journal of Micromechanics and Microengineering*, vol. 14, no. 4, p. R15, 2004.

[69] L. A. Giannuzzi *et al.*, *Introduction to focused ion beams: instrumentation, theory, techniques and practice.* Springer Science & Business Media, 2006.

[70] J. D. Casey Jr, M. Phaneuf, C. Chandler, M. Megorden, K. E. Noll, R. Schuman, T. J. Gannon, A. Krechmer, D. Monforte, N. Antoniou, *et al.*, "Copper device editing: Strategy for focused ion beam milling of copper," *Journal of Vacuum Science & Technology B*, vol. 20, no. 6, pp. 2682–2685, 2002.

[71] N. I. Kato, "Reducing focused ion beam damage to transmission electron microscopy samples," *J. Electron Microsc. (Tokyo)*, vol. 53, no. 5, pp. 451–458, 2004.

[72] S. Brand, A. Lapadatu, T. Djuric, P. Czurratis, J. Schischka, and M. Petzold, "Scanning acoustic gigahertz microscopy for metrology applications in three-dimensional integration technologies," *Journal of Micro/Nanolithography, MEMS, and MOEMS*, vol. 13, no. 1, pp. 011207–011207, 2014.

[73] R. G. Maev, "Scanning acoustic microscopy. physical principles and methods. current development," *Acoustic Microscopy: Fundamentals and Applications*, pp. 9–19, 2009.

[74] S. Brand, T. Appenroth, F. Naumann, W. Steller, M. J. Wolf, P. Czurratis, F. Altmann, and M. Petzold, "Acoustic GHz-microscopy and its potential applications in 3D-integration technologies," in *Electronic Components and Technology Conference (ECTC), 2015 IEEE 65th*, pp. 46–53, IEEE, 2015.

[75] S. U. Fassbender and K. Kraemer, "Acoustic microscopy: a powerful tool to inspect microstructures of electronic devices," in *NDE for Health Monitoring and Diagnostics*, pp. 112–121, International Society for Optics and Photonics, 2003.

[76] H. Volders, L. Carbonell, N. Heylen, K. Kellens, C. Zhao, K. Marrant, G. Faelens, T. Conard, B. Parmentier, J. Steenbergen, *et al.*, "Barrier and seed repair performance of thin RuTa films for Cu interconnects," *Microelectron. Eng.*, vol. 88, no. 5, pp. 690–693, 2011.

[77] P. Gondcharton, B. Imbert, L. Benaissa, F. Fournel, and M. Verdier, "Effect of copper–copper direct bonding on voiding in metal thin films," *J. Electron. Mater.*, vol. 44, no. 11, pp. 4128–4133, 2015.

[78] G. Beyer, A. Satta, J. Schuhmacher, K. Maex, W. Besling, O. Kilpela, H. Sprey, and G. Tempel, "Development of sub-10-nm atomic layer deposition barriers for Cu/low-k interconnects," *Microelectron. Eng.*, vol. 64, no. 1, pp. 233–245, 2002.

[79] K. Lee, C. Hu, and K. Tu, "Insitu scanning electron microscope comparison studies on electromigration of Cu and Cu (Sn) alloys for advanced chip interconnects," *J. Appl. Phys.*, vol. 78, no. 7, pp. 4428–4437, 1995.

[80] C.-K. Hu, L. Gignac, R. Rosenberg, E. Liniger, J. Rubino, C. Sambucetti, A. Domenicucci, X. Chen, and A. Stamper, "Reduced electromigration of Cu wires by surface coating," *Appl. Phys. Lett.*, vol. 81, no. 10, pp. 1782–1784, 2002.

[81] A. Kaloyeros and E. Eisenbraun, "Ultrathin diffusion barriers/liners for gigascale copper metallization," *Annual review of materials science*, vol. 30, no. 1, pp. 363–385, 2000.

[82] V. Curicuta, D. Poulain, D. Alexander, R. De Angelis, S. Gasser, and E. Kolawa, "Furnace and laser methods of bonding metals to ceramics: phenomenological investigation," *Materials Science and Engineering: B*, vol. 68, no. 3, pp. 186–195, 2000.

[83] S.-M. Yi, J.-U. An, S.-S. Hwang, J. R. Yim, Y.-H. Huh, Y.-B. Park, and Y.-C. Joo, "Electrical reliability and interfacial adhesion of Cu (Mg) thin films for interconnect process adaptability," *Thin Solid Films*, vol. 516, no. 8, pp. 2325–2330, 2008.

[84] M. Juppo, M. Ritala, and M. Leskelä, "Use of 1, 1-dimethylhydrazine in the atomic layer deposition of transition metal nitride thin films," *J. Electrochem. Soc.*, vol. 147, no. 9, pp. 3377–3381, 2000.

[85] P. Alén, M. Ritala, K. Arstila, J. Keinonen, and M. Leskelä, "Atomic layer deposition of molybdenum nitride thin films for Cu metallizations," *J. Electrochem. Soc.*, vol. 152, no. 5, pp. G361–G366, 2005.

[86] M. Juppo and et al., *Atomic layer deposition of metal and transition metal nitride thin films and in situ mass spectrometry studies.* PhD thesis, University of Helsinki, 2001.

[87] T. J. Knisley, T. C. Ariyasena, T. Sajavaara, M. J. Saly, and C. H. Winter, "Low temperature growth of high purity, low resistivity copper films by atomic layer deposition," *Chem. Mater.*, vol. 23, no. 20, pp. 4417–4419, 2011.

[88] H. Ishikawa, T. Nozawa, T. Matsuoka, A. Teramoto, M. Hirayama, T. Ito, and T. Ohmi, "Evaluation of new amorphous hydrocarbon film for copper barrier dielectric film in low-k copper metallization," *Japanese Journal of Applied Physics*, vol. 47, no. 4S, p. 2531, 2008.

[89] S. Divinski, J. Ribbe, G. Schmitz, and C. Herzig, "Grain boundary diffusion and segregation of Ni in Cu," *Acta Mater.*, vol. 55, no. 10, pp. 3337–3346, 2007.

[90] V. Keast, J. Bruley, P. Rez, J. Maclaren, and D. Williams, "Chemistry and bonding changes associated with the segregation of Bi to grain boundaries in Cu," *Acta Mater.*, vol. 46, no. 2, pp. 481–490, 1998.

[91] X. Liu, D. Tham, D. Yates, and C. J. McMahon, “Evidence for the intergranular segregation of tin to grain boundaries of a Cu–Sn alloy and its consequences for dynamic embrittlement,” *Materials Science and Engineering: A*, vol. 458, no. 1, pp. 123–125, 2007.

[92] J. Bruley, V. Keast, and D. Williams, “An EELS study of segregation-induced grain-boundary embrittlement of copper,” *Acta Mater.*, vol. 47, no. 15, pp. 4009–4017, 1999.

[93] E. Lugscheider, S. Ferrara, H. Janssen, A. Reimann, and B. Wildpanner, “Progress and developments in the field of materials for transient liquid phase bonding and active soldering processes,” *Microsystem technologies*, vol. 10, no. 3, pp. 233–236, 2004.

[94] L. Di Cioccio, F. Baudin, P. Gergaud, V. Delaye, P.-H. Jouneau, F. Rieutord, and T. Signamarcheix, “Modeling and integration phenomena of metal-metal direct bonding technology,” *ECS Transactions*, vol. 64, no. 5, pp. 339–355, 2014.

[95] B. T. Tung, F. Kato, N. Watanabe, S. Nemoto, K. Kikuchi, and M. Aoyagi, “15-μm-pitch Cu/Au interconnections relied on self-aligned low-temperature thermosonic flip-chip bonding technique for advanced chip stacking applications,” *Japanese Journal of Applied Physics*, vol. 53, no. 4S, p. 04EB04, 2014.

[96] G. Botton and C. Humphreys, “Determining the bonding in intermetallics using electron energy loss spectroscopy and density functional theory,” *Intermetallics*, vol. 7, no. 7, pp. 829–833, 1999.

[97] Y.-J. Chang, Y.-S. Hsieh, and K.-N. Chen, “Submicron Cu/Sn bonding technology with transient ni diffusion buffer layer for 3DIC application,” *Electron Device Letters, IEEE*, vol. 35, no. 11, pp. 1118–1120, 2014.

[98] K. Tanida, M. Umemoto, N. Tanaka, Y. Tomita, and K. Takahashi, “Micro Cu bump interconnection on 3D chip stacking technology,” *Japanese journal of applied physics*, vol. 43, no. 4S, p. 2264, 2004.

[99] K. Takahashi, M. Umemoto, N. Tanaka, K. Tanida, Y. Nemoto, Y. Tomita, M. Tago, and M. Bonkohara, “Ultra-high-density interconnection technology of three-dimensional packaging,” *Microelectronics Reliability*, vol. 43, no. 8, pp. 1267–1279, 2003.

[100] C. K. Chung, Z. Zhu, and C. Kao, “Thermal stress of surface oxide layer on micro solder bumps during reflow,” *J. Electron. Mater.*, vol. 44, no. 2, pp. 744–750, 2015.

[101] H. Ezawa, M. Miyata, S. Honma, H. Inoue, T. Tokuoka, J. Yoshioka, and M. Tsujimura, “Eutectic sn-ag solder bump process for ulsi flip chip technology,” *Electronics Packaging Manufacturing, IEEE Transactions on*, vol. 24, no. 4, pp. 275–281, 2001.

[102] B. Rebhan and K. Hingerl, "Physical mechanisms of copper-copper wafer bonding," *J. Appl. Phys.*, vol. 118, no. 13, p. 135301, 2015.

[103] M. J. Kim, K. J. Park, T. Lim, O. J. Kwon, and J. J. Kim, "Fabrication of Cu-Ag interconnection using electrodeposition: The mechanism of superfilling and the properties of Cu-Ag film," *J. Electrochem. Soc.*, vol. 160, no. 12, pp. D3126–D3133, 2013.

[104] Y. Yuan, Y. Guan, D. Li, and N. Moelans, "Investigation of diffusion behavior in Cu–Sn solid state diffusion couples," *J. Alloys Compd.*, vol. 661, pp. 282–293, 2016.

[105] L. Chen, M. Huang, and S. Zhou, "Effect of electromigration on intermetallic compound formation in line-type Cu/Sn/Cu interconnect," *J. Alloys Compd.*, vol. 504, no. 2, pp. 535–541, 2010.

[106] H. Liu, G. Salomonsen, K. Wang, K. E. Aasmundtveit, and N. Hoivik, "Wafer-level Cu/Sn to Cu/Sn SLID-bonded interconnects with increased strength," *Components, Packaging and Manufacturing Technology, IEEE Transactions on*, vol. 1, no. 9, pp. 1350–1358, 2011.

[107] G.-T. Lim, B.-J. Kim, K. Lee, J. Kim, Y.-C. Joo, and Y.-B. Park, "Temperature effect on intermetallic compound growth kinetics of Cu pillar/Sn bumps," *J. Electron. Mater.*, vol. 38, no. 11, pp. 2228–2233, 2009.

[108] G.-T. Lim, B.-J. Kim, K. Lee, J. Kim, Y.-C. Joo, and Y.-B. Park, "Effect of isothermal aging on intermetallic compounds and kirkendall void growth kinetics of Au stud bumps," *Metals and Materials International*, vol. 15, no. 5, pp. 819–823, 2009.

[109] G. Vakanas, B. Vandecasteele, D. Schaubroek, J. De Messemaeker, G. Willems, M. A. Ashworth, G. D. Wilcox, and I. De Wolf, "Sn whisker evaluations in 3D microbumped structures," *Microelectronics Reliability*, vol. 54, no. 9, pp. 1982–1987, 2014.

[110] M. Murugesan, Y. Ohara, T. Fukushima, T. Tanaka, and M. Koyanagi, "Low-resistance Cu-Sn electroplated–evaporated microbumps for 3D chip stacking," *J. Electron. Mater.*, vol. 41, no. 4, pp. 720–729, 2012.

[111] B. Horváth, "Influence of copper diffusion on the shape of whiskers grown on bright tin layers," *Microelectronics Reliability*, vol. 53, no. 7, pp. 1009–1020, 2013.

[112] U. Alber, H. Müllejans, and M. Rühle, "Bismuth segregation at copper grain boundaries," *Acta Mater.*, vol. 47, no. 15, pp. 4047–4060, 1999.

[113] C.-M. Liu, H.-w. Lin, Y.-C. Chu, C. Chen, D.-R. Lyu, K.-N. Chen, and K. Tu, "Low-temperature direct copper-to-copper bonding enabled by creep on highly (111)-oriented Cu surfaces," *Scr. Mater.*, vol. 78, pp. 65–68, 2014.

[114] H. Shimizu, K. Sakoda, T. Momose, and Y. Shimogaki, "Atomic layer deposited Co (W) film as a single-layered barrier/liner for next-generation Cu-interconnects," *Japanese Journal of Applied Physics*, vol. 51, no. 5S, p. 05EB02, 2012.

[115] C. Okoro, R. Labie, K. Vanstreels, A. Franquet, M. Gonzalez, B. Vandevelde, E. Beyne, D. Vandepitte, and B. Verlinden, "Impact of the electrodeposition chemistry used for TSV filling on the microstructural and thermo-mechanical response of Cu," *J. Mater. Sci.*, vol. 46, no. 11, pp. 3868–3882, 2011.

[116] N. Lin, J. Miao, and P. Dixit, "Void formation over limiting current density and impurity analysis of TSV fabricated by constant-current pulse-reverse modulation," *Microelectronics Reliability*, vol. 53, no. 12, pp. 1943–1953, 2013.

[117] J. Hess and H. Vogt, "Sacrificial ion beam etching process for seed layer removal of 6 μm pitch CuSn micro bumps," in *IOP Conference Series: Materials Science and Engineering*, vol. 41, p. 012005, IOP Publishing, 2012.

[118] F. Inoue, H. Philipsen, M. van der Veen, S. Van Huylenbroeck, S. Armini, H. Struyf, and T. Tanaka, "Electroless Cu seed on Ru and Co liners in high aspect ratio TSV," in *Interconnect Technology Conference/Advanced Metallization Conference (IITC/AMC), 2014 IEEE International*, pp. 207–210, IEEE, 2014.

[119] T. Wang, Y. Cheng, Y. Wang, T. Hsieh, G. Hwang, and C. Chen, "Comparison of characteristics and integration of copper diffusion-barrier dielectrics," *Thin Solid Films*, vol. 498, no. 1, pp. 36–42, 2006.

[120] J. Barnes, V. Carreau, and S. Maitrejean, "Tof-sims imaging of Cl at Cu grain boundaries in interconnects for microelectronics," *Appl. Surf. Sci.*, vol. 255, no. 4, pp. 1564–1568, 2008.

[121] K. Maekawa, K. Mori, N. Suzumura, K. Honda, Y. Hirose, K. Asai, A. Uedono, and M. Kojima, "Impact of Al in Cu alloy interconnects on electro and stress migration reliabilities," *Microelectron. Eng.*, vol. 85, no. 10, pp. 2137–2141, 2008.

[122] J.-M. Park, J.-W. Kim, and Y.-B. Park, "Effects of wet treatment conditions and pattern densities on interfacial bonding characteristics of Cu–Cu direct bonds," *Japanese Journal of Applied Physics*, vol. 53, no. 5S3, p. 05HB07, 2014.

[123] B. Rebhan, G. Hesser, J. Duchoslav, V. Dragoi, M. Wimplinger, and K. Hingerl, "Low-temperature Cu-Cu wafer bonding," *ECS Transactions*, vol. 50, no. 7, pp. 139–149, 2013.

[124] M. Murugesan, H. Nohira, H. Kobayashi, T. Fukushima, T. Tanaka, and M. Koyanagi, "Locally induced stress in stacked ultrathin Si wafers: XPS and μ-raman study," in *Electronic Components and Technology Conference (ECTC), 2012 IEEE 62nd*, pp. 625–629, IEEE, 2012.

[125] M. Murugesan, H. Kobayashi, H. Shimamoto, F. Yamada, T. Fukushima, J. Bea, K. W. Lee, T. Tanaka, and M. Koyanagi, “Minimizing the local deformation induced around Cu-TSVs and CuSn/InAu-microbumps in high-density 3D-LSIs,” in *Electron Devices Meeting (IEDM), 2012 IEEE International*, pp. 28–6, IEEE, 2012.

[126] B. Neveu, F. Lallemand, G. Poupon, and Z. Mekhalif, “Electrodeposition of pb-free sn alloys in pulsed current,” *Appl. Surf. Sci.*, vol. 252, no. 10, pp. 3561–3573, 2006.

[127] A. Lis and C. Leinenbach, “Effect of process and service conditions on tlp-bonded components with Ag, Ni– Sn interlayer combinations,” *J. Electron. Mater.*, vol. 44, no. 11, pp. 4576–4588, 2015.

[128] H. Kim, T. Koseki, T. Ohba, T. Ohta, Y. Kojima, H. Sato, and Y. Shimogaki, “Process design of Cu (Sn) alloy deposition for highly reliable ultra large-scale integration interconnects,” *Thin Solid Films*, vol. 491, no. 1, pp. 221–227, 2005.

[129] C. Lee and Y.-L. Kuo, “The evolution of diffusion barriers in copper metallization,” *JOM*, vol. 59, no. 1, pp. 44–49, 2007.

[130] K. Barmak, A. Gungor, C. Cabral Jr, and J. Harper, “Annealing behavior of Cu and dilute Cu-alloy films: Precipitation, grain growth, and resistivity,” *J. Appl. Phys.*, vol. 94, no. 3, pp. 1605–1616, 2003.

[131] E. Voelker, F. J. Williams, E. J. Calvo, T. Jacob, and D. J. Schiffrin, “O2 induced Cu surface segregation in Au–Cu alloys studied by angle resolved XPS and DFT modelling,” *Phys. Chem. Chem. Phys.*, vol. 14, no. 20, pp. 7448–7455, 2012.

[132] S. Jin, G. Wang, and B. Yoo, “Through-silicon-via TSV filling by electrodeposition of Cu with pulse current at ultra-short duty cycle,” *J. Electrochem. Soc.*, vol. 160, no. 12, pp. D3300–D3305, 2013.

[133] P. Shang, Z. Liu, D. Li, and J. Shang, “Intermetallic compound identification and kirkendall void formation in eutectic SnIn/Cu solder joint during solid-state aging,” *Philos. Mag. Lett.*, vol. 91, no. 6, pp. 410–417, 2011.

[134] C. K. Chung, Y. Chen, T. Yang, and C. Kao, “Reactions of Sn-4.0 Ag-0.5 Cu on Cu and electroless Ni substrate in premelting soldering process,” *J. Electron. Mater.*, vol. 42, no. 6, pp. 1254–1259, 2013.

[135] T.-C. Liu, C.-M. Liu, Y.-S. Huang, C. Chen, and K.-N. Tu, “Eliminate kirkendall voids in solder reactions on nanotwinned copper,” *Scr. Mater.*, vol. 68, no. 5, pp. 241–244, 2013.

[136] K. Chen, A. Fan, C. Tan, R. Reif, and C. Wen, “Microstructure evolution and abnormal grain growth during copper wafer bonding,” *Appl. Phys. Lett.*, vol. 81, no. 20, pp. 3774–3776, 2002.

[137] C.-M. Liu, H.-W. Lin, Y.-S. Huang, Y.-C. Chu, C. Chen, D.-R. Lyu, K.-N. Chen, and K.-N. Tu, "Low-temperature direct copper-to-copper bonding enabled by creep on (111) surfaces of nanotwinned Cu," *Scientific reports*, vol. 5, 2015.

[138] K. Tanida, M. Umemoto, Y. Tomita, M. Tago, R. Kajiwara, Y. Akiyama, and K. Takahashi, "Au bump interconnection with ultrasonic flip-chip bonding in 20 μm pitch," *Japanese Journal of Applied Physics*, vol. 42, no. 4S, p. 2198, 2003.

[139] C.-K. Hu, L. Gignac, and R. Rosenberg, "Electromigration of Cu/low dielectric constant interconnects," *Microelectronics reliability*, vol. 46, no. 2, pp. 213–231, 2006.

[140] Y. Amouyal, S. Divinski, L. Klinger, and E. Rabkin, "Grain boundary diffusion and recrystallization in ultrafine grain copper produced by equal channel angular pressing," *Acta Mater.*, vol. 56, no. 19, pp. 5500–5513, 2008.

[141] T.-C. Liu, C. Chen, K.-J. Chiu, H.-W. Lin, and J.-C. Kuo, "Novel EBSD preparation method for Cu/Sn microbumps using a focused ion beam," *Mater. Charact.*, vol. 74, pp. 42–48, 2012.

[142] B. Majeed, P. Soussan, P. Le Boterf, and P. Bouillon, "Microbumping technology for hybrid IR detectors, 10μm pitch and beyond," in *Electronics Packaging Technology Conference (EPTC), 2014 IEEE 16th*, pp. 453–457, IEEE, 2014.

[143] J.-Y. Chang, R.-S. Cheng, K.-S. Kao, T.-C. Chang, and T.-H. Chuang, "Reliable microjoints formed by solid–liquid interdiffusion SLID bonding within a chip-stacking architecture," *Components, Packaging and Manufacturing Technology, IEEE Transactions on*, vol. 2, no. 6, pp. 979–984, 2012.

[144] A. Klumpp, R. Merkel, P. Ramm, J. Weber, and R. Wieland, "Vertical system integration by using inter-chip vias and solid-liquid interdiffusion bonding," *Japanese Journal of Applied Physics*, vol. 43, no. 7A, p. L829, 2004.

[145] C.-T. Ko and K.-N. Chen, "Low temperature bonding technology for 3D integration," *Microelectronics reliability*, vol. 52, no. 2, pp. 302–311, 2012.

[146] R. I. Made, P. Lan, H. Y. Li, C. L. Gan, and C. S. Tan, "Effect of direct current stressing to Cu–Cu bond interface imperfection for three dimensional integrated circuits," *Microelectron. Eng.*, vol. 106, pp. 149–154, 2013.

[147] E.-J. Jang, S. Hyun, H.-J. Lee, and Y.-B. Park, "Effect of wet pretreatment on interfacial adhesion energy of Cu-Cu thermocompression bond for 3D IC packages," *J. Electron. Mater.*, vol. 38, no. 12, pp. 2449–2454, 2009.

[148] T.-C. Liu, S.-R. Wang, and M. Corey, "Fabrication and characterization of grain growth in electroplated Cu for 3D IC interconnect applications," in *Meeting Abstracts*, no. 29, pp. 2056–2056, The Electrochemical Society, 2013.

[149] H.-Y. Hsiao, C.-M. Liu, H.-w. Lin, T.-C. Liu, C.-L. Lu, Y.-S. Huang, C. Chen, and K. Tu, "Unidirectional growth of microbumps on (111)-oriented and nanotwinned copper," *Science*, vol. 336, no. 6084, pp. 1007–1010, 2012.

[150] H.-H. Hsu, S.-Y. Huang, T.-C. Chang, and A. T. Wu, "Nucleation and propagation of voids in microbumps for 3 dimensional integrated circuits," *Appl. Phys. Lett.*, vol. 99, no. 25, p. 251913, 2011.

[151] W.-L. Chiu, C.-M. Liu, Y.-S. Haung, and C. Chen, "Formation of nearly void-free Cu3Sn intermetallic joints using nanotwinned Cu metallization," *Appl. Phys. Lett.*, vol. 104, no. 17, p. 171902, 2014.

[152] J. E. Semmens and L. W. Kessler, "Characterization of flip chip interconnect failure modes using high frequency acoustic micro imaging with correlative analysis," in *Reliability Physics Symposium, 1997. 35th Annual Proceedings., IEEE International*, pp. 141–148, IEEE, 1997.

[153] C. S. Lee, G.-M. Zhang, D. M. Harvey, and A. Qi, "Characterization of micro-crack propagation through analysis of edge effect in acoustic microimaging of microelectronic packages," *NDT & E International*, vol. 79, pp. 1–6, 2016.

[154] C. Flötgen, M. Pawlak, E. Pabo, H. van de Wiel, G. Hayes, and V. Dragoi, "Wafer bonding using Cu-Sn intermetallic bonding layers," *Microsystem technologies*, vol. 20, no. 4-5, pp. 653–662, 2014.

[155] L. Sanchez, L. Bally, B. Montmayeul, F. Fournel, J. Dafonseca, E. Augendre, L. D. Cioccio, V. Carron, T. Signamarcheix, R. Taibi, *et al.*, "Chip to wafer direct bonding technologies for high density 3D integration," in *Electronic Components and Technology Conference (ECTC), 2012 IEEE 62nd*, pp. 1960–1964, IEEE, 2012.

[156] L. W. Kong, J. R. Lloyd, A. C. Rudack, and A. C. Diebold, "Thermally induced void growth in through-silicon vias," *Journal of Micro/Nanolithography, MEMS, and MOEMS*, vol. 12, no. 2, pp. 023010–023010, 2013.

[157] Y. K. Tsui and S. R. Lee, "Design and fabrication of a flip-chip-on-chip 3-D packaging structure with a through-silicon via for underfill dispensing," *Advanced Packaging, IEEE Transactions on*, vol. 28, no. 3, pp. 413–420, 2005.

[158] S.-Y. Huang, T.-C. Chang, R.-S. Cheng, J.-Y. Chang, F.-J. Leu, Y.-L. Lu, and T.-F. Yang, "Reliability assessment of the 20 um pitch micro-joints within a 3DIC assembly under various environments," in *Microsystems Packaging Assembly and Circuits Technology Conference (IMPACT), 2010 5th International*, pp. 1–4, Oct 2010.

[159] P. Borgesen, L. Yin, and P. Kondos, "Assessing the risk of kirkendall voiding in Cu 3 Sn," *Microelectronics Reliability*, vol. 51, no. 4, pp. 837–846, 2011.

[160] M. Rizzolo, S. Novak, E. Lifshin, and K. A. Dunn, "Correlating surface segregation and microstructural evolution of electrochemically deposited copper," *Appl. Phys. Lett.*, vol. 101, no. 10, p. 101901, 2012.

[161] T. Anderson and I. Ansara, "The Ga-Sn (gallium-tin) system," *Journal of phase equilibria*, vol. 13, no. 2, pp. 181–189, 1992.

[162] S. Wang, L. Hsu, N. Wang, and C.-E. Ho, "EBSD investigation of Cu-Sn imc microstructural evolution in Cu/Sn-Ag/Cu microbumps during isothermal annealing," *J. Electron. Mater.*, vol. 43, no. 1, pp. 219–228, 2014.

[163] Y. Liu, J. Wang, L. Yin, P. Kondos, C. Parks, P. Borgesen, D. Henderson, E. Cotts, and N. Dimitrov, "Influence of plating parameters and solution chemistry on the voiding propensity at electroplated copper–solder interface," *J. Appl. Electrochem.*, vol. 38, no. 12, pp. 1695–1705, 2008.

[164] T. Moffat, D. Wheeler, and D. Josell, "Electrodeposition of copper in the SPS-PEG-Cl additive system I. Kinetic measurements: influence of SPS," *J. Electrochem. Soc.*, vol. 151, no. 4, pp. C262–C271, 2004.

A Appendix

Name	Electroplating Solution (Concentration, Supplier, Chemical)
Basic Solution A (Low Quality)	0.25 M $CuSO \cdot 5H_2O$ (ACS reagent) (Aldrich, 209198) 1.8 M H_2SO_4 (Reagent) 1.92 mM HCl (Aldrich, 40304)
Basic Solution B (High Quality)	0.25 M $CuSO \cdot 5H_2O$ (ACS reagent) (Aldrich, 209198) 1.8 M H_2SO_4 (Semiconductor Grade, VLSI) (Aldrich, 40306) 1.92 mM HCl (Aldrich, 40304)
SPS	0.25 M $CuSO \cdot 5H_2O$ (ACS reagent(Aldrich, 209198) 1.8 M H_2SO_4 (Semiconductor Grade, VLSI) (Aldrich, 40306) 1.92 mM HCl (Aldrich, 40304) 0.01 mM SPS (Raschig, RALU®PLATE SPS)
PEG	0.25 M $CuSO \cdot 5H_2O$ (ACS reagent) (Aldrich, 209198) 1.8 M H_2SO_4 (Semiconductor Grade, VLSI) (Aldrich, 40306) 1.92 mM HCl (Aldrich, 40304) 0.059 mM PEG (Aldrich, 202444)
SPS+PEG	0.25 M $CuSO \cdot 5H_2O$ (ACS reagent) (Aldrich, 209198) 1.8 M H_2SO_4 (Semiconductor Grade, VLSI) (Aldrich, 40306) 1.92 mM HCl (Aldrich, 40304) 0.01 mM SPS (Raschig, RALU®PLATE SPS) 0.059 mM PEG (Aldrich, 202444)

Figure A1: The different copper electrolytes used in this thesis.

B Appendix

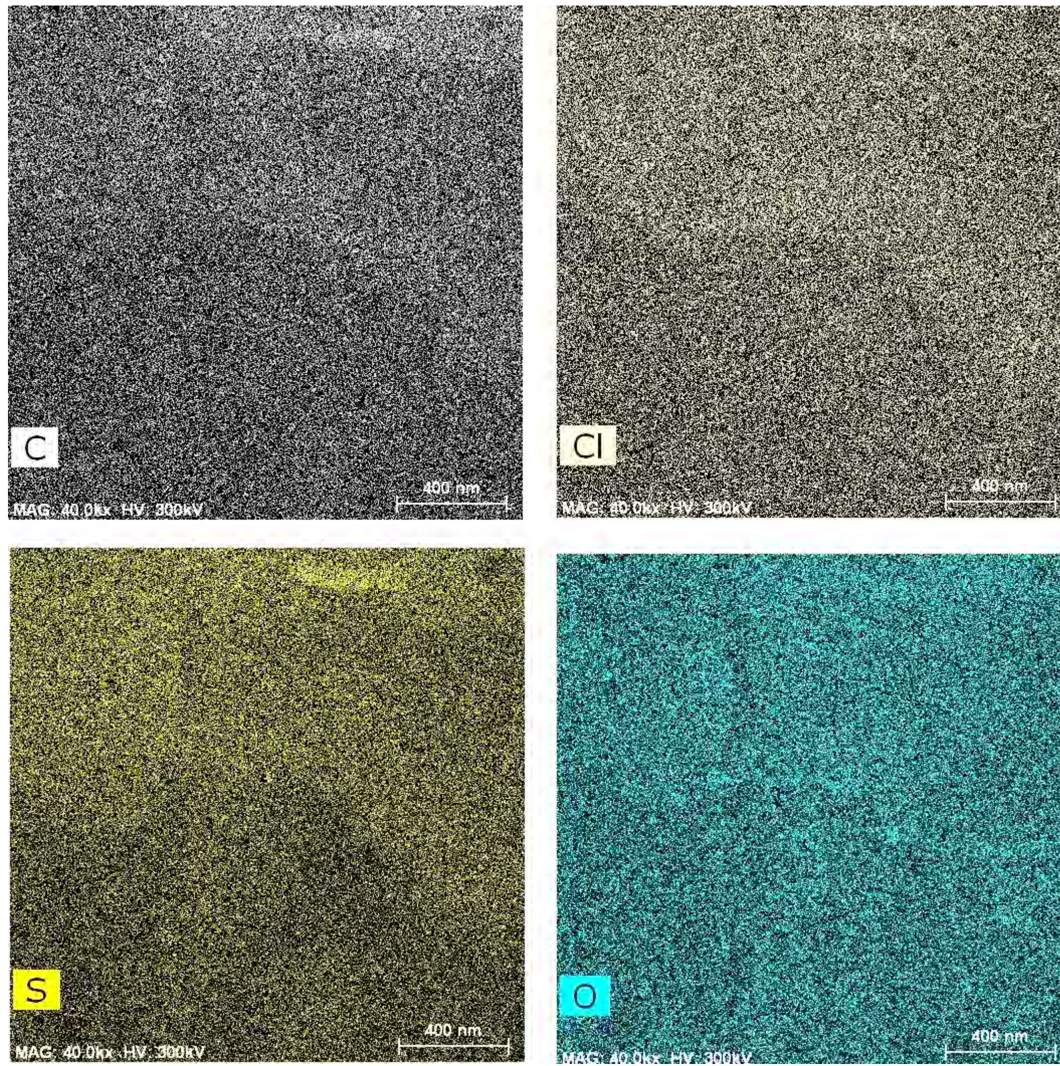

Figure B1: The rest of the chemical maps from the sample A-1. Impurities, that is usually claimed to be related to the Kirkendall voiding, could not be found.

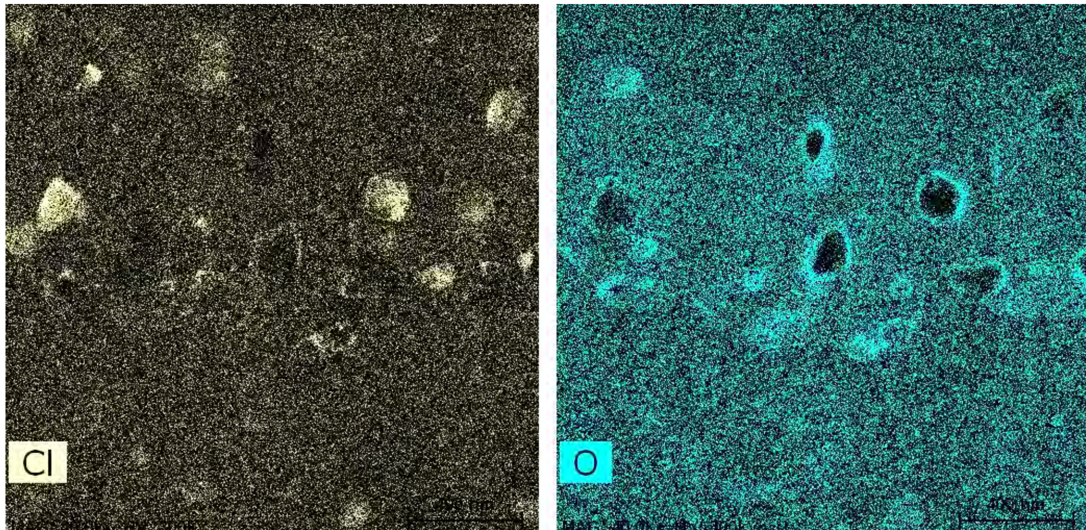

Figure B2: The rest of the chemical maps from the sample A-2. Sulphur, that is usually claimed to be related to the Kirkendall voiding, could not be found.

C Appendix

Table C1: The calculated values and errors for the grain size analysis

	A-1	**A-2**	**B-1**	**B-2**	**B-3**
Type	SPS	SPS 150C 4h	SPS	SPS 150c 4h	SPS 150c 24h
# Grains Observed (average)	6	4.8	6	4	4
True Area (µm)	1	1	1	1	1
Grain Size Number	20	19	19	19	19
Average Grain Size ASTM (µm)	0.40	0.46	0.43	0.53	0.52
Pos. Error (µm)	0.04	0.06	0.05	0.09	0.09
Neg. Error (µm)	0.03	0.04	0.03	0.06	0.06
Average Grain Size Intercept (µm)	0.39	0.43	0.38	0.41	0.33
Pos. Error (µm)	0.03	0.06	0.02	0.03	0.04
Neg. Error (µm)	0.03	0.04	0.00	0.02	0.02
	B-4	**B-5**	**B-6**	**C-1**	**C-2**
Type	SPS+PEG	SPS+PEG 150C 4h	SPS+PEG 150C 24h	SPS (new)	SPS (new) 150C 24h
# Grains Observed (average)	2	4	4	6	4
True Area (µm)	4	8	6	1	4
Grain Size Number	16	16	16	19	17
Average Grain Size ASTM (µm)	1.49	1.42	1.27	0.43	1.04
Pos. Error (µm)	0.75	0.22	0.22	0.05	0.18
Neg. Error (µm)	0.30	0.15	0.14	0.03	0.12
Average Grain Size Intercept (µm)	0.82	1.21	1.11	0.30	0.72
Pos. Error (µm)	0.15	0.12	0.16	0.02	0.11
Neg. Error (µm)	0.09	0.09	0.10	0.01	0.07
	C-3	**C-4**	**C-5**	**C-6**	**D-1**
Type	PEG (new)	PEG (new) 150C 24h	Basic sol. A (new)	Basic sol. B (new)	SPS+PEG 150C 24h (thick)
# Grains Observed (average)	5	4	8	6	3
True Area (µm)	1	1	1	1	16
Grain Size Number	19	19	20	20	15
Average Grain Size ASTM (µm)	0.44	0.48	0.35	0.42	2.22
Pos. Error (µm)	0.05	0.07	0.02	0.04	0.45
Neg. Error (µm)	0.04	0.05	0.02	0.03	0.28
Average Grain Size Intercept (µm)	0.30	0.40	0.24	0.24	1.47
Pos. Error (µm)	0.03	0.05	0.02	0.02	0.31
Neg. Error (µm)	0.02	0.03	0.01	0.01	0.17